

# Studies of light exotic nuclei in the vicinity of neutron and proton drip lines at FLNR JINR

L V Grigorenko, M S Golovkov, S A Krupko, S I Sidorchuk,  
G M Ter-Akopian, A S Fomichev, V Chudoba

DOI: 10.3367/UFNe.0186.201604a.0337

## Contents

<b>1. Introduction</b>	<b>322</b>
1.1 Qualitatively new phenomena at the drip lines; 1.2 Applied aspects of radioactive isotope studies; 1.3 Methods of RIB production; 1.4 Main RIB factories and prospective projects; 1.5 Typical research methods with RIBs; 1.6 RIB studies in the Flerov Laboratory of Nuclear Reactions	
<b>2. Direct reactions at intermediate energies</b>	<b>327</b>
2.1 Advantages and drawbacks of reactions at different energies; 2.2 Correlations and spin-parity identification; 2.3 Monte Carlo simulations; 2.4 Correlations in three-body systems	
<b>3. Dynamics of a few-body problem at the border of stability</b>	<b>332</b>
3.1 Hyperspherical harmonics method for the three-body problem; 3.2 Borromean nuclei; 3.3 Soft dipole mode; 3.4 Two-proton radioactivity; 3.5 Democratic decays; 3.6 Coulomb three-body problem for 2p-decays; 3.7 Three-body mechanism of the Thomas–Ehrman shift; 3.8 Long-living 2n/4n-emitters	
<b>4. Experimental techniques</b>	<b>343</b>
4.1 U-400M accelerator; 4.2 ACCULINNA fragment separator; 4.3 Particle and gamma-ray detectors; 4.4 Cryogenic $^{1,2,3}\text{H}$ , $^4\text{He}$ targets; 4.5 Optical time-projection chamber	
<b>5. Research at the ACCULINNA facility</b>	<b>348</b>
5.1 Dineutron structure of the $^6\text{He}$ neutron halo; 5.2 Study of the $^6\text{He}$ structure in quasifree scattering reactions; 5.3 $^9\text{He}$ : unambiguous spectrum identification; 5.4 $^5\text{H}$ : the ground state and spectrum; 5.5 $^{10}\text{He}$ : the end of the shell magic; 5.6 $^6\text{Be}$ : isovector soft dipole mode; 5.7 $^8\text{He}$ : $2^+$ state and soft dipole mode; 5.8 $^7\text{H}$ and the 4n-decay problem; 5.9 $^{17}\text{Ne}$ for astrophysics; 5.10 Search for $^{26}\text{S}$	
<b>6. Implemented and prospective projects</b>	<b>359</b>
6.1 ACCULINNA-2; 6.2 User center built around ACCULINNA-2; 6.3 Project EXPERT; 6.4 Storage ring complex and electron-ion collider based on ACCULINNA-2; 6.5 Storage ring complex for direct reactions with beams of radioactive isotopes	
<b>7. Conclusion</b>	<b>364</b>
<b>References</b>	<b>365</b>

**L V Grigorenko** Joint Institute for Nuclear Research,  
Flerov Laboratory of Nuclear Reactions,  
ul. Joliot-Curie 6, 141980 Dubna, Moscow region, Russian Federation;  
National Research Nuclear University MEPhI  
(Moscow Engineering Physics Institute),  
Kashirskoe shosse 31, 115409 Moscow, Russian Federation;  
National Research Centre ‘Kurchatov Institute’,  
pl. Kurchatova 1, 123182 Moscow, Russian Federation  
**M S Golovkov, S A Krupko, S I Sidorchuk, G M Ter-Akopian,**  
**A S Fomichev** Joint Institute for Nuclear Research,  
Flerov Laboratory of Nuclear Reactions,  
ul. Joliot-Curie 6, 141980 Dubna, Moscow region, Russian Federation  
E-mail: fomichev@jinr.ru  
**V Chudoba** Joint Institute for Nuclear Research,  
Flerov Laboratory of Nuclear Reactions,  
ul. Joliot-Curie 6, 141980 Dubna, Moscow region, Russian Federation;  
Institute of Physics, Silesian University in Opava,  
Bezručovo nám. 13, 74601 Czech Republic

Received 10 October 2015, revised 4 December 2015  
*Uspekhi Fizicheskikh Nauk* **186** (4) 337 – 386 (2016)  
DOI: 10.3367/UFNr.0186.201604a.0337  
Translated by A S Fomichev; edited by A Radzig

**Abstract.** Defining the limits of the existence of the nuclear structure is one of fundamental problems of natural science, requiring the advancement of studies towards the sites of maximum neutron- and proton-excess nuclei, to the borders of nuclear stability, and further, to the regions of nuclear instability. In such regions, nuclear systems exist only as resonant states in continuous spectra with characteristic ‘nuclear’ lifetimes. This work is done most effectively with experimental setups providing radioactive ion beams (RIBs). This review discusses the approaches in this field of research developed during the last 20 years at the ACCULINNA fragment separator in the Flerov Laboratory of Nuclear Reactions (FLNR) of the Joint Institute for Nuclear Research (JINR). The methodology developed is based on the comprehensive study of correlations among the reaction fragments emitted in the decays of nuclear-unstable systems which are populated in direct reactions induced by RIBs with intermediate (20–60 MeV per nucleon) energies. This allows us to acquire detailed knowledge about exotic nuclear systems close to and beyond nuclear drip lines. We discuss exotic forms of nuclear dynamics appearing in the vicinity of nuclear drip lines and

relevant results of their theoretical analysis. Also discussed are existing facilities and prospective projects aimed at nuclear structure studies with RIBs at JINR.

**Keywords:** radioactive beams, drip lines, neutron- and proton-rich nuclei, direct reactions, heavy-ion cyclotrons, fragment separators, cryogenic targets, correlation measurements, astrophysics, few-body systems, hyperspherical harmonics, two-proton radioactivity, democratic decays, resonance states

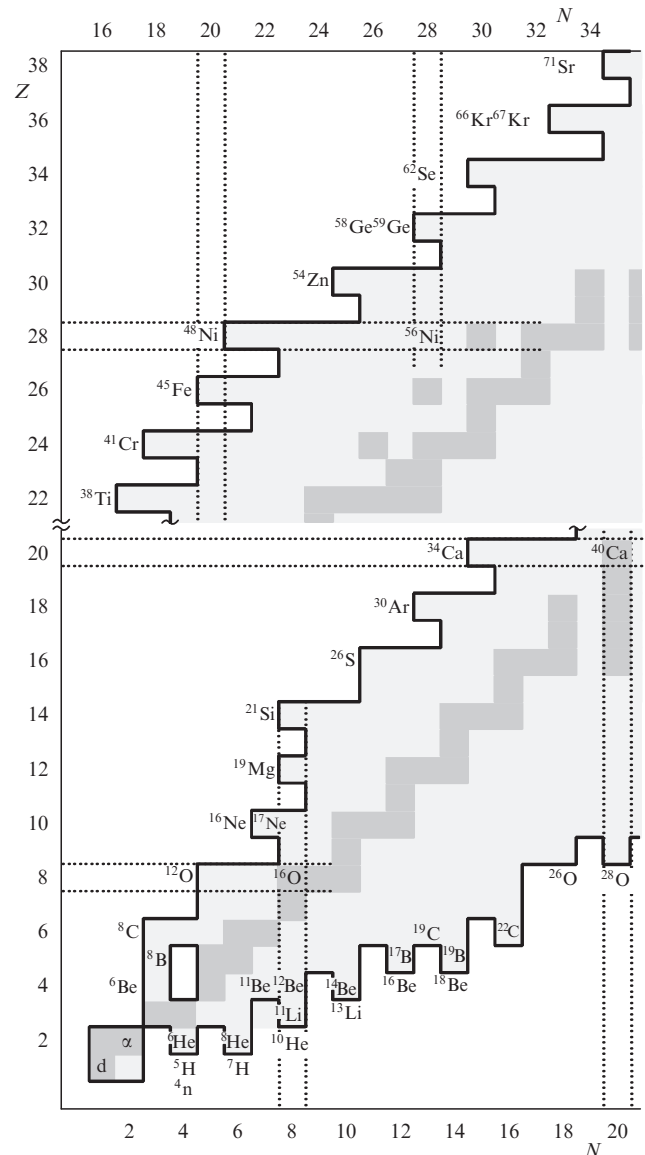
## 1. Introduction

It is well known that there is a total of 254 stable isotopes. However, 339 isotopes can be found in Nature: some unstable ones live long enough to survive either directly after the time of secondary nucleosynthesis or after they are produced as decay products of shorter-living precursor nuclei. From the point of view of nuclear physics, the property of ‘stability’ is less important than the concept of ‘nuclear stability’ or stability with respect to the strong interaction. The chart of stable nuclides is an analog of the Periodic Table of elements for the ‘world of nuclides,’ and as of today it includes about 3100 nuclear-stable isotopes [1]. It is useless to provide exact number, because studies in this field are very active and the number of known isotopes increases annually by 3–10. Theoretical predictions here are not very reliable, but in general it is expected that 2000–3000 more nuclear-stable isotopes exist. Expansion of the investigated region in the chart of nuclides and in-depth studies of new isotopes are the subject of research with radioactive ion beams (RIBs).

The physics of RIBs is nowadays one of the most actively developing field of nuclear science. The major concepts of research facilities in this field are already well developed. About fifteen years ago, the main research centers in the world entered a phase of massive upgrades of their experimental base with the application of modern technologies. The total worldwide budget for the new generation of facilities—so-called factories of radioactive ion beams—is close to 10 billion euros. This amount is comparable with the budgets of the most expensive scientific human enterprises: high-energy particle physics research and space research.

The status of current research of exotic nuclei with the charge numbers  $Z < 40$  is provided in Fig. 1. The drip lines (the borderlines of nuclear stability) with respect to spontaneous emission of neutrons/protons are achieved and studied to some extent only for the lightest nuclei. Information about nuclear systems near the drip lines and especially beyond is scarce and contradictory already for nuclei with  $Z > 5$ . This area of the nuclear chart is expected to be one of the major attractions for the RIB community in the forthcoming years. It can be seen in Fig. 1 that for drip-line nuclei with  $Z < 40$  there appears a broad field for pioneering theoretical and experimental studies. As we approach the borderlines of nuclear stability, we face qualitatively new phenomena of nuclear dynamics (see Sections 1.1 and 3).

The question about the borderlines of nuclear stability can be generalized to the question about the *limits of the existence of the nuclear structure*. The drip line is formally defined by the position of nuclides for which the separation energy of any fragment (nucleon, several nucleons, alpha-particle, or heavier cluster) becomes negative. However, it is clear that for decays via particle emission with sufficiently low decay



1 MeV, and are given as follows:

$$\Gamma = \frac{4.56 \times 10^{-22} [\text{MeV s}]}{\ln 2\tau [\text{s}]}.$$

The study of such short-lived systems is only possible in nuclear reactions. The range of practical problems and developed techniques, both experimental and theoretical, ultimately related to this fundamental task and worked out in the Flerov Laboratory of Nuclear Reactions (FLNR) at Joint Institute for Nuclear Research (JINR) is the main subject of this review [2–7].

The layout of the paper is as follows. Various general aspects of RIB physics are described in Sections 1.1–1.6. Section 2 provides motivation for the use of direct reactions at intermediate energies for RIB research. Section 3 discusses some nontrivial theoretical results concerning manifestations of the few-body dynamics in drip-line nuclei. We presume related experimental studies to be one of the priorities in RIB physics today. The instruments and experimental techniques applied at the ACCULINNA fragment separator<sup>2</sup> in FLNR are discussed in Section 4. The most significant experimental results obtained with this facility within the last 20 years are presented in Section 5. Implemented research projects [ACCULINNA-2, EXPERT (EXotic Particle Emission and Radioactivity by Tracking)] and possible future long-term developments in RIB physics are discussed in Section 6.

The system of units  $\hbar = c = 1$  is used throughout the review.

### 1.1 Qualitatively new phenomena at the drip lines

One of the major concepts underlying nuclear physics is the statement about the density saturation of nuclear matter. According to this concept, which emerged at the beginning of the 1930s, nuclear matter predominantly behaves like an almost incompressible fluid of nucleons. This straightforwardly leads to the liquid drop model of the nucleus. It is worth mentioning the two best-known consequences of this model approach: the relation between the root-mean-square nucleus radius  $r$  and the mass number  $A$ :

$$r = r_0 A^{1/3}, \quad r_0 = 1.2 \text{ fm}, \quad (1)$$

and the famous Bethe–Weizsäcker formula for the nucleus binding energy:

$$E_b = a_v A - a_s A^{2/3} - a_c \frac{Z^2}{A^{1/3}} - a_A \frac{(A-2Z)^2}{A} - \delta(A, Z).$$

Here, the first three terms (those with coefficients  $a_v$ ,  $a_s$ ,  $a_c$ ) correspond to the volume, surface, and Coulomb energies, and they are a direct consequence of the notion of a nucleus as a liquid drop. The last two terms are connected with peculiarities of the nuclear dynamics and provide corrections allowing for the asymmetry of nuclear matter (i.e., how far is the nucleus from the  $N = Z$  line, corresponding to coefficient  $a_A$ ) and for pairing interaction [function  $\delta(A, Z)$ ].

The idea of representing the nucleus as a drop of nuclear matter often fails near the drip lines. The clustering phenomenon begins to play an important role here. The drip line, by definition, is the location where the emission threshold of a nucleon (two or more nucleons, a cluster or two clusters)

becomes equal to the ground state (g.s.) energy of the nucleus. It is quite natural that nuclear states near thresholds attain the corresponding clustered structure [8]. Because of clustering, different characteristic scales appear in the nuclear system. They are associated with the motion of nucleons inside clusters and the motion of clusters relative to each other. So, considering the separation of a single nucleon (or a few nucleons), one argues in terms of ‘valence’ and ‘core’ nucleons.

When the separation energy for a nucleon (a few nucleons) tends to zero, the wave function of such a valence nucleon (valence nucleons) starts to take on an extreme radial extension. This phenomenon received the name *nuclear halo*. The nucleus becomes similar to a planetary system with a compact core and valence nucleons which spend most of their time in the classically forbidden region far beyond the core boundaries. In atomic physics, some analog of such a phenomenon is demonstrated by Rydberg atoms. However, it should be noted that Rydberg atoms reside in a quasistationary excited state, while halo nuclei are nuclear-stable ground state systems. In heavy neutron-rich nuclei, there is another manifestation of the halo-like structure: the formation of the so-called *neutron skin*—a layer of pure neutron matter on the surface of a nucleus. Near the drip lines, the separation of scales for nucleonic degrees of freedom, associated with a halo or skin, leads to manifestation of specific mechanisms of nucleus excitation. To distinguish these mechanisms from standard resonant excitation mechanisms, the notion of *soft excitation modes* is introduced. Among them, the *soft dipole mode* (SDM) is the most discussed.

One of the major concepts offering some insight into the nuclear structure is the phenomenon of pairing: two neutrons or two protons ‘prefer’ to be in a correlated state with zero spin, forming a bosonic quasiparticle. From a theoretical point of view, the pairing has the same roots as the origination of superconductivity and superfluidity in the motion of electrons and atoms. Pairing clearly manifests itself at the drip line: it can be seen in Fig. 1 that nuclei with an even number of neutrons or protons are more stable. This leads to the formation of characteristic ‘ridges’ on the border of stability. The nuclei which are located at these ridges often possess special forms of nuclear dynamics, which can be characterized as a *few-body dynamics* at the drip line. The best-known phenomena of this type are the so-called Borromean nuclei exhibiting a two-nucleon halo, two-proton radioactivity, and democratic decays (true three-particle decay). It is also possible that novel types of radioactivity, such as two-neutron and four-neutron radioactive decays, could be discovered there.

Theoretical studies of several few-body dynamics phenomena in light exotic nuclei, conducted in the team affiliated with the ACCULINNA fragment separator, are discussed in Section 3.

### 1.2 Applied aspects of radioactive isotope studies

There are several well-known applications of radioactive isotopes: in methods of radiation control, for the production of radioisotope power sources, and in nuclear medicine. Previously, these developments were often based on general-purpose scientific installations. Nowadays, however, they are mainly realized at dedicated commercial facilities. Here, we would like to point to the applied aspect of RIB research related to other fundamental problems in the natural sciences.

<sup>2</sup> Historically, ACCULINNA is not an acronym but a derivative from the female Russian name Akulina.

**1.2.1 Fast processes of nucleosynthesis.** Theoretical calculations of nucleosynthesis are based on two main constituents: the astrophysical scenario, and nuclear physics data. The astrophysical scenario specifies the initial conditions of nucleosynthesis and the time evolution of temperature and pressure. Nuclear physics data should preferably be provided by nuclear experiment; however, this is not always possible.

A list of required nuclear data may be quite extensive, in particular:

(1) it is imperative to know the mass of each involved nuclide in order to determine those processes in which it can participate;

(2) knowledge of the excitation spectrum up to several MeV, possibly with spin-parity identification, might be demanded;

(3) cross sections of various reactions may be required, at least the cross sections for the most abundant components of the astrophysical medium: protons, neutrons, alpha-particles, etc.

For ‘hydrostatic’ burning nucleosynthesis (normal star evolution), large volumes of the necessary information are already available. In this case, the nuclear systems involved are located near the stability valley, and the history of their study is typically several decades long. Fast processes of nucleosynthesis are considered in two main scenarios. In a core-collapse supernova, so-called r-process, nucleosynthesis occurs in a neutron-rich medium, so it proceeds along the neutron drip line. In explosive hydrogen burning on the surface of neutron stars (this rp-process is assumed to be responsible for gamma-ray bursts), the nucleosynthesis proceeds along the proton drip line. Thus, the ‘trajectories’ of fast nucleosynthesis processes are located in the vicinity of the drip lines in the chart of nuclides. These areas have been insufficiently explored or are just still totally unknown. Until the experimental RIB research advances in these areas, our understanding of the fast nucleosynthesis processes will be based on guesses and extrapolations, not always being reliable.

**1.2.2 Nuclear structure studies far from the stability valley.** One of the most interesting and promising fields of modern nuclear physics is connected with the study of the structure of exotic nuclei. Such nuclei in the vicinity of drip lines often possess features of the structure, which substantially distinguish them from ‘ordinary’ nuclei near the stability valley. Models of nuclear structure have been formulated on the basis of data obtained for nuclei in the vicinity of the stability valley. Extreme characteristics of nuclei, determined by the low binding energy of valence nucleons and the anomalous charge asymmetry of nuclei far from the stability valley, provide conditions for extended validation of nuclear structure models.

**1.2.3 Equation of state of asymmetric nuclear matter.** The problem of developing an equation of state for asymmetric nuclear matter is closely related to the problem described above in Section 1.2.2, but it is mainly relevant to astrophysics. The interpretation of astrophysical data of various types is often based on the understanding of neutron star properties. Here, reliable information about the properties of neutron matter is required. The global characteristic of neutron matter is reproduced by its equation of state. To deduce the equation of nuclear state, until recently we could only rely on experimental results concerning ordinary nuclei near the stability valley, which corresponds to a situation of

nearly symmetric nuclear matter (the stability valley deviates markedly from the  $N = Z$  line only for sufficiently heavy nuclei). Neutron nuclear matter is the opposite limiting case of maximum unbalanced nuclear matter in terms of the neutron-to-proton number ratio. Apparently, studies of nuclei in the vicinity of drip lines and, thus, far from the region of symmetric nuclear matter should make an important contribution to the solution of this problem.

### 1.3 Methods of RIB production

The study of nuclei in the vicinity of nucleon drip lines meets a great experimental challenge. Production of RIBs became possible due to progress in accelerator technology and isotope separation methods.

Electromagnetic separators made possible effective extraction of and manipulation with exotic radioactive nuclei for studies of their own properties, for studies of nuclear reactions with RIBs, and for the production and investigation of isotopes even more remote from the stability valley in the chart of nuclides.

Historically, the first method of RIB production was termed ISOL (Isotope Separation On-Line). The target nucleus (usually uranium) was disintegrated by bombarding it with light particles — p, d, n — or in a photofission reaction (induced by bremsstrahlung of incident electrons). Disintegration products are ejected or diffuse from thin target foils and are picked up by a stream of inert gas. The ISOL method was intended to solve the problem of radiochemical separation of radioactive isotopes: the short-lived beta-decay species disappear within times ranging between 0.1 and 1 s. So, separation and transportation of such nuclides to a detecting system should be performed in a comparable time. Modern ISOL methods provide separation times on the order of 100 ms.

Significant advantages in the separation time, range, and intensity of RIBs have been connected with the development of the *in-flight* separation method. In this method, RIBs were usually obtained in a fragmentation reaction by impinging beams of stable nuclei on a (usually light) target. Subsequent step-by-step purification from unwanted reaction products was performed by a special type of spectrometer — a fragment separator. In-flight separated beams allow the properties of the most short-lived nuclei near the drip lines (half-life  $T_{1/2} > 50$ –200 ns) to be explored. In highly specialized experiments, radioactive decays with lifetimes on the order of several picoseconds can be examined (see, e.g., Ref. [9] and also Section 6.3). The exceptionally high quality and complexity of modern RIB experiments can be illustrated by the following simple estimate. In a typical experiment of this type,  $\sim 10^{10}$  incident nuclei per second hit the primary (production) target. If in an experiment lasting about 100 hours, 1–10 exotic nuclei of interest are expected to be observed, then the required selectivity of the experimental setup should be on the order of  $10^{15}$ .

### 1.4 Main RIB factories and prospective projects

For many years, one of the world leaders in the field of RIB studies has been the research center GSI (Gesellschaft für Schwerionenforschung) in Darmstadt (Germany) [10]. Leadership was ensured by the heavy-ion SIS-18 synchrotron, which could accelerate various nuclides up to uranium with energies of  $\sim 1$  GeV/nucleon, and by the largest (until recently) fragment separator FRS (FRagment Separator) for in-flight RIB production. Among the most important

research instruments at GSI is the ESR (Experimental Storage Ring), which allows unique nuclear and atomic physics studies with completely or almost completely stripped heavy ions. Currently, the GSI research program is significantly limited because it is in the process of transformation into the new FAIR (Facility for Antiproton and Ion Research) international research center [11]. The new FAIR facility was developed with a significant Russian contribution; see Section 6.3 concerning one of the aspects of scientific cooperation within this program. FAIR is planned to start operation in approximately 2024–2025, and it should become the most powerful RIB ‘factory’ in the world. It includes the SIS-100 synchrotron providing a uranium beam with an energy of  $\approx 2.4$  GeV per nucleon with an intensity up to  $10^{10} \text{ s}^{-1}$ , and Super-FRS, the largest (length of about 140 m) fragment separator.

The Japanese RIB center RIKEN (Saitama) [12] was the first to enter the stage of massive upgrade at the end of the 1990s with the project RIBF (RIKEN Beam Factory). The method of in-flight separation using the superconducting fragment separator BigRIPS (Big RIKEN Projectile fragment Separator) was first implemented within this project. For the last seven years, RIBF has provided the best opportunities for RIB studies with primary beam energies of  $\approx 450$  MeV per nucleon.

The leading U.S. RIB center is NSCL (National Superconducting Cyclotron Laboratory) in East Lansing (Michigan) [13]. The characteristic feature of this Lab is its location in a compact building complex directly on the campus of MSU (Michigan State University). The FRIB (Facility for Rare Isotope Beams) program of the NSCL upgrade provides the deployment of a new RIB complex at the old site by 2022. FRIB utilizes a twice folded linear superconducting accelerator of heavy ions, delivering primary beams with energies of  $\approx 300$  MeV per nucleon. The RIB factory will have a mixed design with the main program associated with in-flight technology, but the accelerator will also be utilized as a ‘driver’ of the ISOL facility.

The GANIL (Grand Accélérateur National d’Ions Lourds, Kaen, France) research center [14] in the late 1980s was one of the pioneers in applying the in-flight method for RIB studies with the LISE (Ligne d’Ions Super Epluchés) fragment separator. However, the upgrade project SPIRAL2 (Système de Production d’Ions Radioactifs en Ligne de 2 generation) being deployed at the old site was chosen to be an ISOL type (the launch is scheduled for 2020). Within this project, RIBs are obtained in the neutron-induced fission of uranium at a record-high intensity for ISOL facilities up to  $10^{13}$  fissions per second. Neutrons are generated by the stripping reaction from an intensive deuteron beam: 30-MeV deuterons with an intensity of  $\approx 10$  mA are delivered by a linear accelerator.

In addition to major RIB centers, there are several ‘second echelon’ facilities working in this field. It is worth mentioning here the centers in Legnaro (Italy), the University of Jyväskylä (Finland), Stellenbosch (South Africa), Oak-Ridge (USA), Lanzhou (China), the ISAC facility in the Triumf center (Vancouver, Canada), and the ISOLDE (ISOL Device) facility at CERN. There are as well ambitious initiatives to construct advanced RIB facilities with an estimated cost of about 1 billion euros each: the South Korean project KOBRA (Korea Broad acceptance Recoil spectrometer Apparatus) and the Chinese project HIAF (High Intensity heavy ions Accelerator Facility).

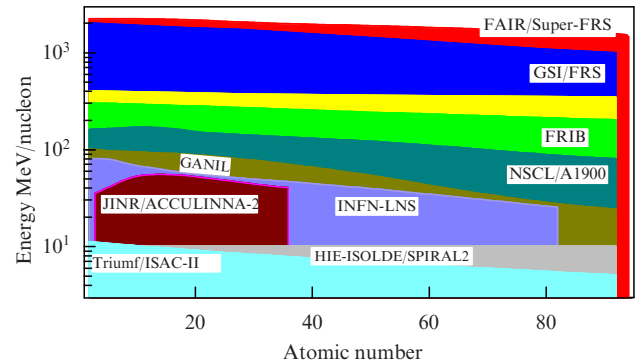


**Figure 2.** (Color online.) Capabilities of modern RIB facilities. Various colors show the ranges of energies and particles available at different research institutions/facilities. Technical characteristics of some of these facilities are provided in Table 4 (see Section 6). INFN-LNS is the one-letter abbreviation for Istituto Nazionale Fisica Nucleare Laboratori Nazionali del Sud in Italy.

The largest RIB facilities in the world (in existence and under construction) and their capabilities are illustrated in Fig. 2. In Eastern Europe and in the countries of the former Soviet Union, RIB physics is being developed now only in JINR FLNR (see Section 1.6 and Table 4).

### 1.5 Typical research methods with RIBs

The first information obtained about a new isotope is typically just the fact of its existence. The majority of isotopes discovered in recent decades were observed in experiments with fragment separators. In this case, the mass number and the ion charge are determined from the time of flight and energy loss in detectors located near the final focal plane of the fragment separator. Other information that becomes simultaneously available in such an experiment is the lower bound for the lifetime: to get to the final focal plane, the lifetime of the nuclide must be longer than its time of flight through the fragment separator. For typical 15–50 m length of facilities and velocities ranging  $(0.3–0.6)c$ , the typical lifetime lower bounds of  $\tau > 50–200$  ns can be established.

Next in importance is information about the mass of the nuclide. Expecting a mass measurement accuracy of 100 keV and better, it is necessary to use spectrometric facilities with a relative resolution of at least  $10^{-5}$  for light nuclei, and  $10^{-6}$  for heavy ones. Such a precision can be achieved in magnetic traps (e.g., the Penning trap) [15, 16] or in storage rings operating in the isochronous mode [17, 18]. The latest trend in this field is the development of MR-ToF (Multiple-Reflection Time-of-Flight) mass spectrometers, in which a slow beam gains a huge flight distance due to multiple reflections from electromagnetic mirrors [19]. All these methods are ‘slow’, i.e., require not less than 1 s of measurement time. Therefore, the determination of the masses of short-lived nuclides is only possible implementing nuclear reactions.

Registration of gamma-rays from decays of RIB excited states makes possible spectroscopic studies. Since a typical gamma-decay time is as small as  $10^{-15}–10^{-12}$  s, the measurement should be carried out directly at the point of RIB formation (within such a time, even a nuclide in a relativistic beam is unable to fly out some macroscopic distance). Work with low-intensity and highly contaminated RIBs in the vicinity of the secondary target region with complicated background conditions requires special approaches to gamma-ray spectroscopy [20].

Nuclei located far from the valley of stability are transmuted into more stable systems due to ‘weak’ processes ( $\beta^-$ - and  $\beta^+$ -decays or electron capture). Because of structural peculiarities of isobaric multiplets, weak transitions mostly populate the excited states of the daughter nuclides. If these excited states are located above the emission thresholds of nucleons or even clusters, we face a situation of  $\beta$ -delayed emission of particles. Studies of  $\beta$ -decays and  $\beta$ -delayed emission of particles cover a priority area for experiments with RIB implantation in the detecting system.

A special field of research comprises studies of ‘strong’ decays (including ‘strong’ radioactive decays), i.e., processes with the emission of particles ( $\alpha$ , p, 2p, n, 2n). While  $\alpha$ -decay belongs to the three basic types of radioactivity ( $\alpha$ ,  $\beta$ , and  $\gamma$ ) discovered by A Becquerel in 1896, the discoveries of proton (p) radioactivity [21] (1982) and two-proton (2p) radioactivity [22, 23] (2002) (see Section 3.4) are among the relatively recent achievements of RIB physics. The question of the possible existence of novel types of radioactive decay connected with the emission of several neutrons, such as 2n- and 4n-decays, was recently considered in paper [24] (see Section 3.8). The current status of radioactive decay studies near the edges of nuclear stability is discussed in review [25].

The study of the decay of a nuclear system can give very precise information about certain aspects of its structure, namely, about the specific matrix elements for processes in this system. However, this method of research can be seen as a kind of ‘passive’ approach: here, only that information which Nature itself ‘agrees’ to provide can be obtained.

A truly flexible approach to the investigation of RIBs consists in studying nuclear reactions. Nuclear physics accumulated a rich arsenal of different reactions at its disposal: knock-out, stripping, pickup, charge exchange, Coulomb excitation, quasifree scattering, etc. The particular choice of which kind of reaction to utilize strongly depends, of course, on available energy, possible kinematics for the experimental setup, and other technical limitations. However, there is considerable freedom in choice, which allows one to focus on reactions that fully reveal the physical aspect of interest. For example, the second most often performed RIB experiment (after the discovery of new isotopes) is the study of the momentum distributions of residues from reactions of nucleon (or nucleon pair) stripping. Such reactions have large cross sections, the experiments are relatively simple, and the information obtained immediately imposes strong constraints on the possible properties of valence orbitals—their angular momenta and nucleon separation energies.

In this review, we focus on nuclear reactions as a method of obtaining information about exotic nuclei.

### 1.6 RIB studies in the Flerov Laboratory of Nuclear Reactions

In the 1990s, JINR FLNR managed not only to maintain a scientific program at the world level, but also to achieve breakthrough results in certain areas. First of all, the program of superheavy element (SHE) synthesis should be mentioned here, which made FLNR a world leader in this field. This program led to the discovery of chemical elements with charge numbers  $Z = 113$ – $118$  in the last two decades. In recognition of FLNR’s achievements in this field, the International Union of Pure and Applied Chemistry (IUPAC) assigned the official names for elements

with  $Z = 114$  (Flerovium) and  $Z = 116$  (Livermorium).<sup>3</sup> It can be presumed that now we are very close to completion of the Periodic Table, as  $Z = 120$  is probably the charge number of the last chemical element.<sup>4</sup>

Continuation of the SHE synthesis and study program at FLNR will be provided by construction of the specialized ‘SHE factory’ taking aim at the months-long search for super-rare events of SHE formation with typical cross sections of 1–100 fb (for comparison, the typical nuclear cross section has a scale of 1 b, or 100 fm<sup>2</sup>, which is 10<sup>15</sup> fb). Commissioning of the SHE factory will allow the FLNR accelerators to be freed up for a variety of other experimental tasks, in particular, for studies with RIBs.

It should be noted that the search for SHE, although aimed at expanding the chart of nuclides in one of the most extreme radioactivity areas, does not directly belong to research with RIBs. These experiments are conducted with the employment of very intensive 0.5–2.0  $\mu$ A (particle microampere, 1  $\mu$ A =  $1(e/Z)$   $\mu$ A) and very neutron-rich (such as <sup>48</sup>Ca and <sup>50</sup>Ti), but still stable, beams. The use of neutron-rich RIBs, of course, could lead to a breakthrough in this field, but the production of secondary beams with an intensity sufficient for the SHE search is still an unresolved problem.

The Flerov Laboratory of Nuclear Reactions operates the RIB accelerating complex DRIBs-1 (Dubna Radioactive Ion Beams 1). DRIBs-1 includes the in-flight facility ACCULINNA [26] and devices which deliver low-energy RIBs at the U-400 cyclotron for a number of light radioactive nuclei separated by the ISOL method. The latter installation requires the operation of two accelerators, U-400M and U-400, in tandem: the first produces RIBs by irradiating a thick target with an intense beam, and the second subsequently accelerates the selected RIB to an energy of  $\approx 6$  MeV per nucleon [27]. Prospects for the further development of ISOL type methods at JINR are discussed in Section 6.2.

The ACCULINNA separator started operation in 1996; the DRIBs-1 complex has been fully functioning since 2004. The results of the work performed at DRIBs-1 are presented in numerous articles and conference reports (see, e.g., Ref. [2]). Now, the Flerov Laboratory resides in the third phase of developing infrastructure for getting intense RIBs, which is called DRIBs-3. One of the most promising parts of this program is the study of light exotic nuclei in the vicinity of the drip lines at the ACCULINNA and ACCULINNA-2 facilities.

The ACCULINNA fragment separator (see Section 4.2), built in the mid-1990s, was initially planned as one of the first elements of the K4–K10 project. The K4–K10 project of massive upgrade of the FLNR research infrastructure was approved in 1989. It was aimed at taking world leading positions in the field of RIB studies [28]. The project was cancelled for obvious reasons. However, the general design of the K4–K10 complex with two storage and accelerator rings was later used in Lanzhou (China) [29], and the idea of an electron–RIB collider proposed in the K4–K10 project

<sup>3</sup> Lawrence Livermore National Laboratory and Oak Ridge National Laboratory (USA) actively participated in joint experiments on the SHE synthesis. In December 2015, IUPAC officially recognized the discovery of the elements  $Z = 115$ , 117, 118, made by a collaboration with leading contributions from JINR FLNR.

<sup>4</sup> It is assumed that we are talking about sufficiently long-lived (a few milliseconds?) isotopes.  $Z = 120$  is the closest nuclear magic number to the already achieved  $Z = 118$  according to the most simple estimates. There are, however, theoretical models with maximum  $Z = 122$ , or even higher, up to  $Z \sim 164$ .



inspired the ELISE [Electron-Ion scattering in Storage ring (eA-collider)] experiment [30] within the currently constructed FAIR facility. The effectiveness of the scientific program carried out with the ACCULINNA facility became the basis for developing the concept and subsequent construction of a new fragment separator, ACCULINNA-2. This fragment separator, built in collaboration with French ion-optical systems supplier SigmaPhi in 2011–2015, is now at the stage of commissioning and preparation for ‘first day’ experiments (see section 6.1).

## 2. Direct reactions at intermediate energies

Investigations of direct reactions at intermediate energies proved to be a useful approach to RIB experiments. Highlighting the reasons let us, first, briefly define this subject.

Direct reactions comprise the wide spectra of nuclear reactions with a few nucleon (cluster) degrees of freedom. This assumes an adiabatic character of direct reactions, i.e., an interaction within selected degrees of freedom is faster than the typical time of a nuclear rearrangement. Therefore, this rearrangement does not have enough time to occur. Hence, the theoretical description here can be perturbative or close to it. If it is adequate to apply the first-order perturbation theory, the description can be especially simplified. These situations can be properly illustrated by pole diagrams (Fig. 3), on the basis of which several important qualitative conclusions can be made. The reaction of interest has a preferential direction (this fact distinguishes it from the process of spontaneous decay). Obviously, beam direction (vector  $\mathbf{k}$ ) specifies it. Moreover, in direct reactions with the pole mechanism, the other additional preferential direction becomes physically important. This direction is given by the momentum transfer vector  $\mathbf{q}$ . The existence of this preferential direction provides us with several important consequences: the realization of Treiman–Yang criteria [31, 32], and the possibility of forming a significant alignment in the direction of  $\mathbf{q}$  (see Section 2.3).

By intermediate energies<sup>5</sup> are meant a fairly conventional range of 20–60 MeV per nucleon. They are significantly

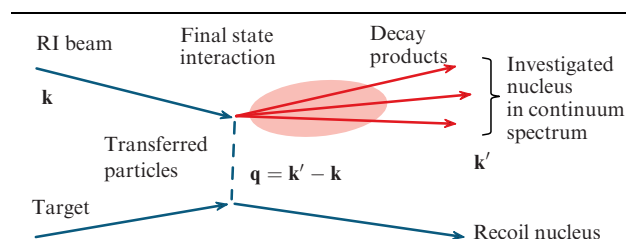


**Figure 3.** Schematic representation of the direct-reaction pole mechanism with the population of the exotic nuclear system continuum states. The final state interaction should be considered while analyzing the spectrum of the investigated nucleus. It is assumed that a final state interaction between any of the decay products and a recoil nucleus can be disregarded due to the kinematic separation. The kinetic energy of motion of any of the decay products in relation to the recoil is at least an order of magnitude larger than the relative motion energy of the decay products.

<sup>5</sup> There is a significant lack of consistency in treating the term ‘intermediate energies’. Sometimes, the term is used together with ‘medium energies’ to define an extra energy interval. For different fields of nuclear physics, the boundary points are the transitions between underbarrier and near-barrier reactions, the excitation energies of giant resonances, the excess energy threshold for pion production, or the transition to the relativistic situation upon an excess of the nucleon mass. As will be shown in Section 2.1, the transition from the domination of transfer reactions to the prevalence of knock-out reactions is important for the discussed field of studies.

higher than the Coulomb barrier (1–7 MeV per nucleon for light nuclei), but are still far from relativistic energies (100 MeV or higher per nucleon) and from the related experimental problems. Reactions in such a range of energies are sufficiently fast to proceed by the direct mechanism and the kinematics allows a significant contribution of the various direct reaction mechanisms, i.e., the stripping, pickup, transfer, exchange, and charge exchange of one or several nucleons. The criterion that determines the effectiveness of the above mechanisms is the approximate equality of the momentum per nucleon in the incident nucleus to the typical Fermi momentum for the system.

Overall, the result of a nuclear reaction is determined by the following main ingredients: (1) the initial nuclear structure of the reaction participants; (2) the reaction mechanism; (3) the structure of the exotic nuclear system formed in reactions with RIBs, and (4) the interaction of the fragments in the final state. If the subject of the investigation is ingredient number 3, then for obtaining the important information it is necessary to correctly account for the remaining items in the list above. Assuming that the nuclear structure of initial, less exotic, nuclear systems is understood relatively well and the interaction processes in the final state are adequately described by modern theoretical methods, the most important becomes to understand the second ingredient—the nuclear reaction mechanism. In direct reactions, the mechanism is relatively simple. And if certain experimental conditions are selected, a number of well-developed, relatively simple, and reliable theoretical models adequately describing the reaction mechanism are found on hand: PWIA (Plane-Wave Impulse Approximation), DWBA (Distorted Wave Born Approximation), QFS (Quasi-Free Scattering), eikonal models, the Glauber model, and so on [33–35].

### 2.1 Advantages and drawbacks of reactions at different energies

Modern RIB factories follow the tendency of increasing the energy of RIBs. The motivations for different facilities are various.

In the ISOL method, secondary nuclei have a very low energy (a few keV or tens of keV) after extraction from the target. This allows one to transport the RIBs for further implantation into the detecting system or injection into an electromagnetic trap. Reactions with RIBs cannot be effectively studied at those low energies. The secondary beam has to be post-accelerated. At many ISOL factories post-acceleration of their RIBs to energies of 5–20 MeV per nucleon is implemented in order to study the reactions with RIBs.

For ‘in-flight’ RIB factories, the tendency towards high energies has several principal arguments.

- The increase in the primary beam energy allows using the thicker primary (production) target. This results in increasing the efficiency of the use of the primary beam. So, if the production target is 1 cm thick and made from a light material (beryllium), only  $\sim 20\%$  of the primary beam will be utilized. Let us take  $^{36}\text{Ar}$  as an example. In order to have an energy loss in the target of less than 20%, the required energy should be more than 250 MeV per nucleon.
- The primary reaction fragments are focused in a narrow cone in the forward direction. This increases the efficiency and the quality of the fragment separator’s work.
- Very thick secondary (physical) targets can be used for experiments. This is especially important for investigations of RIBs with an ultimately low intensity. Thus, experimentation

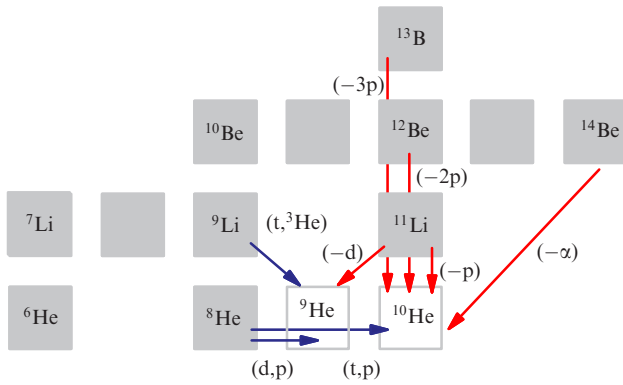


**Figure 4.** (Color online.) Possible reactions leading to the formation of a system beyond the neutron drip line. As an example, the formation of superheavy helium isotopes is illustrated. Reactions with high energies are shown in red. Alternative methods of forming exotic systems in the 1n, 2n transfer and charge exchange reactions are shown in blue.

[36] with a 27-mm thick beryllium target irradiated by an  $^{31}\text{Ar}$  beam with the intensity of only  $\sim 10^3 \text{ s}^{-1}$  resulted in the discovery of a new  $^{30}\text{Ar}$  isotope and obtaining a sufficiently detailed spectroscopic data about this rare isotope.

- With an increase in the beam energy, the adiabatic character of direct reactions becomes more explicit. At the same time, it becomes possible to apply simple theoretical approaches to the nuclear reaction mechanism and the reliability of the retrieved structural information is also enhanced.

The above-mentioned advantages of high-energy RIBs lead to a number of problems.

- The cross sections of the majority of direct reactions are reduced to a level excluding their practical use. In fact, the only reactions available for study become the ones with nucleon or cluster knock-out. This means that, for example, from the exotic neutron-rich system  $\{A, Z\}$  we can move to more exotic systems:  $\{A-1, Z-1\}$  by knocking out a proton, to  $\{A-2, Z-2\}$  by knocking out two protons, and to  $\{A-4, Z-2\}$  by knocking out  $\alpha$ -particles. At the lower energies of RIBs ( $< 60 \text{ MeV}$  per nucleon), superexotic nuclear systems can be formed in a quite different way: as a result of transfer reactions of one or two nucleons, and charge exchange reactions (Fig. 4).

- The only method of identification of the desirable system obtained in the knock-out reaction is the method of invariant mass. This method is applicable only at energies above the decay thresholds, and it requires the identification of all the decay products for the desired system. It is clear that if there are more than three such products (as, for example, in decay with the emission of four neutrons), then registration of all fragments in coincidence becomes a serious technical problem. At intermediate energies, relevant are the transfer reactions or QFS reactions, at which all the recoil nuclei are detected (see Fig. 3), and the use of the missing mass method—the detection of only recoils—and the method of combined mass (detection of recoils and several decay products) becomes possible.

- While working with the invariant mass method under relativistic conditions, the main source of errors resides in the measurement of the longitudinal momentum (the total energy of the fragment). Studies of reactions at intermediate energies allow us to reach a compromise while choosing among the desired accuracy of the energy characteristics of the system

(which requires low energy), the sufficient value of the secondary-reaction cross section (which also requires low energy), the high enough efficiency of secondary beam production (high energy required), and the simplicity of the reaction mechanism (high energy required).

- In the knock-out reactions, the resulting systems are formed in a rather nonspecific way in term of angular momentum alignment. This leads to the limitation of the correlation method functioning, which, as will be shown later, operate efficiently at intermediate energies.

The advantages of the direct reactions at intermediate energies are recognized by the scientific community. So, there is a subproject HISPEC (High-resolution In-flight SPECTroscopy) in the FAIR project, which is aimed at studying such reactions. The production of intermediate energy RIBs due to the strong inhibition of the beam in the absorber (the decrease in energy is more than 100-fold from the values of  $\approx 1500 \text{ MeV}$  per nucleon) is planned. As a result, enormous spatial and energy dispersions emerge. This leads to the development of rather expensive bulky detecting systems.

Project ISOLDE at CERN is developing different methods of secondary beam acceleration, starting from energies of  $3 \text{ MeV}$  per nucleon (REX-ISOLDE—Radioactive EXperiment at ISOLDE) and up to  $10 \text{ MeV}$  per nucleon (HIE-ISOLDE—High Intensity and Energy ISOLDE). The Canadian center Triumf realizes RIB post-acceleration to energies of  $5\text{--}15 \text{ MeV}$  per nucleon at the ISAC-II (Isotope Separator and Accelerator II) facility. However, there is a constraint in operation with short-lived RIBs (lifetimes less than  $100 \text{ ms}$ ) at the last two ISOL type facilities mentioned above.

Thus, it can be affirmed that the scientific program for studies of reactions at intermediate energies has good prospects for development. At the ACCULINNA facility of JINR FLNR, the research program based on the listed advantages and compromises in the choice of the RIB energy range has been successfully implemented over the last 20 years.

## 2.2 Correlations and spin-parity identification

Along with nuclear spectroscopy, one of the main sources of information on the structure of atomic nuclei and on nuclear interaction mechanisms comes from the measurement of angular correlations in reactions and decays.

The simplest example is the measurement of the angular distribution of reaction products, which can be regarded as a correlation between the incident beam direction and the emission angle of the detected particles being the products of the reaction. The angular distribution in the elastic scattering of spinless particles is given by the expression

$$\frac{d\sigma}{d\Omega} = \frac{1}{k^2} \left| \sum_l \frac{2l+1}{2} [\exp(2i\delta_l) - 1] P_l(\cos\theta_{\text{cm}}) \right|^2, \quad (2)$$

where  $\sigma$  is the scattering cross section,  $\Omega$  is a solid angle,  $l$  is the orbital angular momentum,  $P_l$  is the Legendre polynomial of the first kind, and  $\theta_{\text{cm}}$  is the scattering angle in the centre-of-mass system. In the vicinity of resonances (with the energy  $E_r$  and width  $\Gamma$ ), phase shifts are parameterized as follows:

$$\delta_l(E) = \arctan \left[ \frac{\Gamma}{2(E_r - E)} \right]. \quad (3)$$

A popular method for RIB studies is the elastic resonant scattering measured in the inverse kinematics in a thick target



(see, for example, articles [37–40] and references cited therein). Using the measured data on the energy and angular dependences of the cross section and applying expressions (2) and (3), it is possible to determine the resonance parameters, including spin-parity. In this case, if the *elastic channel is the only open one*, then the identification of the resonance states in the spectrum would be *unambiguous*. This is a nontrivial feature of elastic scattering. It is worth mentioning that quantum mechanics does not guarantee unambiguous correspondence of quantum numbers to the scattering data for inelastic processes, and we are faced with choosing a plausible model. Also, we notice that, in accordance with expression (2), when the isolated resonance with  $J = L$  is populated in the elastic scattering of spinless particles, the angular distribution takes the simple form

$$W(\theta_{\text{cm}}) \sim |P_J(\cos \theta_{\text{cm}})|^2. \quad (4)$$

Such a pronounced angular distribution makes trivial the experimental identification of  $J$  for a narrow isolated resonance.

The following method is widely used to identify the spin-parity in direct reactions (inelastic processes). It can be shown that for many types of direct reactions the shape of the angular distribution is mainly determined by the transferred angular momentum  $\Delta L$ . Qualitatively, this dependence is described by the expression

$$\frac{d\sigma}{d\Omega} = \sum_{J\Delta L} \frac{d\sigma_{J\Delta L}}{d\Omega}, \quad \frac{d\sigma_{J\Delta L}}{d\Omega} \sim |j_{\Delta L}(qr_0)|^2, \quad (5)$$

where  $j_{\Delta L}$  is the spherical Bessel function,  $q$  is the momentum transferred in the reaction, and  $r_0$  is a characteristic nuclear radius, for example,  $r_0 = 2-5$  fm. Sufficiently developed methods of cross-section calculations may exist for specific types of reactions, but the simple expression (5) in most cases correctly reproduces the position of the maximum and the first diffraction minimum and allows the easy determination of  $\Delta L$  in the first approximation.

The above-mentioned techniques are built around the angular distribution in the *center-of-mass system of all reaction products*. Much less known and popular is the method associated with the angular correlation measurements performed for the decay products of an *unstable subsystem*. As a simplified illustration, we first consider a classic example of spin identification in cascade decays with spinless particle emission in the ‘zero geometry’ (Fig. 5).

Let the excited compound state of  $^{28}\text{Si}^*$  be populated in the collision of  $^{12}\text{C}$  and  $^{16}\text{O}$  at the stage 1 (see Fig. 5). Assume that this state decays at stage 2 with the emission of an alpha particle ( $\alpha_1$ ), and the excited states of  $^{24}\text{Mg}^*$  with different

spins  $J = L$  are populated. The measurement of  $\alpha_1$  energies allows one to select the  $^{24}\text{Mg}^*$  state with a certain energy. If  $\alpha_1$  is detected at a zero angle relative to the beam direction, the spin of the selected excited  $^{24}\text{Mg}^*$  state is equal to the angular momentum  $J = \Delta L$  transferred in the reaction, since the spins of all the other participants in the reaction are equal to zero. This kinematic condition for cascade decays is called ‘zero geometry’. At the stage 3, the  $^{24}\text{Mg}^*$  state decays with emission of the second alpha particle ( $\alpha_2$ ). In general, the angular distribution over  $\theta$  should be expressed through a set of associated Legendre polynomials  $P_J^{M_J}$ :

$$W(\theta) \sim \left| \sum_{M_J} a_{M_J} P_J^{M_J}(\cos \theta) \right|^2, \quad (6)$$

with some amplitudes  $a_{M_J}$ . However, it turns out that, in the reference frame where  $\alpha_1$  is emitted parallel to the  $z$ -axis,  $a_{\pm 1} \equiv 0$  and the angular distribution of  $\alpha_2$  is also described by a simple expression like (4) but only dependent on the angle  $\theta$  in the center-of-mass frame of the subsystem  $^{24}\text{Mg}^*$ . The explanation is that the projection of the transferred angular momentum  $\Delta L$  onto the  $z$ -axis in such a system can only be zero ( $M_{\Delta L} \equiv 0$ ). It was zero initially, since all initial momenta were parallel to the  $z$ -axis, and remained zero, since  $\alpha_1$  cannot ‘carry away’ a nonzero projection of angular momentum. In the angular momentum theory, it could be formulated as the simplification of the correlation pattern related with the formation of the highly aligned intermediate state of  $^{24}\text{Mg}^*$ . The alignment corresponding to the condition  $M_{\Delta L} \equiv 0$  is characterized as the *polar* one, because it corresponds to the dominant emission of particles in the direction of the poles of the spherical system of reference.

This method was widely exploited primarily in the study of high-spin states of medium- $Z$  nuclei (see, for example, Ref. [41]). An essential constraint on this method is the requirement that the reaction participants be spinless. In addition, the spectrum of states populated in such reactions is limited by those with natural parity  $\pi = (-1)^J$ .

The idea of the ‘zero geometry’ method is easily generalized to the case of direct pole reactions. The reference frame should be oriented not in the beam direction but in the direction of the transferred momentum  $\mathbf{q}$  (for each event). For direct reactions, the cause of population of the highly aligned intermediate states is somewhat different from that in the ‘zero geometry’ case, but it might be easily explained qualitatively. The angular momentum  $\Delta L$  transferred in the reaction is derived from the transferred momentum  $\mathbf{q}$  and, hence, it can be obtained by vector multiplication of  $\mathbf{q}$  by a certain radius vector; therefore, it is orthogonal to  $\mathbf{q}$ . This implies that in the reference frame associated with  $\mathbf{q}$ ,  $\Delta L$  can only have the zero projection onto the  $z$ -axis:

$$\{[\Delta L \times \mathbf{q}] \equiv 0, z \parallel \mathbf{q}\} \rightarrow M_{\Delta L} \equiv 0. \quad (7)$$

The mathematical apparatus devised for describing the angular correlations in cascades of nuclear processes involving particles and electromagnetic radiation is presented in classical paper [42]. Significant materials on correlations in nuclear processes are contained in recent monograph [43].

The nonzero spins of the reaction participants significantly complicate the picture of the angular correlations. The result of the analysis is no longer guaranteed, to be as it is in the situation shown in Fig. 5. Even in this case, however, the angular correlation measurement in certain favorable conditions can be used for the spin-parity identification of the excited nuclear states populated in the reaction. For example,

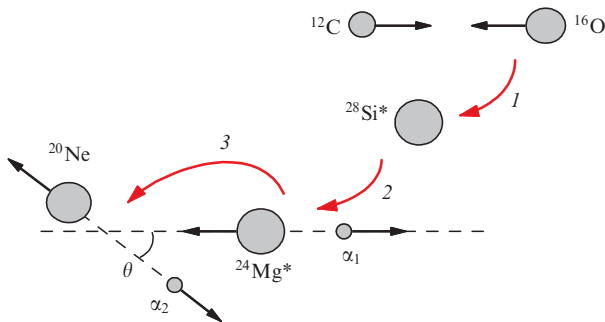


**Figure 5.** Spin identification in the ‘zero-geometry’ reaction by the example of the reaction  $^{12}\text{C}(^{16}\text{O}, 2\alpha)^{20}\text{Ne}$ .

when studying the alpha-cluster states of the p- and s-d-shell nuclei, the angular correlation measurements in the reaction ( ${}^6\text{Li}$ ,  $d\alpha$ ) found wide applications (see, for example, paper [44] and references cited therein). In Section 5, we will present a number of successful examples of the correlation studies made at the ACCULINNA facility for participant systems with spins.

While the characteristic angular correlations arise due to polarization (spin alignment) of the intermediate state in the example above, we encounter a fundamentally new phenomenon in moving towards the drip-line nuclei. The small binding energy of these exotic nuclei leads to the fact that the whole spectrum of excited states, and sometimes the ground state, lies above the decay threshold. Of special interest are those nuclei in which the two-particle decay threshold lies above the threshold of decaying to three or sometimes more particles. As an example of a three-particle emitter, we can look at the  ${}^6\text{Be}$  nucleus, with its ground state lying above the threshold of the decay into an alpha-particle and two protons, while in binary  ${}^6\text{Be}$  subsystems ( $\alpha$ -p or p-p) there are no intermediate resonances which could ensure a two-step decay of the ground state (see Sections 3.5 and 5.6). The angular correlation measurements on such systems can provide unique information on the nuclear structure and decay dynamics.

Another feature connected with studies of light exotic nuclei should be noted. Since the excited states of such nuclear systems typically reside above the nucleon decay threshold, the experimentally measured spectra represent a result of the overlap of broad states, which significantly complicates their interpretation. For example, in the measured missing mass spectrum in the reaction leading to population of low-lying states of residual nucleus, contributions from states with different quantum characteristics (due to their orthogonality) are not coherent. If the widths of the states are comparable to the distance between the levels, the result is an inexpressive, structureless pattern complicating, and often making impossible, the isolation of separate components in the spectrum. In angular correlations of the decay particles, interference effects can lead to the formation of a clear structural pattern. For example, the asymmetry of the angular distribution in the center-of-mass system of the decaying nucleus unambiguously testify to the interference of states with different parities.

Thus, it could be argued that the angular correlation measurement is a powerful tool for obtaining unique information. The correlation measurements are much more sophisticated than those based on traditional methods. In so doing, the experimental setup becomes much more complicated, requirements for statistics accumulated in the experiment increase, and data analysis becomes more time-consuming. However, all this must be paid by the creation of reliable information on the exotic nuclear structure and on the decay dynamics.

### 2.3 Monte Carlo simulations

Experimental data can be affected by three factors related to the experimental setup: (1) limited acceptance, when the particle flies past the detecting system; (2) low registration efficiency when the particle hits the detector but is not detected, and (3) errors caused by angular and energy resolutions, when the real attributes differ from the detected ones. The distortions are especially large in experiments with coincidence registration of several particles, when the

obtained spectra and correlation distributions might be distorted beyond recognition. Thus, the results of modern experiments of sufficient complexity cannot be directly compared with the theoretical predictions. The most common and sometimes the only available approach consists in applying the simulations by the Monte Carlo (MC) method. It is necessary to transform theoretical predictions (amplitudes in the momentum space) to *events* (sets of momentum vectors for all particles) which are distributed in phase space with the same probability density as those in the theory. Such events are then processed by a software filter maximally reproducing the experimental setup. The results of the simulations are analyzed using the same procedure as during experimental data processing. Theoretical results processed in this way are the only suitable ones for comparison with the experimental data.

From conceptual viewpoint, this means that, for experiments of sufficient complexity, self-standing theoretical results are no longer important. The problem of comparing calculated results with experimental data forces theorists to work on a team with the experimentalists. The MC procedure is processed from two sides: the theorists transform the probability densities to events, and the experimentalists create a simulator of the experimental setup. This requires a specific methods to organize the research process and accentuates questions of scientific ethics in working with data.

The density matrix formalism is applied for parameterization of cross sections of direct reactions populating continuum states:

$$\frac{d\sigma}{dq_{\parallel} dq_{\perp} dE_T d\Omega} \sim \sum_{SM_S} \sum_{JM, J'M'} \rho_{JM}^{J'M'}(q_{\parallel}, q_{\perp}, E_T) \times A_{J'M'SM_S}^{\dagger}(E_T, \Omega) A_{JMSM_S}(E_T, \Omega). \quad (8)$$

Two components of transferred momentum  $\mathbf{q}$  are clearly singled out: the longitudinal  $dq_{\parallel}$ , and transverse  $dq_{\perp}$ , as its azimuthal orientation with respect to the beam carries no physical information. The amplitude  $A_{JMSM_S}$  of the final state is summed over the spin states, since it is assumed, for now, that the study of spin degrees of freedom is irrelevant for experiments on radioactive ion beams because of the complexity. The factorization of the cross section in the form of expression (8) reflects the adiabatic character of direct reactions: it is revealed by the ‘fast’ (density matrix  $\rho_{JM}^{J'M'}$ ) and the ‘slow’ (amplitudes of the decay channel of interest) components. The  $E_T$  energy is measured above the decay threshold of the system, and the amplitudes  $A_{JMSM_S}$  in Eqn (8) can be both the two-particle and three-particle ones. Accordingly, the solid angle  $\Omega$  will be two-dimensional or five-dimensional (see the discussion of variables for the three-body problem in Sections 2.4, 3.1):

$$\begin{aligned} \Omega \rightarrow \Omega_2 &= \{\theta, \phi\}, \\ \Omega \rightarrow \Omega_5 &= \{e, \Omega_{kx}, \Omega_{ky}\} = \{e, \theta_k, \alpha, \beta, \gamma\}. \end{aligned} \quad (9)$$

As a consequence, we have a five-fold differential cross section, which is still acceptable, for reactions with a two-particle final state, while it will be eight-fold for a three-particle final state cross section, which poses a substantial numerical problem.

It is desirable to make predictions both for amplitudes  $A_{JMSM_S}$  of the process considered and for the reaction mechanism encoded in  $\rho_{JM}^{J'M'}$ . However, the problem of

finding  $\rho_{JM}^{J'M'}$  might be much more complex in the theoretical approach. Helpful is the fact that there are a number of simplifications for the density matrix parameterization, making Eqn (8) attractive to phenomenology.

(1) The density matrix depends in expression (8) on the energy  $E_T$ . In fact, this matrix depends on  $E_{\text{tot}} - E_T$ , where  $E_{\text{tot}}$  is the total energy of the reaction in the center-of-mass system of the reaction. For direct reactions,  $E_{\text{tot}}$  is on the order of tens or hundreds of MeV, while the range of interest of the  $E_T$  variation is about a few MeV. Thus, the dependence of  $\rho_{JM}^{J'M'}$  on  $E_T$  can usually be ignored for practical purposes.

(2) The Treiman–Yang criterion [31, 32] should be obeyed for direct reactions described in the pole approximation. In a reference frame where the  $z$ -axis is parallel to the vector of the transferred momentum  $\mathbf{q}$ , this criterion implies a physically insignificant azimuthal angle. Such angles are  $\phi$  or  $\alpha$  for the final state of two and three bodies, respectively. As a result, the number of parameters in expression (8) is reduced to four or seven, correspondingly. From a formal point of view, the Treiman–Yang criterion requires the symmetry of the density matrix with respect to the change of sign of the magnetic quantum number projections:

$$\rho_{JM}^{J'M'} \equiv \rho_{J-M}^{J'-M'}.$$

A test for satisfaction of the Treiman–Yang criterion is always done in our experimental work. Its meeting is an encouraging signal for the applicability of a simplified analysis; however, it does not guarantee success, inasmuch as the satisfaction of the criterion is a necessary but not sufficient condition for the validity of the pole approximation.

(3) A strong alignment can reduce the number of free parameters in the density matrix. So, under the condition of zero projection of the magnetic quantum number being transferred in the reaction, the density matrix for the population of nuclear states with integer  $J$  will have so-called polar alignment in the system where  $z \parallel \mathbf{q}$ :

$$\rho_{JM}^{J'M'} \sim \delta_{M,0} \delta_{M',0}. \quad (10)$$

## 2.4 Correlations in three-body systems

To study three-body correlations, one needs to pass from single-particle radius vectors  $\mathbf{r}_i$  of three bodies to the Jacobian coordinates (Fig. 6):

$$\begin{aligned} \mathbf{X} &= \mathbf{r}_1 - \mathbf{r}_2, \\ \mathbf{Y} &= \frac{A_1 \mathbf{r}_1 + A_2 \mathbf{r}_2}{A_1 + A_2} - \mathbf{r}_3, \\ \mathbf{R} &= \frac{A_1 \mathbf{r}_1 + A_2 \mathbf{r}_2 + A_3 \mathbf{r}_3}{A_1 + A_2 + A_3}. \end{aligned} \quad (11)$$

Canonically conjugate to them are the Jacobian momenta

$$\begin{aligned} \mathbf{k}_x &= \frac{A_2 \mathbf{k}_1 - A_1 \mathbf{k}_2}{A_1 + A_2}, \\ \mathbf{k}_y &= \frac{A_3 (\mathbf{k}_1 + \mathbf{k}_2) - (A_1 + A_2) \mathbf{k}_3}{A_1 + A_2 + A_3}, \\ \mathbf{k}_R &= \mathbf{k}_1 + \mathbf{k}_2 + \mathbf{k}_3. \end{aligned} \quad (12)$$

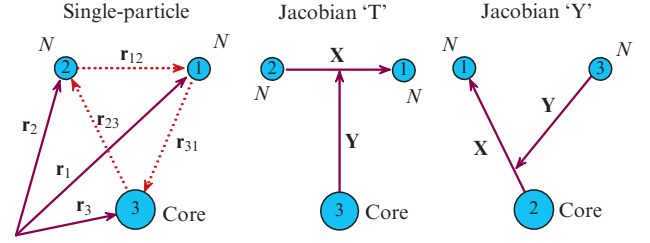


**Figure 6.** Single-particle, relative, and Jacobian coordinates for the three-body system. Only the two Jacobian systems, ‘T’ and ‘Y’, are not equivalent for a system consisting of a core and two identical nucleons.

There are three topologically different Jacobian systems, which can be obtained by cyclic permutation of the particles in formulas (11) and (12) in the general case of three different bodies. Only two systems are not equivalent and have their own names ‘T’ and ‘Y’ (see Fig. 6) for the frequently encountered three-particle systems consisting of a core and two identical valence nucleons.

The coordinate  $\mathbf{R}$  and momentum  $\mathbf{k}_R$  of the center-of-mass of the entire three-particle system are not involved in its dynamic description. Thus, the Jacobi vectors  $\mathbf{k}_x$  and  $\mathbf{k}_y$  are sufficient for a complete description of correlations in the three-particle system. This description becomes the five-parametric one at a fixed total decay energy  $E_T$ . Correlations of the three-particle decay of nuclear systems populated in direct reactions are illustrated in Fig. 7. It appears convenient to divide the correlations into two-dimensional, ‘internal’ or energy-angular ones, which depend on the three-body decay dynamics, and three-dimensional, ‘external’ ones related to the orientation of the three-particle system as a whole. The internal correlations are parameterized by a variable of energy distribution  $\varepsilon$  and the angle between the Jacobian momenta  $\theta_k$ :

$$\begin{aligned} E_T &= E_x + E_y = \frac{A_1 + A_2}{A_1 A_2} \frac{k_x^2}{2M} + \frac{A_1 + A_2 + A_3}{(A_1 + A_2) A_3} \frac{k_y^2}{2M}, \\ \varepsilon &= \frac{E_x}{E_T}, \quad \cos \theta_k = \frac{\mathbf{k}_x \mathbf{k}_y}{k_x k_y}, \end{aligned} \quad (13)$$

where  $M$  is the average mass of a nucleon in the system. The parameter  $\varepsilon$  shows the relative  $E_T$  distribution in the  $E_x$  and  $E_y$  Jacobian subsystems.

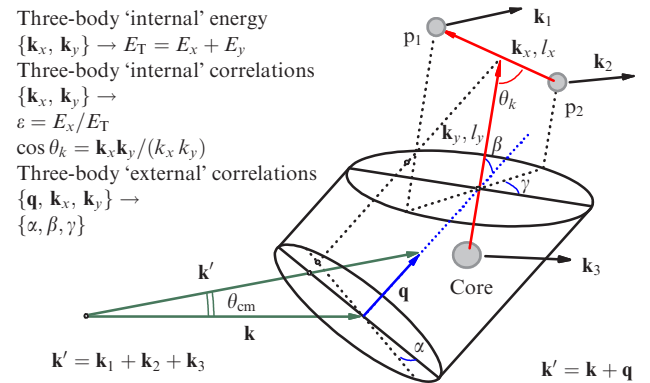


**Figure 7.** Correlations in the three-body decay of a nuclear system populated in a direct reaction.

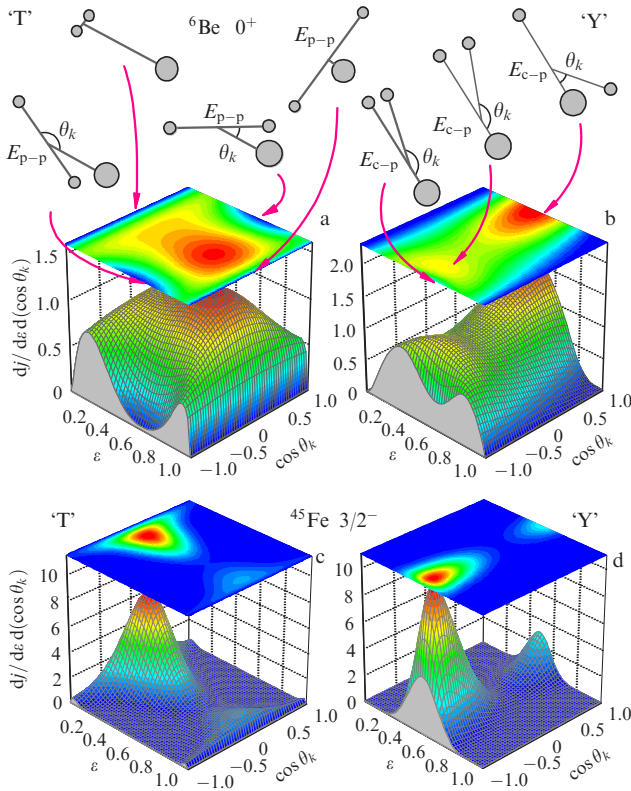


**Figure 8.** (Color online.) Energy-angular (or internal) correlations for the 2p-decays of the  ${}^6\text{Be}$  (a, b) and  ${}^{45}\text{Fe}$  (c, d) ground states calculated in the three-particle model. The correlations are presented in the Jacobian ‘T’ and ‘Y’ systems. A qualitative illustration for some typical regions in the kinematic plane  $\{\varepsilon, \cos \theta_k\}$  is given in the upper part of figures a and b.

Examples of internal correlations in the plane  $\{\varepsilon, \cos \theta_k\}$  for the 2p-decays of the  ${}^6\text{Be}$  and  ${}^{45}\text{Fe}$  ground states, calculated in the three-particle model, are given in Fig. 8. The correlation representations in the different Jacobian systems are physically completely equivalent. However, the involvement of both representations makes easier the visualization of the details associated with various aspects of the decay dynamics. Theoretically calculated correlation patterns are in good agreement with experiment [45–47], and, moreover, the achieved agreement is excellent in the case of light systems (see Section 3.5).

Three parameters required to describe external correlations are associated with the Euler angles  $\{\alpha, \beta, \gamma\}$ , which is a standard parameterization of the solid body orientation (see Fig. 7). According to the Treiman–Yang criterion [31, 32], parameter  $\alpha$  is not meaningful and distribution over this angle should be isotropic for direct pole reactions. The angle  $\gamma$  is involved in the correlation patterns in a rather complicated way. On the contrary, the distribution over the angle  $\beta$ , the angle between the direction of the particle emission 3 (in Fig. 6) and the direction of the transferred momentum  $\mathbf{q}$ , can be strongly pronounced in some cases, which is easy to interpret. The principal reasons for this feature are the same as in the two-particle case for ordinary two-body decays, as discussed in Section 2.3. This approach works particularly well in the case of interference between broad overlapping states, and in reactions leading to a strong alignment of the final states.

### 3. Dynamics of a few-body problem at the border of stability

In Section 2, we discussed the approach to the RIB reaction study at the ACCULINNA facility. In this section, we will touch upon a variety of theoretical results related to unusual phenomena observed near the drip line. We will deal with a specific subset of tasks which should be considered in terms of the few-body dynamics. Such phenomena as nucleon halos, proton decays, the soft dipole mode, and the Thomas–Ehrman shift undoubtedly emerge in the one-nucleon version (two-body problem) at the border of nuclear stability. However, we will examine in this section their more complicated version related to the collective motion of three or more bodies.

Not all of the problems discussed in Sections 3.1–3.8 are related to studies directly carried out at the ACCULINNA facility. Nevertheless, they give a more general view of problematic topics considered in modern RIB experiments and in research conducted in collaboration by our group. Without going into all the details of the problems themselves and their historical explanation, we focus on a few glowing examples with important qualitative features.

#### 3.1 Hyperspherical harmonics method for the three-body problem

The application of the three-body problem to  $A > 3$  nuclei is based on a cluster approach. It is assumed that the basic dynamics of the considered nuclear system  $A$  is described by the potential interaction of three inert clusters:  $A_1$ ,  $A_2$ , and  $A_3$ . In this case, the total wave function (WF) can be factorized into the internal WFs of clusters and the three-body WF of their relative motion:

$$\Psi_A = \Psi_{A_1} \Psi_{A_2} \Psi_{A_3} \Psi(\mathbf{X}, \mathbf{Y}).$$

Russian scientists have contributed significantly to the development of methods of the many-body theory. After a rigorous approach to solving the three-body quantum-mechanical problem was realized within the method of Faddeev equations, an alternative approach, based on the hyperspherical harmonic method (HHM), was suggested and intensively developed. A range of principal problems in the application of this method to nuclear physics tasks was resolved in the work by Yu A Simonov [Institute of Theoretical and Experimental Physics (ITEP)] [48, 49], Yu F Smirnov [Lomonosov Moscow State University (MSU)] [50], A I Baz’ [51], M V Zhukov [52], V D Efros (Kurchatov Institute of Atomic Energy) [53, 54], and their coworkers from the mid-1960s to the late 1980s (see monograph [55] and references cited therein).

Our approach to a few-body problem, historically originating from a scientific school at the Kurchatov Institute of Atomic Energy, is based on the HHM. A discussion of the technical features and a detailed bibliography are presented in reviews [4, 25, 56, 57].

At the basis of the HHM lies the fact that the WFs of a series of three-body problems may be effectively expanded into the hyperspherical basis. First of all, such is the case for situations where the system resides in the three-body ‘collectivized’ state, and the employment of basis functions, explicitly depending on single-particle degrees of freedom, does not lead to compact decompositions of the WF. In the HHM, the wave function can be written down

as

$$\begin{aligned}\Psi(\mathbf{X}, \mathbf{Y}) &= \Psi(\rho, \Omega_\rho) = \sum_{K\gamma} \frac{\chi_{K\gamma}(\rho)}{\rho^{5/2}} \mathcal{J}_{K\gamma}(\Omega_\rho), \\ x^2 &= \frac{A_1 A_2}{A_1 + A_2} X^2, \quad y^2 = \frac{(A_1 + A_2) A_3}{A_1 + A_2 + A_3} Y^2, \\ \rho^2 &= x^2 + y^2, \quad \theta_\rho = \arctan \frac{x}{y},\end{aligned}\quad (14)$$

where we transform Jacobian vectors  $\{\mathbf{X}, \mathbf{Y}\} = \{X, \Omega_x, Y, \Omega_y\}$  into a hyperradius and hyperangle:  $\{\rho, \theta_\rho, \Omega_x, \Omega_y\} = \{\rho, \Omega_\rho\}$ . The hyperradius  $\rho$  is symmetric with respect to the permutation of particles. This feature of the hyperradius as a collective variable is more pronounced in an alternative definition:

$$\rho^2 = \frac{A_1 A_2 A_3}{A_1 + A_2 + A_3} \left( \frac{r_{12}^2}{A_3} + \frac{r_{23}^2}{A_1} + \frac{r_{31}^2}{A_2} \right). \quad (15)$$

The  $\mathcal{J}_{K\gamma}^{JM_J}$  hyperharmonics with the definite total spin  $J$  and its projection  $M_J$ , namely

$$\mathcal{J}_{K\gamma}^{JM_J}(\Omega_\rho) = \psi_L^{l_x l_y}(\theta_\rho) \left[ [Y_{l_x}(\Omega_x) \otimes Y_{l_y}(\Omega_y)]_L \otimes X_S \right]_{JM_J},$$

form the complete set of orthonormalized functions on the ‘hypersphere’  $\Omega_\rho$ . The ‘multiindex’  $\gamma = \{L, S, l_x, l_y\}$  is a short notation of a set of quantum numbers necessary for the description of the three-body system, with the exception of the principal quantum number—hypermomentum  $K$ . The pure hyperangle function is expressed as the Jacobi polynomials  $\psi_L^{l_x l_y}$ .

In the three-cluster approximation, the total nuclear Hamiltonian is reduced to the three-body Hamiltonian

$$\hat{H}_3 = \hat{T}_3 + V_{12} + V_{23} + V_{31} + V_3(\rho),$$

where the pair interactions  $V_{ij}$  have to be obtained from experimental data on the binary subsystems or from corresponding systematics, and a collective three-cluster interaction  $V_3(\rho)$  is introduced as a phenomenological correction specified by many-body effects beyond the three-cluster approximation. The employment of  $V_3(\rho)$  is relevant for problems where a precise fit of the energy of state is needed (for example, for calculations of widths). If describing experimental data demands a significant contribution from  $V_3(\rho)$ , it indicates that the three-cluster approximation is poorly applicable in this case.

Different physical problems might require different formulations of Schrödinger equation (SE), namely

$$(\hat{H}_3 - E_T) \Psi_{E_T} = 0, \quad (16)$$

$$(\hat{H}_3 - E_T) \Psi_{E_T}^\pm = 0, \quad (17)$$

$$\left( \hat{H}_3 - E_T + \frac{i\Gamma}{2} \right) \Psi_{E_T}^\pm = 0, \quad (18)$$

$$(\hat{H}_3 - E_T) \Psi_{E_T}^\pm = \Phi_q. \quad (19)$$

The homogeneous SE (16) is applied to solving the bound-states problem. The asymptotic behavior of the partial WFs  $\chi_{K\gamma}(\rho)$  for  $\rho \rightarrow \infty$  is determined by the modified Bessel function  $K$ , exponentially decreasing in the limit of large radii:

$$\chi_{K\gamma}(\rho) \sim \sqrt{\frac{2\kappa\rho}{\pi}} K_{K+2}(\kappa\rho) \sim \exp(-\kappa\rho). \quad (20)$$

Hypermomentum  $\kappa = \sqrt{2M|E_T|}$  is a dynamic variable conjugate with the hyperradius. The ‘scaling’ mass  $M$  is taken as the average nucleon mass for the considered nuclear system.

The solution to the homogeneous SE (17) with WF  $\Psi_{E_T}^\pm$  in the  $S$ -matrix representation is a standard approach in the case of a continuum spectrum. For partial WFs, equation (17) at the asymptotics gives

$$\chi_{K\gamma}^{K'\gamma'}(\rho) \sim \delta_{K\gamma}^{K'\gamma'} \mathcal{H}_{K+3/2}^-(\kappa\rho) + S_{K\gamma}^{K'\gamma'} \mathcal{H}_{K'+3/2}^+(\kappa\rho), \quad (21)$$

where  $\mathcal{H}^\pm$  is the Riccati–Bessel functions with converging and diverging wave asymptotics:

$$\mathcal{H}^\pm(\kappa\rho) \sim \exp(\pm i\kappa\rho).$$

Solving the problem of radioactive decay, it was found appropriate to make use of the homogeneous SE with the complex energy (18). In this case, the solution is sought for in the form of the WF  $\Psi_{E_T}^\pm$  containing only the diverging waves;

$$\chi_{K\gamma}^+(\rho) \sim \mathcal{H}_{K+3/2}^+(\kappa\rho) \sim \exp(i\kappa\rho). \quad (22)$$

For small widths,  $\Gamma \ll E_T$ , equation (18) is effectively reduced to an inhomogeneous SE with the real energy [58].

Population of the three-body continuum spectrum in many direct reactions can also be described by an inhomogeneous SE with the real energy (19), where the influence of the reaction mechanism is fully contained in the ‘source’  $\Phi_q$  which is the function of a single parameter—the vector of the transferred momentum  $\mathbf{q}$ . As an illustration, let us write down this term for one of the simplest reaction models—the sudden removal approximation. In this model, the spectrum of a system with mass number  $A$  is populated after the sudden removal of  $A_r$  nucleons from the WF of the initial state,  $\Psi_{A+A_r}$ , and we obtain

$$\Phi_q = \int d^3r_r \exp(i\mathbf{q}\mathbf{r}_r) \langle \Psi_{A_1} \Psi_{A_2} \Psi_{A_3} | \Psi_{A+A_r} \rangle,$$

where  $\mathbf{r}_r$  is the radius vector of the removed cluster  $A_r$ , and the expression in angle brackets is an overlap integral of the initial state and the final cluster state WFs. Such a model qualitatively satisfies the conditions of the stripping reaction at high energies, when the removal time of a subsystem  $A_r$  is significantly shorter than the characteristic time of nucleon motion inside the nucleus  $A$ .

Boundary conditions (20)–(22) were formulated for three-body systems without the Coulomb interaction (for example, for a charged core and two neutrons). Investigation of the three-body Coulomb interaction in a continuum spectrum is a separate, well-known, albeit generally unsolved problem (see Section 3.6).

The three-body SE in the hyperspherical basis is reduced to a set of differential equations for the partial hyperradial functions  $\chi_{K\gamma}$ . As an example, for equation (19) we get

$$\begin{aligned}& \left\{ \frac{d^2}{d\rho^2} - \frac{\mathcal{L}(\mathcal{L}+1)}{\rho^2} + 2M[E - V_{K\gamma, K\gamma}(\rho)] \right\} \chi_{K\gamma}^+(\rho) \\ &= 2M \sum_{K'\gamma' \neq K\gamma} V_{K\gamma, K'\gamma'}(\rho) \chi_{K'\gamma'}^+(\rho) - 2M \Phi_{\mathbf{q}, K\gamma}(\rho).\end{aligned}\quad (23)$$

These equations can be treated as those describing the motion of one effective particle with mass  $M$  in a strongly deformed



field. ‘Three-body potentials’ (matrix elements of the pair potentials)  $V_{K\gamma, K'\gamma'}(\rho)$  and partial components  $\Phi_{\mathbf{q}, K\gamma}$  of sources are defined as

$$V_{K\gamma, K'\gamma'}(\rho) = \int d\Omega_\rho \mathcal{J}_{K'\gamma'}^{JM_{J'}}(\Omega_\rho) \sum_{i < j} V_{ij}(\mathbf{r}_{ij}) \mathcal{J}_{K\gamma}^{JM_J}(\Omega_\rho),$$

$$\Phi_{\mathbf{q}, K\gamma}(\rho) = \int d\Omega_\rho \mathcal{J}_{K'\gamma'}^{JM_{J'}}(\Omega_\rho) \Phi_{\mathbf{q}}(\rho, \Omega_\rho).$$

Details on the hyperspherical harmonic method in application to different problems in the field of RIB investigations can be found in Refs [59–63].

### 3.2 Borromean nuclei

The most familiar ‘scientific brand’ related to RIB physics is the nuclear halo. As mentioned in Section 1.1, the basic concept of the one-nucleon halo is very simple. As the value of a nucleon separation energy comes close to zero and due to tunneling to the classically forbidden region, the average radius of a nucleon WF will come close to quite a large value; in particular, for the s-wave it tends to infinity since

$$\Psi(\mathbf{r}) = \Psi(r, \Omega) = \sum_{lm} \frac{\chi_l(r)}{r} Y_{lm}(\Omega), \quad (24)$$

$$\chi_{l=0}(r) \stackrel{r \rightarrow \infty}{\sim} \exp(-kr), \quad k = \sqrt{-2ME_T}.$$

Eventually, this leads to an increase in the nuclear root-mean-square (rms) radius, abnormally large reaction cross sections, narrow momentum distributions of the removal reaction products, and other unexpected effects.

Ironically, the history of the question began with the discovery of a halo with a more complicated origin, rather than the one-nucleon halo. In 1985, I Tanihata et al. [64] measured so-called interaction cross sections for lithium isotopes. For  $^9\text{Li}$ , the matter rms radius deduced from the measured cross sections,  $r_{\text{mat}} = 2.43$  fm, is in perfect agreement with standard systematics (1). At the same time, the  $^{11}\text{Li}$  rms radius, 3.27 fm, significantly deviates from the one obtained with the systematics (Fig. 9). In the planetary model, where  $^{11}\text{Li}$  is composed of  $^9\text{Li} + n + n$ , the rms radius of the particle’s valence orbitals is easy to calculate, giving the value of 5.7 fm. If one relies on the same systematics (1) in the opposite direction, one can estimate that such an average size of the nucleon orbitals is inherent for nuclei with the atomic number  $A \approx 110$ , which is an order of magnitude heavier than  $^{11}\text{Li}$ .

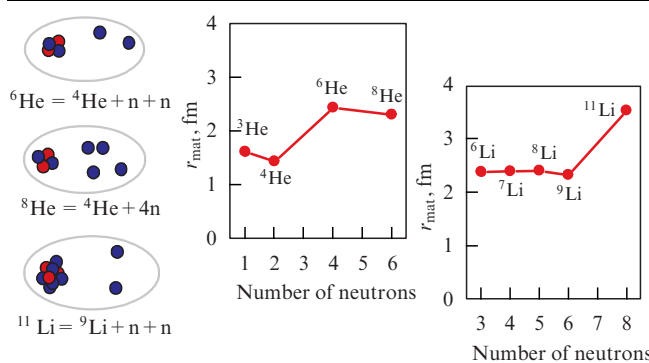


**Figure 9.** Clusterization and formation of halo in  $^6\text{He}$ ,  $^8\text{He}$ , and  $^{11}\text{Li}$ . Drastic increase in the matter root-mean-square radii of nuclei upon the transition from ‘ordinary’ nuclei to those with a two-nucleon halo.

An explanation of this phenomenon was given at the end of the 1980s by M V Zhukov and his colleagues (see review [56]). The problem lies in the fact that the nuclear halo in  $^{11}\text{Li}$  cannot be explained in terms of increasing the radius of the one-nucleon orbitals, as in Eqn (24), because the  $^{10}\text{Li}$  nuclear subsystem is unstable and cannot be associated with any negative one-nucleon energy  $E_T$ . A qualitative answer to this question was given within few-body physics in the framework of so-called *Borromean systems*.

In mathematics, Borromean rings provide an example of a ‘topological link’: the whole system is nonseparable, but there is no link between any two of the rings, i.e., rupture of any ring results in a complete disintegration of the system. The term ‘Borromean rings’ comes from the name of the Italian aristocratic family Borromeo, on whose coat of arms three connected rings are drawn. The image of the Borromean rings has been widely used in Italian heraldry (Fig. 10a). It symbolizes strength in unity.

The term ‘Borromean nuclei’ has been used in nuclear physics for three-body systems featuring a similar coupling property: the three-body system is bound, while all its two-body subsystems are unbound and the removal of one fragment leads to the decay of the rest. The energy scheme reflecting the emergence conditions for Borromean nuclei is depicted in Fig. 10b. This system is stable with respect to the two-nucleon emission (the two-nucleon separation energy is positive,  $S_{2N} > 0$ ), whereas the subsystem  $A - 1$  is unstable with respect to the one-nucleon emission (its ground state is resonant with the energy  $E_T$  above the threshold).

In nuclear physics, these energy conditions originate due to the pairing interactions and, hence, are often met at the border of stability. Thus, at the neutron drip line nearly every second nucleus is Borromean (see Fig. 1). From the theoretical viewpoint, realization of the energy conditions shown in Fig. 10b results in the development of collective three-body dynamics in the system, which is transparently illustrated in the framework of the hyperspherical harmonic method. The Borromean system WFs are effectively expanded in the hyperspherical basis and, which is noticeable, also have an exponentially decreasing asymptotics in the hyperradius space:

$$\Psi(\mathbf{X}, \mathbf{Y}) = \Psi(\rho, \Omega_\rho) = \sum_{K\gamma} \frac{\chi_{K\gamma}(\rho)}{\rho^{5/2}} \mathcal{J}_{K\gamma}(\Omega_\rho), \quad (25)$$

$$\chi(\rho) \stackrel{\rho \rightarrow \infty}{\sim} \exp(-\kappa\rho), \quad \kappa = \sqrt{-2ME_T}.$$

The only difference is that this asymptotics depends on the collective radius (hyperradius)  $\rho$  [see Eqn (15)] instead of the one-nucleon degrees of freedom, as in the two-particle case (24). Let us also mention another power dependence on the radial variable, namely, the power index 5/2 of the hyperradius, instead of 1.

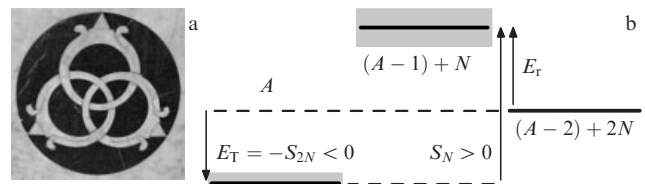


**Figure 10.** (a) Borromean rings in an emblem associated with the name of Lorenzo de Medici in a Florence chapel. (b) Energy diagram specifying conditions for the emergence of the Borromean nucleus.

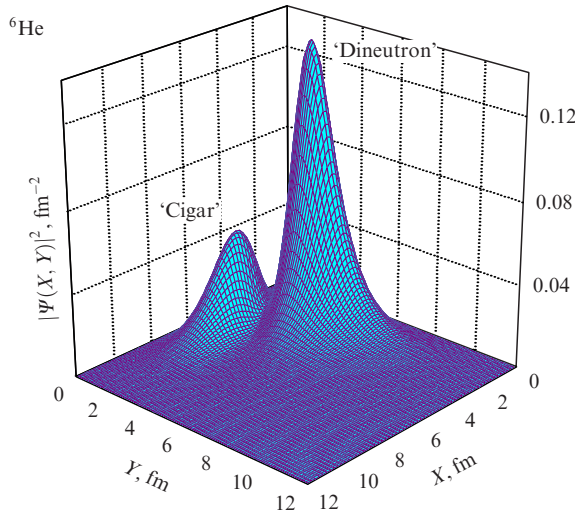


**Figure 11.** Correlation density (wave function squared) of  ${}^6\text{He}$  in the Jacobian coordinates in the ‘T’-system.

The density of the ground state WF of the  ${}^6\text{He}$  nucleus calculated in the three-body ( $\alpha$ -n-n) model is depicted in Fig. 11. Notable is the presence of two dominating configurations: one dineutron (small distance  $X$  between two neutrons), and the other cigar-shaped (small values of  $Y$  compared to  $X$  mean that the  $\alpha$ -core is placed approximately between two neutrons). The existence of such structures is experimentally confirmed (see Section 5.1) and has a transparent qualitative theoretical explanation (so-called Pauli focusing [65, 66]).

The study of the nuclear halo at the neutron drip line has a great potential. Today, the neutron drip line is reached and partly studied up to oxygen isotopes, but beyond that resides *terra incognita*. Forming a halo structure is rather complicated in the vicinity of the proton drip line, as the Coulomb barrier inhibits effective penetration of the proton WF into the classically forbidden region. However, it is recognized that the formation of a one-proton halo in the  ${}^8\text{B}$  nucleus and the two-proton halo in the  ${}^{17}\text{Ne}$  nucleus is due to the rather low binding energies,  $E_b = 136$  keV and  $E_b = 944$  keV, respectively. The formation of the proton halo in heavier systems is hardly expected, although another possible candidate for the two-proton halo is  ${}^{31}\text{Ar}$ . For now, experiment shows the binding energy of this nucleus to be close to zero. With these Coulomb barriers, distinctions in the manifestation of the Borromean halo and two-proton radioactivity (see Section 3.4) are blurred.

### 3.3 Soft dipole mode

A classic example of the collective dynamics in nuclei is given by the phenomenon of giant dipole resonance (GDR). This is not a separate resonance, but rather an envelope curve for a set of resonances possessing large dipole matrix elements with the nucleus ground state. This means that there is an intensive GDR population in the electromagnetic excitation reactions where the dipole component usually dominates. GDR is localized at the energies of  $\sim 25$  MeV in light nuclei, and at the energies of  $\sim 15$  MeV in heavy ones, and the properties of the GDR are closely related to properties of nuclear matter (first of all, with nuclear compressibility and charge polarizability), which determines the continuing interest in this problem. As a collective mode of nuclear excitation, GDR is qualitatively connected to a collective oscillation of all

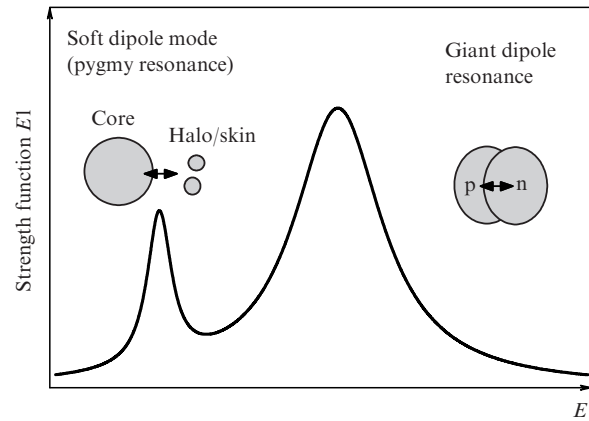


**Figure 12.** Qualitative illustration of the GDR and SDM origins.

protons against all neutrons in a nucleus under the action of momentum of a dipole electromagnetic field.

As was mentioned, in contrast to ‘ordinary’ nuclei, halo nuclei have two scales: the first one is about the nuclear length, and the second much larger one is related to the motion of halo nucleons. Obviously, this should lead to an additional low-energy component (soft dipole mode, or SDM) in the dipole strength function (Fig. 12). To evaluate the scale of this phenomenon, one could make a simple assessment of the dipole matrix element  $M_{E1}(E)$  using a single-particle s-wave WF  $\phi_{l=0}$  in a simple analytical form (Hülthén ansatz) and a  $p$ -wave component of the plain wave (cylindrical Bessel function  $j_1$ ):

$$\begin{aligned}\phi_{l=0}(r) &= N[\exp(-k_1 r) - \exp(-k_2 r)], \quad k_1 = \sqrt{2ME_b}, \\ M_{E1}(E) &= \int_0^\infty dr (pr) j_{l=1}(pr) r \phi_{l=0}(r), \quad p = \sqrt{2ME}, \\ \frac{dB_{E1}}{dE} &\sim \frac{|M_{E1}(E)|^2}{\sqrt{E}}.\end{aligned}\quad (26)$$

The estimated dipole strength functions  $dB_{E1}/dE$  are plotted in Fig. 13. Parameter  $k_2$  is arbitrarily fixed here as  $k_2 = 1 \text{ fm}^{-1}$ . It can be seen that for the appreciable nucleon binding energies of (5–10 MeV), typical of many stable nuclei, the single-nucleon dipole strength is distributed in a wide range of excitation energies (up to 20–30 MeV). For a weakly bound nucleus,  $E_b \sim 1$  MeV, this strength is concentrated at energies of  $E \sim 0.5$ –1 MeV. For an extremely weakly bound nucleus,  $E_b \sim 0.1$  MeV, i.e., for a system with an extremely extended halo, the dipole strength is totally localized near the threshold  $E < 100$  keV. These simple ideas explaining the possible existence of SDMs were first suggested by K Ikeda [67] in 1988. Since that time, various kinds of SDMs have been actively studied (see, for example, review [68], and also Sections 5.6, 5.7).

There are two main conclusions here.

(1) The presence of a nucleon halo will reveal itself with high probability in the SDM as a specific form of the nuclear excitation mechanism related to wide spatially distributed WFs.

(2) Observation of an intensive low-energy peak does not necessarily indicate the presence of a resonance state in the system. In striking contrast to the concept of resonance as a manifestation of the *final state* dynamics alone, the concept of the *mode of excitation* is introduced as a phenomenon related

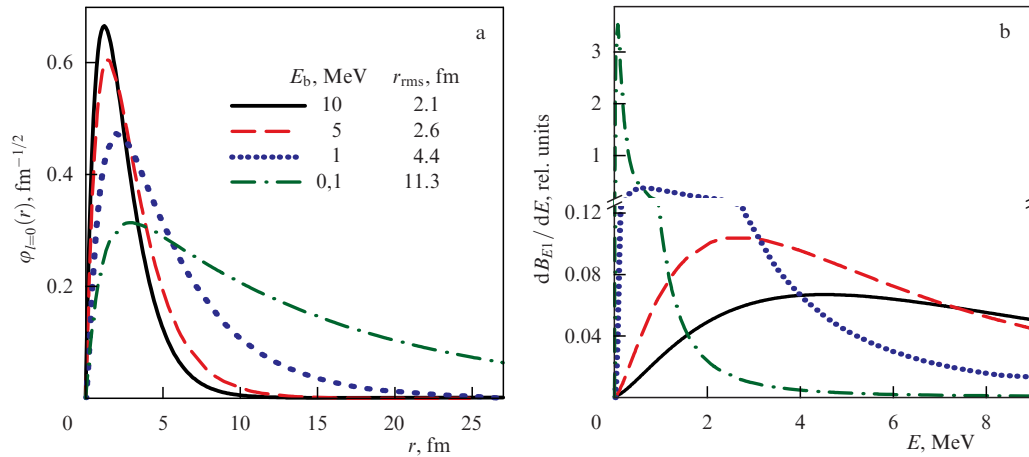


**Figure 13.** (a) Hülthén type one-nucleon WF for different binding energies;  $E_b$  is the binding energy, and  $r_{rms}$  is the root-mean-square radius for a certain WF. (b) Dipole strength functions estimated for transition from the state with the wave functions shown in figure (a) to the plain-wave continuum spectrum.

to the *initial state structure* and *excitation mechanism*. Questions concerning the excitation modes and their relation to the halo phenomenon are considered in review [57].

Interest in SDM is largely determined by the fact that, at the decay of halo nuclei, matrix elements of electromagnetic dipole transitions, responsible for SDM, determine the probabilities of the inverse processes as well, i.e., radiative capture processes. Exactly these processes of the nonresonant radiative capture with the parity alteration appear to be dominant for many reactions of key importance in astrophysics. For example, the classical reaction  ${}^7\text{Be} + p \rightarrow {}^8\text{B} + \gamma$  is among them: it is important for the solar neutrino problem. Thus, by studying the photodissociation reactions of halo nuclei (a realistic approach to this is, certainly, the dissociation induced by virtual photons in Coulomb excitation reactions), it is possible to recalculate the obtained results deducing the cross section values of astrophysical radiative captures for nuclei participating in the r- and rp-processes (see, for example, Refs [69–74]).

Notice that SDMs for a three-body system have special features compared to those in the two-body case (Fig. 14). In the two-body case, the basic dynamics of the process can be explained in terms of simple estimates (26) using a satisfactory approximation with a plane wave instead of a nonresonant continuum WF. In the three-body case, the dipole operator is capable of promoting the one-nucleon transition to a nonresonant state. As a result, the final state's dependence of the three-body SDM will be characterized by a nontrivial combination of resonant and nonresonant dynamics. In this

case, quite simple approaches are also available [71], although, in general, the situation with SDMs in three-body systems remains poorly studied, and there is still no agreement on this. In particular, the unexplainable discrepancy in the experimental data is noticeable for repeatedly studied SDM in  ${}^{11}\text{Li}$  (see paper [75] and references cited therein). The results of SDM studies at the ACCULINNA facility are presented in Sections 5.6, 5.7.

### 3.4 Two-proton radioactivity

Two-proton radioactivity—the ‘freshest’ among all known types of radioactive decays—was found in 2002 in almost simultaneous experiments at GSI [22] and GANIL [23] during studies of the decay of the  ${}^{45}\text{Fe}$  nucleus. Some intrigue had preceded this discovery for quite a number of decades.

The possibility of two-proton radioactivity was predicted by Soviet theorists at the beginning of 1960s. A paper by V I Goldansky [76] is usually referred to here (where the prospects for the search for proton radioactivity have also been discussed). However, the basic statement about the possibility of two-proton radioactivity can be found in earlier work by Ya B Zel’dovich [77]. The main idea is the following: the ordinary two-particle decay (one-proton emission) becomes prohibited under certain energy conditions, and the system can only decay into a three-particle channel with simultaneous emission of two protons (Fig. 15). Similar to the Borromean halo, this phenomenon is related to the pairing interaction: it is easy to recognize that the energy level scheme in Fig. 15a can be obtained by shifting upwards all the levels from Fig. 10 with respect to the threshold, which corresponds to a decrease in binding energy, for example, due to the increased additional Coulomb interaction. Indeed, for the lightest nuclei, the two-neutron halo near the neutron drip line can correspond to the two-proton radioactive nucleus behind the proton border. These pairs of isobaric partners are as follows:  ${}^6\text{He} = \alpha + n + n$  and  ${}^6\text{Be} = \alpha + p + p$  or  ${}^{12}\text{Be} = {}^{10}\text{Be} + n + n$  and  ${}^{12}\text{O} = {}^{10}\text{C} + p + p$ .

In order to stress a qualitative difference between this process and the intuitively obvious *sequential* decay mechanism of proton emission, Goldansky introduced the term *true two-proton decay*. It is clear that the possibility of implementing such dynamics is not exhausted by two-proton emission,

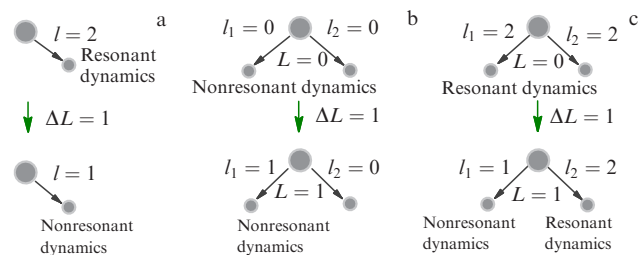


**Figure 14.** Qualitative distinction between SDM (a) in the two-body dynamics (one-nucleon halo nuclei), and (b, c) that in the three-body dynamics (two-nucleon halo nuclei) by the example of the s–d-shell.

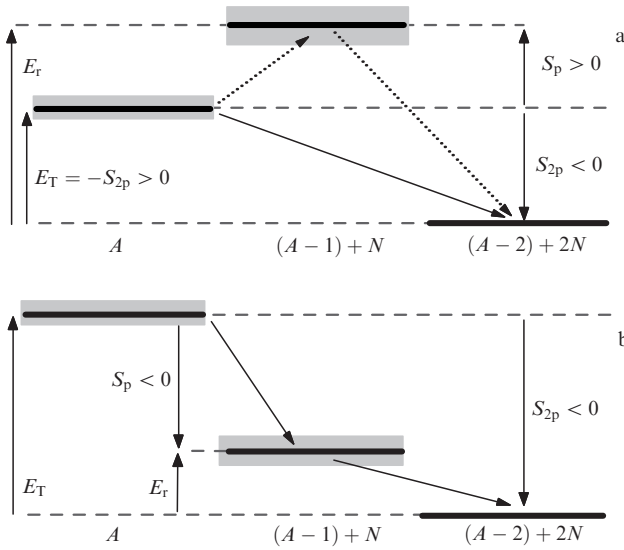


**Figure 15.** (a) Energy level diagram determining conditions for the occurrence of true two-proton decay (two-proton radioactivity). (b) Similar schematic for sequential two-proton decay with the dynamic reducible to the two-particle one (to a consequence of ordinary proton decays).

and the true three-particle decay should be considered for a wider class of systems. Figure 16 qualitatively explains the consequence of events in true two-proton decay. At the first stage I, both nucleons occupy a common orbital with diffuse energy, where the mean energy of each nucleon harbors half of the decay energy,  $E_T/2$ . If one nucleon starts to tunnel and passes to the underbarrier region II, the orbital, where the nucleons initially were, no longer exists. The very existence of the orbital is related to the pairing phenomenon which disappears when the nucleons become separated in space. Now, the closest one-nucleon orbital III is taken up with the energy  $E_r > E_T$ . The ‘residual’ nucleon IV appears to be deep under the barrier in the nonresonant configuration and, hence, should leave it (V) within an exponentially short time.

Goldansky suggested estimating the two-proton decay probability in the independent particle model. The noninteracting protons pass through the Coulomb barrier and share the total energy of the decay:

$$\frac{d\Gamma_3(E_T)}{d\varepsilon} \sim \exp \left[ -\frac{2\pi(Z-2)\alpha\sqrt{M}}{\sqrt{E_T}} \left( \frac{1}{\sqrt{\varepsilon}} + \frac{1}{\sqrt{1-\varepsilon}} \right) \right],$$

$$\Gamma_3(E_T) = \int_0^1 d\varepsilon \frac{d\Gamma_3(E_T)}{d\varepsilon}. \quad (27)$$

Here, parameter  $\varepsilon$  stands for the energy distribution between the protons:  $E(p_1) = \varepsilon E_T$  and  $E(p_2) = (1-\varepsilon) E_T$ . For comparison, we give a standard expression for estimating the

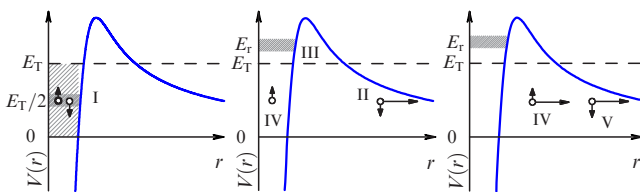


**Figure 16.** Origin of the true three-body decay phenomenon (two-proton radioactivity).

width  $\Gamma_2$  of a common one-proton decay with the decay energy  $E_r$ :

$$\Gamma_2(E_r) \sim \exp \left[ -\frac{\pi(Z-1)\alpha\sqrt{M}}{\sqrt{E_r}} \right].$$

In order to make a realistic width assessment, the above exponential expressions should be multiplied by a dimensional scaling factor on the order of 1 MeV. It can be clearly seen from Eqn (27) that the true two-proton decay width approximately corresponds to the scheme of the decay with the emission of a particle characterized by the doubled charge (diproton) and halved energy of the decay  $E_T/2$ . Thus, the energy systematic of the three-particle decay width is significantly different from that for the two-particle decay.

After the initial period of active studies [78, 79], interest in the two-proton radioactivity faded: no satisfactory theoretical results had been produced, and the experimental search was delayed for decades. Proton radioactivity was discovered in 1982 [21]; however, all attempts to reveal the two-proton radioactivity failed. Theoretical discussions of this problem were limited to using the trivial ‘diproton’ model [80]. This situation is somewhat true today [81, 82].

Significant progress in the theoretical treatment of 2p-radioactivity was reached only in 2000, when in Ref. [58] prospective two-proton radioactive nuclei  $^{19}\text{Mg}$  and  $^{45}\text{Fe}$  were studied in the three-body (core + p + p) model. The progress on the theory has become an important factor in the discovery of 2p-radioactivity. Experiment [23] was performed one year earlier than that reported in paper [22]. However, the authors of Ref. [23] were expecting the lifetime of  $^{45}\text{Fe}$  to be about *microseconds*, as predicted in the diproton model [80]. Predictions [58] in the three-body model refer to the region of *milliseconds*. This was found experimentally in Ref. [22]. Study [23] was published after the reexamination of its data with regard for the results obtained in paper [22]. Notice that confirmation of the data gathered in Ref. [22] in Ref. [23] was not superfluous: both of the studies were based on extremely low statistics (few events).

During the last decade, huge progress has been achieved in the field of 2p-radioactivity studies. New cases of 2p-radioactivity involving  $^{19}\text{Mg}$  [9],  $^{48}\text{Ni}$  [83], and  $^{54}\text{Zn}$  [84] nuclei have been examined. Proton correlations from the 2p-decay were investigated for  $^{19}\text{Mg}$  [85],  $^{45}\text{Fe}$  [45], and  $^{54}\text{Zn}$  [86]. Moreover, correlation data were obtained in Ref. [45] for  $^{45}\text{Fe}$  at a confidence level good enough to reach a conclusion about the configuration mixture in  $^{45}\text{Fe}$  and the peculiarities of the three-body Coulomb interaction. Theoretical aspects of 2p-radioactivity have been intensively studied by our team in the framework of the three-body model [61, 87–91]. The main results of these studies were the development of the lifetime systematic for 2p-radioactive nuclei and the determination of prospective candidates for the experimental search. For the first time, 2p-correlations have been theoretically calculated. The quality of these calculations was gradually improving, and the consequent development of the experiment confirmed the predictions. A set of fundamental problems has been solved, such as the use of approximate semianalytical approaches [90, 91], making precise calculations of correlations with regard for the long-range character of the three-body Coulomb interaction [92, 93], and considering many-body effects of the nuclear structure in three-particle decays [94]. Both experimental and theoretical results obtained in this field are described in detail in recent reviews [4, 25].



In theoretical studies of 2p-radioactivity, an important technical issue is the Coulomb interaction in the three-body system. The three-body Coulomb problem in the continuum spectrum is a known problem of theoretical and mathematical physics. It is still not generally been solved. However, it may be asserted that a part of the problem related to nuclear systems with three similarly charged particles has been solved from the practical viewpoint (see Section 3.6).

In discussing two-proton radioactivity, we mean the two-proton decays of the ground states. However, the study of the true two-proton decay of excited states is of special interest in nuclear astrophysics applications [4, 71, 95]. Such a decay can be considered the time-reversal process to the two-proton radiative capture which itself can be an important process in a number of cases, in particular, when it is necessary to bypass a waiting point of the rp-processes in nucleosynthesis [96]. In work on the thermonuclear synthesis in astrophysics [97, 98], quasiclassical approaches are traditionally applied for describing the two-proton capture. However, these approaches may fail when the capture process is the true three-body one. In this case, a detailed analysis within the many-body theory is needed [91, 95]. The experimental search for the two-proton decay of the first excited state in  $^{17}\text{Ne}$  for applications in nuclear astrophysics is presented in Section 5.9.

The two-proton emission process was studied in detail for democratic decays representing the whole class of phenomena congenerous to two-proton radioactivity. Section 3.5 and partly Sections 3.6, 3.7 are devoted to these investigations.

### 3.5 Democratic decays

In contrast to the concept of two-proton radioactivity, which existed for decades in a pure theoretical form before its experimental confirmation came, the concept of *democratic decay* appeared as the result of experimental investigations. While studying the 2p-correlations in  $^6\text{Be}$  decay, experimentalists found that the extracted energy correlations cannot be explained by a simple combination of the binary amplitudes [99, 100]. Since the particles appeared to be homogeneously distributed in the kinematic space, this decay was called ‘democratic decay’ in the sense of the ‘equality’ among different regions of the kinematic space [100]. This feature is visually illustrated in Fig. 8, where theoretical three-body correlation patterns for the  $^6\text{Be}$  democratic decay are compared to those for the two-proton radioactivity in  $^{45}\text{Fe}$ . In the case of  $^6\text{Be}$ , the  $\{e, \cos\theta_k\}$  plane is more or less uniformly filled, while considerable areas of kinematic space are ‘swept out’ in the case of  $^{45}\text{Fe}$  by the Coulomb interaction and the so-called Pauli focusing [65, 66].

Energy schematics for the democratic decay are presented in Fig. 17. They practically coincide with the schematics in Fig. 15, except that the ground state widths of the  $A - 1$  subsystem are a large and significant ‘part’ of the two-particle resonance always resides in the ‘energy window’ of the 2p-decay. Formally, according to the proton separation energy  $S_p > 0$ , the energy scheme in Fig. 17a corresponds to a true two-proton decay, whereas that in Fig. 17b, with  $S_p < 0$ , formally allows the possibility of a sequential decay. However, it appears that both cases are effectively described in terms of few-body dynamics as the true two-proton process. From a theoretical viewpoint, there are also rather significant qualitative distinctions between the democratic decay and the 2p-radioactive decay (see discussion in review [25]). In particular, there are qualitative distinctions in the energy

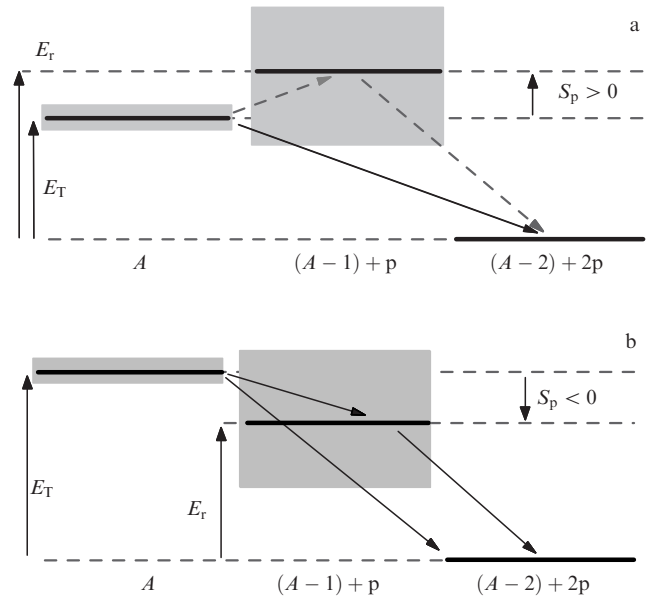


**Figure 17.** Energy schematics illustrating conditions for democratic nuclear decays.

systematics of the lifetimes and behavior of correlations in regimes intermediate between sequential and true two-proton decays.

The term *democratic decay* has been accepted for a rather wide class of decays, and now has become the standard. The 2p-decays of the ground states of the lightest proton-rich nuclei, such as  $^6\text{Be}$ ,  $^{12}\text{O}$ ,  $^{16}\text{Ne}$ , and, probably, yet unknown 2p-decays of nuclei more distanced from the drip line, such as  $^{11}\text{O}$  and  $^{15}\text{Ne}$ , are referred to as democratic decays. Besides this, the already-studied two-neutron decays of the ground states of systems beyond the neutron drip line ( $^5\text{H}$ ,  $^{10}\text{He}$ , and  $^{13}\text{Li}$ ) are also among the democratic decays.

Since the democratic 2p-emitters belong to light systems, they are much more available for study, than those experiencing radioactive 2p-decays. In the last five years, significant progress has been achieved. The nuclei  $^6\text{Be}$  [46, 47, 63, 101],  $^{12}\text{O}$  [102], and  $^{16}\text{Ne}$  [93, 103, 104] have been studied in precise experiments with the statistics sometimes exceeding  $10^6$  events per resonance. From the theoretical viewpoint, the high quality of the data allowed the careful test of calculating methods, and demonstrative clarification of dynamics in a set of hard-to-explain phenomena. For example, as shown in Refs [47, 104], even for a substantial increase in the decay energy  $E_T$  of nuclei exhibiting democratic decays (democratic 2p-emitters), the decay mechanism does not change to the expected pure sequential one, and the complicated three-body dynamics of emitted particles remains the same. The quality of modern experimental data and quality of the data description in the three-body model are illustrated in Fig. 18. The experiment on the  $^6\text{Be}$  decay (although mainly aimed at the study of SDM) is considered in Section 5.7

The following feature of the democratic decay emitters should be noted. Even the ground states of these emitters are quite wide, and the neutron decay widths are, certainly, wider than the proton ones. Thus, the widths are  $\Gamma \sim 100$  keV for  $^6\text{Be}$  and  $^{12}\text{O}$ , and they are  $\Gamma \sim 1$  MeV for  $^5\text{H}$  and  $^{10}\text{H}$ . It is easy to show that exactly at width values on the order of 1 MeV, the boundary lies between the nuclear structure and the continuum spectrum dynamics. Let us estimate the



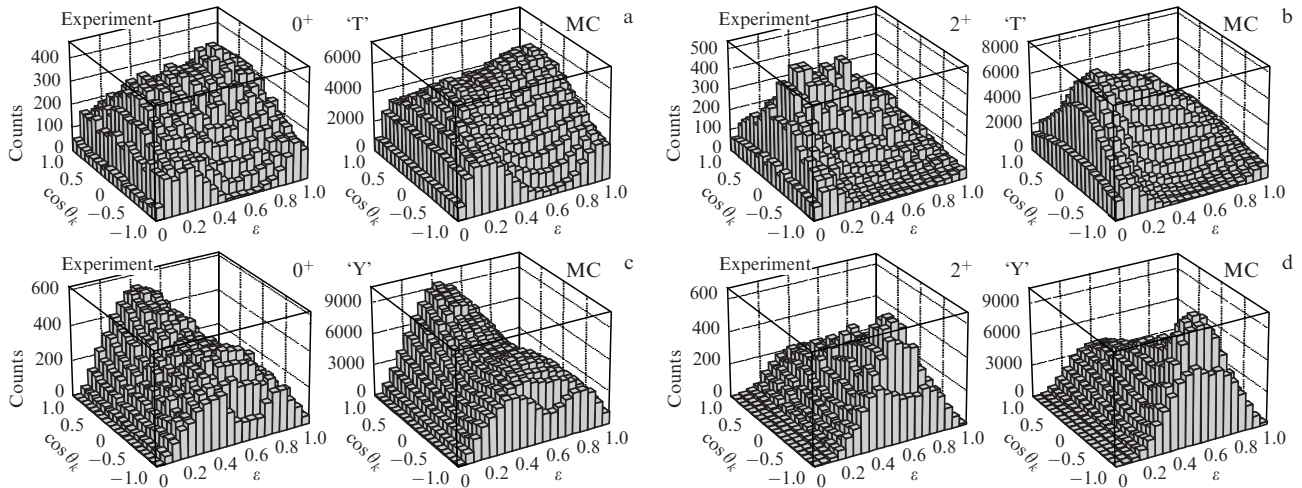


**Figure 18.** Total (energy-angle) ‘internal’ three-body correlations for democratic 2p-decays of the ground state  $0^+$  (a, c) and the first excited state  $2^+$  (b, d) in  ${}^6\text{Be}$  in the ‘T’ and ‘Y’ Jacobian systems. The experimental data from Ref. [47] (in the left part of figures a–d) and the results of three-body calculations after MC simulations (in the right part of figures a–d).

classical time of flight of an arbitrary nucleon with mass  $M$  through the nucleus:

$$t = r_{\text{nuc}} \sqrt{\frac{M}{2T_{\text{nuc}}}},$$

where  $T_{\text{nuc}}$  is the mean kinetic energy inside the nucleus. For  $T_{\text{nuc}} \sim 50\text{--}100$  MeV and  $r_{\text{nuc}} \sim 3\text{--}6$  fm, we find that, during the time corresponding to a width of 1–2 MeV, the nucleon experiences only 3–10 reflections from the potential barrier. This number of reflections is insufficient for establishing an internal structure and, thus, for erasing the formation memory for the system. In this case, the observed spectrum becomes dependent on the population conditions and reaction mechanisms. The practical importance of the accurate analysis of this dependence on the reaction mechanism was demonstrated by the examples of  ${}^3\text{H}$  [105–107],  ${}^{10}\text{H}$  [108],  ${}^6\text{Be}$  [109], and  ${}^{26}\text{O}$  [110]. The experimental results on  ${}^{10}\text{He}$  are also discussed in Section 5.5.

### 3.6 Coulomb three-body problem for 2p-decays

The Coulomb three-body problem for a continuum spectrum is one of the oldest and generally unresolved problems of theoretical and mathematical physics. Formally, this is expressed as the fact that a rigorous analytical solution for boundary conditions at infinity is not found in the coordinate representation, and in the momentum representation the three-body kernel of Faddeev’s equations contains divergences.

For example, for equations in the hyperspherical harmonics method, this is reflected in the fact that the three-body potentials entering into equations (23) have the Coulomb asymptotics for  $\rho \rightarrow \infty$  in the hyperradius space:

$$V_{K\gamma, K'\gamma'}(\rho) \sim \frac{\kappa \eta_{K\gamma, K'\gamma'}}{M\rho}. \quad (28)$$

It should be noted that unlike to the two-body case, the Sommerfeld parameter is a matrix, and this matrix is essentially non-diagonal. So, the different channels  $\{K, \gamma\}$  for the three-body Coulomb problem cannot be uncoupled, and it is impossible to define their analytically rigorous boundary conditions (for comparison, see equations (20)–

(22) in the absence of the Coulomb interaction). In the discrete spectrum (with an exponentially decreasing asymptotics), this difficulty can be overcome by increasing the radius of the numerical solution of the equations. In the continuum spectrum, the boundary condition problem turns out to be fundamental.

In recent years, considerable practical achievements in solving the mentioned problem have been associated with combining analytical and numerical methods [111–116]. In our work [25, 58, 61] we took an approach started from the solution of the pure ‘decay’ problem (22) with an approximate boundary condition of the Coulomb three-body problem. The approximation used is based on a diagonalization of the Coulomb potentials (28) on a hypersphere with a large radius (for example,  $\rho \sim 300\text{--}3000$  fm), which follows the procedure earlier suggested by S P Mercuriev but not realized.

The application of this procedure is equivalent to the cutoff of the Coulomb interaction at the corresponding radius. This gives quite realistic first-order results. However, the substantial improvements in the experimental data quality over the last years required the refinement of calculating methods. A satisfying practical solution was found combining classical and quantum-mechanical approaches [92]. Equations (23) are solved with respect to  $\rho$  at ranges up to maximal practically achievable radius  $\rho_{\text{cut}}$  in the numerical calculation scheme. On the surface of a hypersphere of large radius  $\rho_{\text{cut}}$ , the probability density turns into a large number of ‘MC events’ (see the discussion of the application of the Monte Carlo method in Section 2.3 for a comparison of theoretical and experimental results). For an individual event, the classical Coulomb problem of flying apart three bodies is solved with respect to radii  $\rho_{\text{max}} \gg \rho_{\text{cut}}$ , which are enough to stabilize the fragment momenta with an arbitrary specified accuracy. The momentum distributions are retrieved according to the results of the procedure for a large number of events.

If we take a look at the results of such a ‘classical extrapolation’ for the particularly interesting case of radioactive  ${}^{45}\text{Fe}$  decay (Fig. 19), we will easily see distinctions from the results of a pure quantum-mechanical calculation. A quantitative comparison with the experimental results is

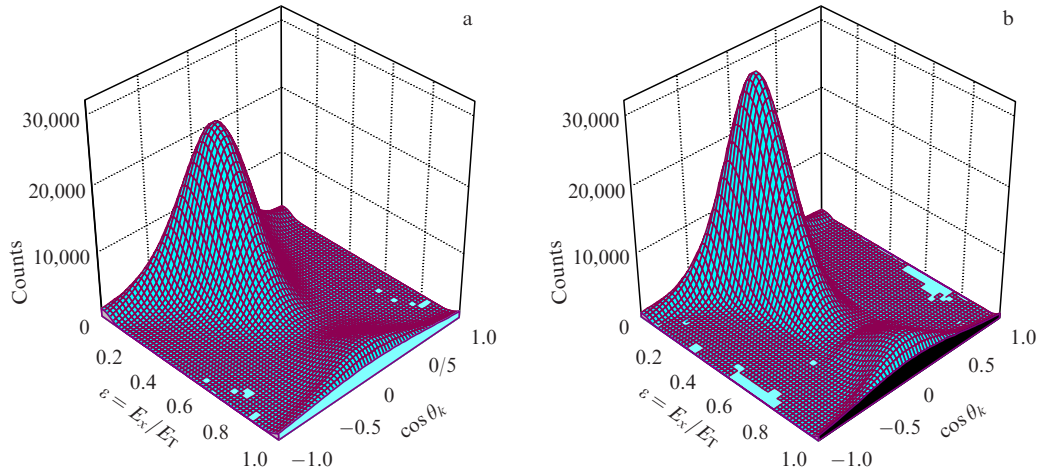


**Figure 19.** Effect of a classical extrapolation onto energy-angle correlations for the 2p-decay of the  $^{45}\text{Fe}$  ground state. (a) A distribution obtained in quantum-mechanical calculations with the Coulomb interaction cutoff at the distance of  $10^3$  fm. (b) The result of the classical extrapolation of the distribution given in panel (a) up to the distance of  $10^5$  fm.

impossible here because of the data insufficiency: the population cross sections for nuclei like  $^{45}\text{Fe}$  have the order of picobarns. Thus, these experiments are and will remain at the very limit of capabilities today and in the nearest future. However, it was revealed [64] that in order to describe the experimental data on  $^{45}\text{Fe}$  a proper allowance must be made for the effects related to the Coulomb interaction at large radii (Fig. 20). In this field, the last significant achievement is concerned with high-precision correlation measurements for the 2p-decay of the  $^{16}\text{Ne}$  ground state [93]. This nucleus is quite a light one and may be referred to as the democratic 2p-emitter (see Section 3.5). The Coulomb effects in such a nucleus are relatively weak compared to those in  $^{45}\text{Fe}$ ; however, the high resolution of the experiment and huge number of statistics allow us to achieve agreement with theoretical predictions at a high confidence level (Fig. 21). Based on the results of Ref. [93], we can state that the problem of three-body Coulomb interaction in the continuum for nuclear systems (where all the Coulomb interactions are repulsive) is solved from the practical viewpoint.

In solving the two-proton radioactivity problem, an interesting hierarchy arises. In order to numerically evaluate

the system's energy with a high precision, equations (23) should be solved for radii ranging up to  $\rho \sim 20\text{--}30$  fm. In order to stabilize the width calculations, the numerical solution at distances highly exceeding the radius of a proton exit from under the Coulomb barrier is needed. For example, for  $^{45}\text{Fe}$  with the decay energy of  $\sim 1$  MeV, this distance is  $\rho \sim 200\text{--}300$  fm. For approximate calculations of correlations, one needs to take  $\rho \sim 1000\text{--}2000$  fm. And, at least, the total convergence of the momentum distributions is expected for  $\rho \sim 10^4\text{--}10^5$  fm.

Thus, consideration of the different aspects of two-proton decay requires us to exceed the nuclear scales and gradually leads us to atomic scales. At distances of  $\sim 10^5$  fm, the electron screening of the Coulomb potential is necessary to take into account [92].

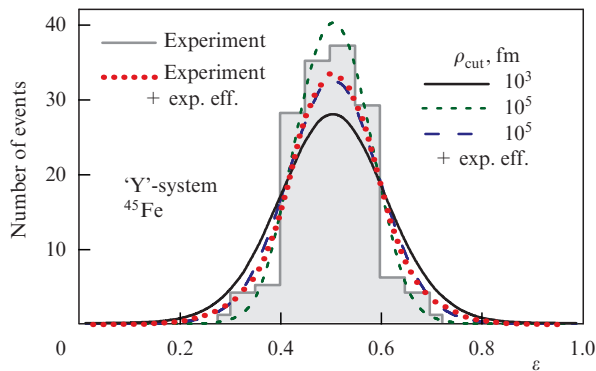


**Figure 20.** (Color online.) Energy distribution for the  $^{45}\text{Fe}$  ground state in the Jacobian ‘Y’-system (in the core-proton channel). Distributions obtained by the cut-off of Coulomb interaction at  $\rho_{\text{cut}} = 10^3$  fm are compared with the result of classical extrapolation at  $\rho_{\text{cut}} = 10^5$  fm and experimental data. The results marked by ‘exp. eff.’ (experimental efficiency) consider the bias induced by the experimental setup.

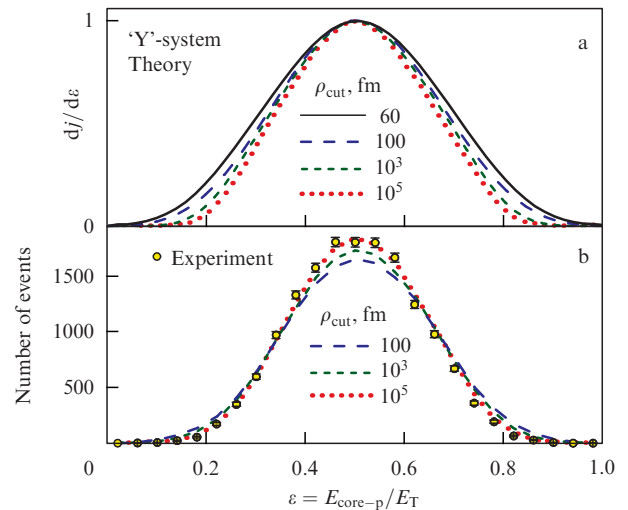


**Figure 21.** Energy distribution obtained for the  $^{16}\text{Ne}$  ground state in the Jacobian ‘Y’ system (in the core-proton channel). (a) Theoretical distributions calculated with different cut-off parameters  $\rho_{\text{cut}}$  of the Coulomb interaction given in the figure. (b) The distributions shown in panel (a), modified using MC simulations taking into account the bias induced by the experimental setup. The data are compared with the experimental results (circles with error bars).

### 3.7 Three-body mechanism of the Thomas–Ehrman shift

The concept of isobaric symmetry (i.e., neutron and proton equivalence inherent to the strong interaction) is one of the fundamentals of nuclear physics. At the level of nuclear structure, the isobaric symmetry manifests itself as follows: the  ${}^A Z$  nuclei at the proton and  ${}^A N = A(Z)$  nuclei at the neutron sides of the isobar are equivalent within an accuracy of small corrections related to the Coulomb interaction. However, while moving from the line  $N = Z$  towards the borders of stability, small corrections tend to increase to principally significant ones, and the clarification of the mechanisms of the isobaric symmetry breaking becomes important.

The Thomas–Ehrman shift (TES) is a well-known mechanism of the isobaric symmetry breaking. This idea was formulated in the early 1950's to explain the relative shifts of the single-particle levels with different parities in the  $s$ - $d$  shell for nuclei with  $A \sim 20$ . In the original work [117, 118], TES is interpreted as a geometric effect (Fig. 22). The Coulomb interaction pushes out the nucleon WF at the proton side of the isobar from the potential well; as a result, the radial properties of the WF change. The more the WF is radially extended, the lower its Coulomb energy. As a result,

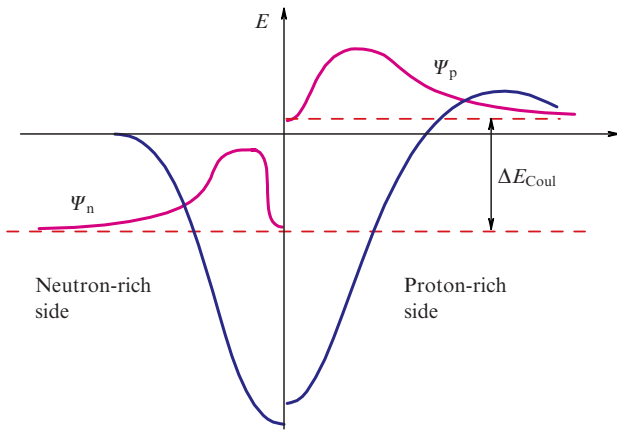


**Figure 22.** Illustration of the Thomas–Ehrman shift mechanism for a single-particle WF.

the real Coulomb shift  $\Delta E_{\text{Coul}}$  appears to be smaller than the perturbative Coulomb shift  $\Delta E_{\text{Coul}}^{\text{pert}}$  calculated with the WF on the neutron side of the isobar. TES is thereby determined as

$$\Delta E_{\text{TES}} = \Delta E_{\text{Coul}} - \Delta E_{\text{Coul}}^{\text{pert}}, \quad E_{\text{Coul}}^{\text{pert}} = \langle \Psi_n | V_{\text{Coul}} | \Psi_n \rangle. \quad (29)$$

TES would be equal to zero in the case of carefully fulfilling isobaric symmetry.

In Ref. [119], a phenomenological analysis with the use of charge-symmetrical mass formulae was performed. Using significant experimental material it was shown that TES is not limited by odd nuclei and quickly grows beyond the stability border.

A specific three-body mechanism of TES, essentially enhancing the standard ‘geometrical’ mechanism for even nuclei, was predicted in the three-body model in Ref. [120] by the example of the  ${}^{12}\text{O}$  and  ${}^{16}\text{Ne}$  nuclei—two-proton emitters.

Let us consider WFs of mirror even nuclei from the  $s$ - $d$  shell in schematic spectroscopic terms, taking only two valence nucleons into account:

$$\begin{aligned} \Psi({}^A N) &= \alpha[s^2]_0 + \beta[d^2]_0, \\ \Psi({}^A Z) &= \tilde{\alpha}[s^2]_0 + \tilde{\beta}[d^2]_0, \end{aligned} \quad (30)$$

with the total spin  $J^\pi = 0^+$  of the system. When  $s$ - and  $d$ -wave orbitals are nearly degenerate (which is typical enough of the  $s$ - $d$  shell), the amplitudes of the  $[s^2]_0$  and  $[d^2]_0$  configurations can be comparable,  $\alpha \sim \beta$ , on the neutron side of the isobar  $\Psi({}^A N)$ . In this case, the configurations  $[s^2]_0$  and  $[d^2]_0$  are close to degeneration and are in a delicate balance. The addition of the Coulomb interaction can disturb this balance, as the  $[d^2]_0$  configuration corresponds to a larger Coulomb energy than the  $[s^2]_0$  one:  $\tilde{\alpha} > \alpha$  and  $\tilde{\beta} < \beta$ . Figure 23 illustrates this process with theoretical calculations, where the Coulomb interaction with the valence nucleons gradually varies from zero up to a proper value in the Wigner isobaric partner for the  ${}^{12}\text{Be} - {}^{12}\text{O}$  and  ${}^{16}\text{C} - {}^{16}\text{Ne}$  pairs. The predicted scale of the isobaric symmetry breaking is tens of percent, depending on the weights of the dominant configurations of the valence nucleons.

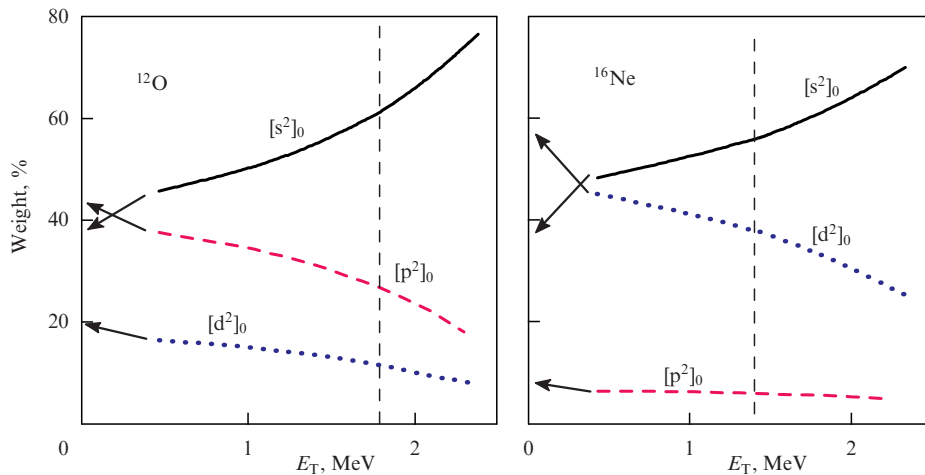


**Figure 23.** Changes in weights of the  ${}^{12}\text{O}$  and  ${}^{16}\text{Ne}$  WF components due to the three-body TES mechanism. The vertical dashed lines correspond to the experimental values of the  ${}^{12}\text{O}$  and  ${}^{16}\text{Ne}$  decay energies. Arrows point to the values of these weights in the Wigner isobaric partners,  ${}^{12}\text{Be}$  and  ${}^{16}\text{C}$ .

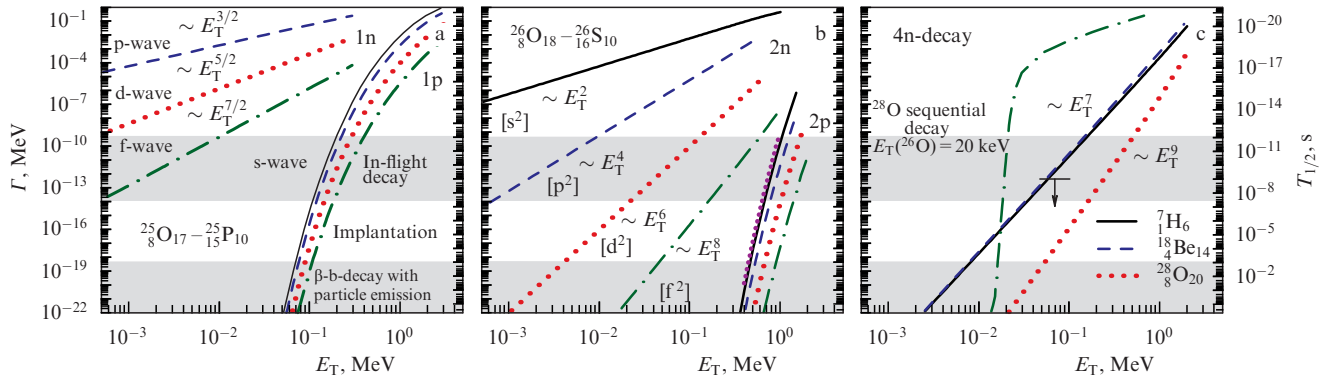


**Figure 24.** Lifetime estimations for decays with simultaneous emission of one (a), two (b), and four (c) neutrons. The arrow in figure (c) shows the limit for the  ${}^7\text{H}$  lifetime obtained in Ref. [122] (see Section 5.8).

For a long time, the results of Ref. [120] were questionable, since the other characteristics, which were predicted, namely, the widths of the  ${}^{12}\text{O}$  and  ${}^{16}\text{Ne}$  ground states, were expected to be much less than experimental values available at that moment. This problem was solved in recent experiments of a new generation, showing agreement with the theory for  ${}^{12}\text{O}$  [102] and an absence of a discrepancy for  ${}^{16}\text{Ne}$  [93]. New high-precision data on the energy of the  $0^+$  and  $2^+$  states of  ${}^{16}\text{Ne}$  allowed testing the theoretical calculations at a new level of precision [121]. Thus, the three-body TES mechanism can be considered confirmed for the  $0^+$  and  $2^+$  states—the states of two-proton emitters.

### 3.8 Long-living 2n/4n-emitters

A natural question might rise: if proton/two-proton radioactivity exists, is this also true for neutron/two-neutron radioactivity? It should be reminded that extremely narrow neutron resonances with widths comparable to electromagnetic ones ( $\Gamma \sim 10^{-9}$  MeV) are observed in the excitation spectra of heavy nuclei. These resonances have quite high decay energies; their narrow widths are entirely related to their nonsingle-particle origin (a low affinity of the internal nuclear structure to the single-particle continuum WF). However, we speculate on radioactive decays of the *ground states* of an almost single-particle origin. In the case of neutron radioactivity, the answer is quite straightforward, because it demands the simplest estimates of the potential barrier penetrability (Fig. 24). For s-wave neutron emission, the concept of the width (or the lifetime) is inapplicable at all, since there is no centrifugal barrier, and the emerging threshold singularity is considered as a *virtual state*. The characteristic threshold time in the sense of the radioactivity is that on the order of 1 ps. The shorter times are related to the resonance effects. In order to refer to the time scales of radioactivity, the decays of the p- and d-wave states should proceed with an energy much less than 1 keV. This is merely an f-wave, for which the scope of radioactivity is  $E_T < 10$  keV. Reaching the border of neutron stability for the f-shell ( $N > 28$ ) is now a long time away.

While studying the two-proton radioactivity, the longer characteristic lifetime than that for ordinary two-particle decays is one of the important qualitative signs. One of the reasons for that is a special feature of the mechanism of simultaneous particle emission related to a few-body dynamics. This feature can be illustrated within the formalism of the hyperspherical harmonic method (HHM), general-

ized for the case of  $A$  bodies. In this case, the WF in HHM and the kinetic energy take the following form:

$$\begin{aligned} \Psi &= \sum_{K\gamma} \frac{\chi_{K\gamma}(\rho)}{\rho^{(3A-4)/2}} \mathcal{J}_{K\gamma}(\Omega), \\ 2M\hat{T}\chi_{K\gamma}^{(+)}(\rho) &= \left[ \frac{d^2}{d\rho^2} - \frac{\mathcal{L}(\mathcal{L}+1)}{\rho^2} \right] \chi_{K\gamma}^{(+)}(\rho), \\ \mathcal{L} &= K + \frac{3A-6}{2}. \end{aligned} \quad (31)$$

Apparently, one particular case of generalized formulas (31) is the common two-body problem,  $A = 2$ . In this case, the hyperharmonics become the common spherical function,  $\mathcal{J}_{K\gamma} \rightarrow Y_{lm}$ , the generalized orbital angular momentum  $\mathcal{L} = K$ , and the hypermomentum  $K \rightarrow l$ . Expressions (31) allow one to estimate the minimum centrifugal barrier arising in this quantum-mechanical system (see Table 1). Thus, the zero barrier in the s-wave is the minimum one for one-neutron emission. For two-neutron emission ( $A = 3$ ), the minimum barrier differs from zero even for the lowest principal quantum number  $K = 0$ . However, for four-neutron emission ( $A = 5$ ), the minimum value of the principal quantum number is necessarily  $K = 2$  in order to satisfy the Pauli principle for four similar particles (with  $K = 0$ , this is impossible). Therefore, for special processes where sequential decays are prohibited and the particles have been simultaneously emitted, a fast increase in the height of effective centrifugal barrier (31) occurs with increasing the number of particles. The widths estimated in Ref. [24] for the 2n- and 4n-decays show that one can expect long-living true 2n- and 4n-emitters in quite realistic decay energy ranges.

Prospects for the discovery of new types of radioactivity are raising definite interest, albeit tempered by the complexity of the problem. The closest candidates for this search are  ${}^7\text{H}$  (4n),  ${}^{16}\text{Be}$  (2n),  ${}^{26}\text{O}$  (2n), and  ${}^{28}\text{O}$  (4n). Thus, the systematics of the decay energies of  ${}^7\text{H}$ ,  ${}^{26}\text{O}$ ,  ${}^{28}\text{O}$  and their subsystems are

**Table 1.** HHM centrifugal barriers for simultaneous emission of 1, 2, and 4 neutrons.

$A$	Minimum $K$	Barrier	Minimal barrier
2	$l = 0$	$l(l+1)/r^2$	0
3	$K = 0$	$(K+3/2)(K+5/2)/\rho^2$	$15/(4\rho^2)$
5	$K = 2$	$(K+9/2)(K+11/2)/\rho^2$	$195/(4\rho^2)$



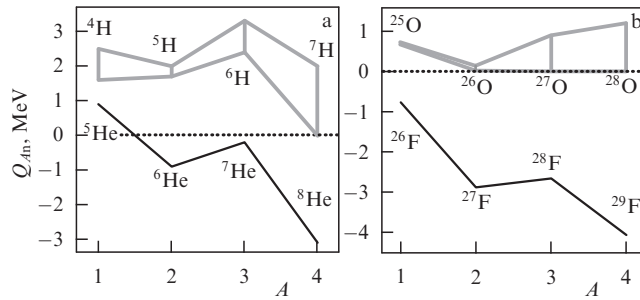
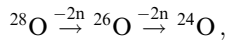


**Figure 25.** Decay energy ( $Q_{Ah}$ ) systematics for  $A$ -nucleon detachment in the nuclei  ${}^4\text{H} + A_n$  (a) and  ${}^{24}\text{O} + A_n$  (b). The grey lines bound the region related to the experimental uncertainty. For comparison, similar systematics are shown for closest isotopes with  $Z + 1$ :  ${}^5\text{--}8\text{He}$ , and  ${}^{26\text{--}29}\text{F}$ , which have been more extensively studied.

given in Fig. 25. One can see that the decay schemes of these systems can reasonably satisfy the conditions for true  $2n$ - and  $4n$ -decays. One of the first attempts to observe the  $4n$ -radioactive decay in  ${}^7\text{H}$  was made at the ACCULINNA facility (see Section 5.8). The upper bound for the lifetime was only obtained. In this sense, the  ${}^{26}\text{O}$  nucleus has appeared to be of special interest. Experimentalists have gradually decreased the upper bound on its decay time in the last years. An indication that the  ${}^{26}\text{O}$  lifetime is about picoseconds has been obtained in Ref. [123]. References [124, 125] ‘narrowed down’ the  ${}^{26}\text{O}$  decay energy to the very tight range  $0 < E_T < 100$  keV. A quite precise measurement of the  ${}^{26}\text{O}$  decay energy was recently declared,  $E_T \sim 10$  keV, in Ref. [126]. It should be noted that the decay energy [126] and lifetime [123] contradict the refined data on the  ${}^{26}\text{O}$  lifetime [127]. The  ${}^{26}\text{O}$  decay energy remains crucial for determination of the  ${}^{28}\text{O}$  decay mechanism as well. Sequential decay becomes possible at the quite low energy of the  ${}^{26}\text{O}$  ground state, viz.



and the energy dependence of the  ${}^{28}\text{O}$  lifetime quickly transforms into systematics for faster  $2n$ -decays (dashed–dotted curve in Fig. 24).

In general, this field stays under continuous study and is still quite far from the final reliable results.

## 4. Experimental techniques

To perform experiments with RIBs, an integrated installation comprising an accelerator (source of primary beam), primary target area with effective radiation protection, fragment separator, and low-background experimental area for the secondary beam is needed. The experimental area has to provide the ability to use a wide set of experimental equipment. In Sections 4.1–4.5, we will present the main elements of this installation operating at JINR FLNR.

### 4.1 U-400M accelerator

Accelerators at JINR FLNR were designed mainly assuming experiments on the production of superheavy elements and studies of their properties, which requires beams of high intensities. This gives us the opportunity to conduct world-class experiments exploiting other equipment with the relatively limited capabilities.

The ACCULINNA fragment separator [2, 26] operates at the output of heavy-ion beams from the U-400M isochronous

cyclotron with the magnet pole diameter of 4 m [128]. The four-sector cyclotron U-400M, with four dees, was designed to produce heavy-ion beams with the mass-to-charge ratio  $A/q = 2\text{--}5$ , accelerated to energies of 20–100 MeV per nucleon. Electron cyclotron resonance (ECR) source DECRIS-2 (Dubna Electron Cyclotron Resonance Ion Source 2), used to inject multicharged ion beams in the initial orbit of acceleration in the cyclotron, provides high-intensity beams for RIB production of ions with the nuclear charge numbers  $Z \leq 18$ . However, the energy range of beams used for RIB production is restricted by the ejection method of accelerated beams from the cyclotron orbit.

For cyclotron beam extraction, the charge-exchange method is applied to electron stripping in thin foils placed in the inner orbit of the cyclotron. It is the method of the most effective extraction of particles with the charge-exchange coefficient  $Z_{\text{out}}/Z_{\text{accelerated}}$  ranging within 1.33–1.67; however, it sets limits on the resulting energy range. The typical energy of the extracted beams (from Li to Ca,  $A = 7\text{--}48$ ) falls within the range of 32–55 MeV per nucleon. Exploiting the DECRIS-2 source, intensities of the  ${}^7\text{Li}$ ,  ${}^{11}\text{B}$ ,  ${}^{18}\text{O}$ ,  ${}^{32}\text{S}$  beams were in the range  $(1\text{--}3) \times 10^{13} \text{ s}^{-1}$  (from 1.5 to 5  $\mu\text{A}$ ). Replacing the DECRIS-2 source, operating at room temperature, by the superconducting ECR source DECRIS-SC2 [129] extended the range of heavy ions produced by U-400M. The beams of  ${}^{40}\text{Ar}^{12+}$ ,  ${}^{48}\text{Ca}^{14+}$ ,  ${}^{84}\text{Kr}^{21+}$  ions have been available at energies of 41, 39, 29 MeV per nucleon and intensities of 0.8, 0.15, 0.05  $\mu\text{A}$ , respectively.

### 4.2 ACCULINNA fragment separator

The ion-optical system of the ACCULINNA separator (Fig. 26) focuses onto the achromatic focal plane F3 the products of nuclear fragmentation of the primary beam emerging from the production beryllium target, placed in the object plane F1. The desired secondary RIBs are separated according to their magnetic rigidity  $B_{\text{RIB}}$  from the ions in the primary beam with  $B_{\text{HI}}$  and, to a large degree, from other fragmentation products. A wedge-shaped beryllium degrader is installed in the intermediate dispersive focal plane F2 (to obey achromatic conditions in the plane F3). The momentum acceptance of ACCULINNA is rather modest ( $\Delta p/p < 2.5\%$ ) (see Table 4 in Section 6) and is determined by the width of the open slits installed in the front of the wedge (maximum value of  $\pm 15$  mm). Setting of the second magnet D2 induction, taking into account the energy losses in the beryllium wedge, allows additional purification of the desired beam. The quality of the purification from admixtures (satellite products of fragmentation reactions) can reach more than 90%, e.g., for separator tuning in  ${}^6\text{He}$  and  ${}^8\text{He}$  beam production, when keeping the relation  $B_{\text{RIB}} > B_{\text{HI}}$  [26] for the magnetic fields. The purity is much less when the facility provides proton-rich beams and does not exceed a few percent (for the sake of a much wider set of nuclei, when the separator operates under conditions of  $B_{\text{RIB}} < B_{\text{HI}}$ ) [130].

An important condition for normal functioning of the separator consists in the capability of the production beryllium target to resist damage when the heat energy released in it during the ion beam bombardment reaches 1–2 kW. This requirement is satisfied for targets made of a beryllium water-cooled disk with a diameter of 80 mm and thicknesses from 0.3 to 2.0 mm, rotating with a frequency of 120 revolutions per minute (see, for example, the inset to Fig. 53b in Section 6.1). Table 2 shows the characteristics of secondary beams typical for the ACCULINNA separator.



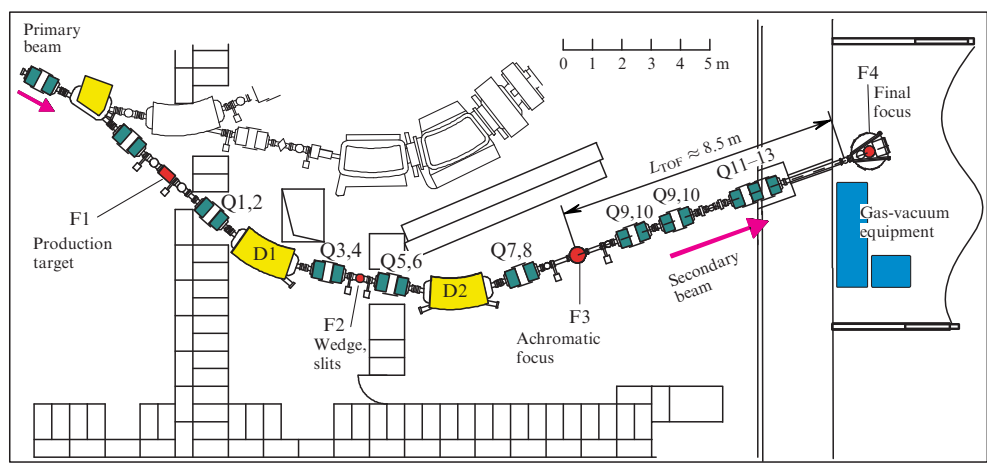


**Figure 26.** Schematic of the ACCULINNA fragment separator: F1 — object plane, F2 — focal plane with maximum dispersion, F3 and F4 — achromatic focal planes, D1 and D2 — dipole magnets, and Q1–Q13 — quadrupole magnets (lenses).

**Table 2.** RIB\* characteristics typical for the ACCULINNA\*\* facility.

HI	$E_{HI}$ , MeV per nucleon	RIB	$E$ , MeV per nucleon	$I$ , $s^{-1}$	$P$ , %
${}^7\text{Li}$	34	${}^6\text{He}$	25	$5 \times 10^5$	97
${}^{11}\text{B}$	32	${}^6\text{He}$	25	$1 \times 10^6$	70
${}^{11}\text{B}$	32	${}^8\text{He}$	25	$1 \times 10^4$	95
${}^{11}\text{B}$	32	${}^9\text{Li}$	25	$5 \times 10^5$	70
${}^{15}\text{N}$	49	${}^8\text{He}$	40	$1 \times 10^4$	92
${}^{15}\text{N}$	49	${}^{11}\text{Li}$	37	$2 \times 10^3$	40
${}^{18}\text{O}$	33	${}^{14}\text{Be}$	27	$3 \times 10^2$	20
${}^{18}\text{O}$	33	${}^{15}\text{B}$	27	$2 \times 10^4$	50
${}^{22}\text{Ne}$	44	${}^{18}\text{C}$	36	$5 \times 10^3$	60
${}^{10}\text{B}$	39	${}^7\text{Be}$	38	$1 \times 10^6$	50
${}^{16}\text{O}$	43	${}^{13}\text{O}$	25	$2 \times 10^4$	2
${}^{20}\text{Ne}$	53	${}^{14}\text{O}$	40	$5 \times 10^4$	0.5
${}^{20}\text{Ne}$	53	${}^{18}\text{Ne}$	40	$5 \times 10^4$	15
${}^{20}\text{Ne}$	53	${}^{17}\text{Ne}$	42	$3 \times 10^3$	3
${}^{32}\text{S}$	52	${}^{24}\text{Si}$	40	$1 \times 10^2$	1
${}^{32}\text{S}$	52	${}^{27}\text{S}$	38	$1 \times 10^1$	0.5

\* HI — heavy ion (primary beam),  $I$  and  $P$  — intensity and purity of secondary beam, respectively.  
\*\* Expected RIB intensities are 10–20 times higher for the ACCULINNA-2 fragment separator (see Section 6.1) due to significantly larger angular and momentum acceptances (see Table 4). The purity of the  ${}^{13}\text{O}$ ,  ${}^{14}\text{O}$ ,  ${}^{18}\text{Ne}$ ,  ${}^{17}\text{Ne}$ ,  ${}^{24}\text{Si}$ , and  ${}^{27}\text{S}$  beams (see the last six rows of this table) can be enhanced by a factor of 10–50, when working with a velocity filter, e.g., the radio frequency (RF) filter in the F3 plane [132].

The ACCULINNA facility is no different from other fragment separators in the sense of a large RIB energy spread ( $\Delta E/E \approx 8\%$ ), a significant angular range of radioactive nucleus trajectories in the beam (30 mrad), and the considerably large diameter of the radioactive beam cross-cut,  $\sim 2$  cm (full width at half maximum — FWHM). While working with RIBs of moderate intensities (less than  $3 \times 10^6 \text{ s}^{-1}$ ), the basic parameters (energy, path inclination angle, and particle hit coordinates on the experimental target) are individually determined for each incident ion of the secondary beam.

The beam diagnostic system of the ACCULINNA separator consists of two thin scintillation detectors and two multiwire proportional chambers [131]. Plastic scintillators are installed between the F3 and F4 planes on a 8-m flight path. The thickness of the scintillators varies between 50 and

500  $\mu\text{m}$  depending on the RIB atomic number. Measurements of velocity and specific energy loss in the thin scintillator for each ion allow its energy to be determined (with an accuracy of 0.5%), and its nuclear mass and atomic number to be unambiguously identified. Two multiwire proportional chambers installed at a distance of 60 cm from each other in front of the experimental target in F4 provide measurement of the trajectory inclination angle of the nucleus hitting the target (the angle is measured with an accuracy of less than 6 mrad). Thus, the coordinates of the impact point on the target are determined with an error of not more than 1.5 mm.

The technical parameters of the ACCULINNA fragment separator are substantially limited compared with those of other facilities. Available RIBs are restricted by nuclei with  $Z < 20$ , and their maximum energy is  $E < 40$  MeV per nucleon. However, the ACCULINNA facility also has some strong sides. The record-high intensity of primary beams at the U-400M cyclotron (up to 5  $\mu\text{A}$ ) is responsible for a high enough intensity of exotic nucleus beams with lower energies compared to other facilities. It should be emphasized that the typical RIB energy at the ACCULINNA separator, about 20–35 MeV per nucleon, is optimal for investigations of the nuclear structure manifesting itself in direct nuclear interaction reactions: elastic and inelastic scattering, transfer reactions, charge-exchange reactions, and reactions of quasi-free scattering (see discussion in Section 2). These circumstances, together with modern methods of the experiment arrangement and data analysis, including theory development, have allowed obtaining a set of world-class results with the ACCULINNA facility.

### 4.3 Particle and gamma-ray detectors

Modern detectors (mainly semiconductor, gaseous, and scintillating) are employed to register charged particles, neutrons, and gamma rays at the ACCULINNA facility. The detectors can be divided into two classes, which serve (a) to monitoring the secondary beam on its way to the secondary (experimental) target, and (b) to register products from radioactive beam interactions with target nuclei. Detectors of the first class were described in Section 4.2, and those of the second class will be discussed further below.

To ensure detailed information on the processes of RIB interaction with target nuclei in the ideal case, the products

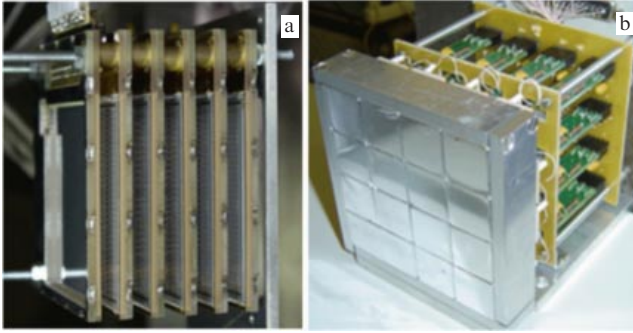


**Figure 27.** (a) Silicon telescope consisting of six layers each  $64 \times 64$  mm in size and 1 mm thick. (b) Scintillation part for the silicon telescope, comprising CsI(Tl) crystals, photodiodes, and preamplifiers.

should be detected in a solid angle close to  $4\pi$ , with high energy and position resolutions, and, certainly, with unambiguous identification of charged particles, neutrons, and gamma rays. A sufficiently high detection efficiency can be reached by using a specific setup with an efficiency of only about 1% with respect to the  $4\pi$ -geometry. This is possible, in many cases, due to the beneficial kinematics of the reaction product emission ‘forward–backward’ or ‘all forward’ (see, e.g., Refs [101, 130, 133–137]).

The detection system usually contains a few telescopes for charged particles and massive assemblies for neutron and gamma-ray registration. Telescopes (annular or rectangular) consist of several layers to allow products to be identified by means of the  $\Delta E1 - \Delta E2 - E$  method (Fig. 27). To measure ionization losses  $\Delta E$  and the emission angle of a particle, a few position-sensitive silicon detectors are installed (with thicknesses from 20 to 1000  $\mu\text{m}$ , with strips on one or both sides). Thick enough (from 25 to 40 mm) scintillation detectors can be installed behind them for measuring the residual energy.

An annular telescope consisting of a silicon detector (thickness of 1000  $\mu\text{m}$ , inside/outside diameter of 32/82 mm, double side segmented into 32 rings and 32 sectors) and assembly of 16 scintillation detectors made of petal-shaped CsI(Tl) crystals 25 mm thick, coupled with photomultipliers (PMT)<sup>6</sup>, is shown in Fig. 28. Typical energy resolution of the silicon detector ranges 30–50 keV for the 5.5 MeV alpha particles, while the characteristic resolution of scintillation detectors lies in the energy range of 250–300 keV for the 7.7 MeV alpha particles.

An example of the  $\Delta E - E$  identification of light charged particles produced in the reaction  $^{18}\text{Ne}$  (38 MeV per nucleon) + p and detected with this telescope is presented in Fig. 29.

If the maximum available energy resolution is needed and it is necessary to organize anticoincidence between layers (veto for background particles hitting the next layer), the telescope might consist only of silicon detectors (see work [136] and Fig. 27a). The assembly of 16 scintillation detectors applied for measurements of the residual particle energy in Ref. [135] is shown in Fig. 27b.

The DEMON (DéteCteur MOdulaire de Neutrons in French) multimodule array of large scintillation detectors

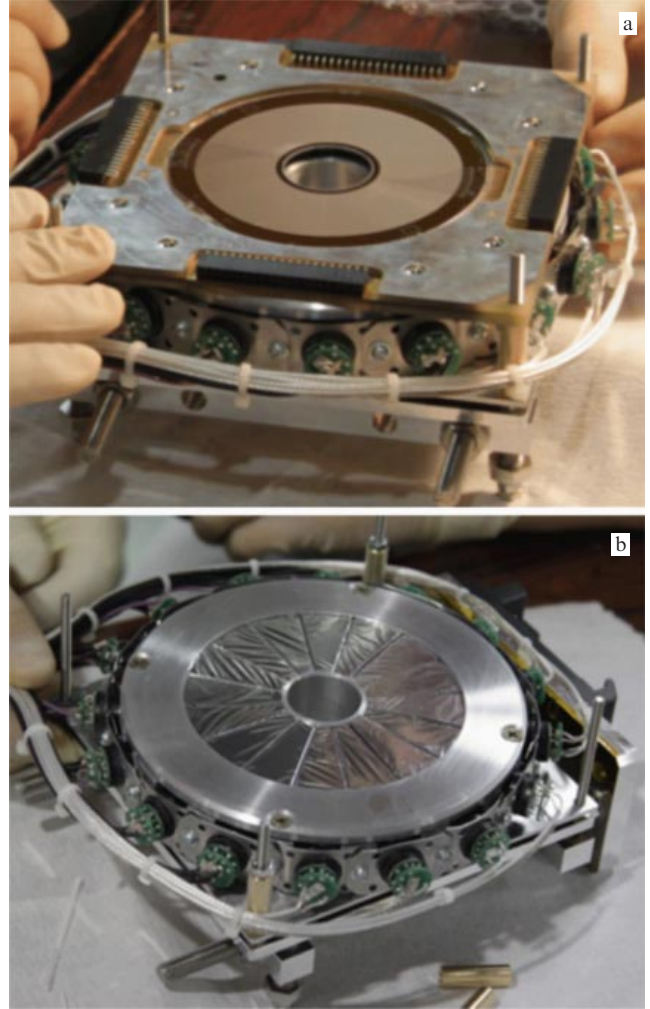


**Figure 28.** Assembled annular telescope (a) and its scintillation part (b). Lateral and back surfaces of the CsI(Tl) crystals are wrapped in VM2000 reflector 165  $\mu\text{m}$  thick, and the front surface is covered by thin (3  $\mu\text{m}$ ) foil made of aluminum-coated mylar.

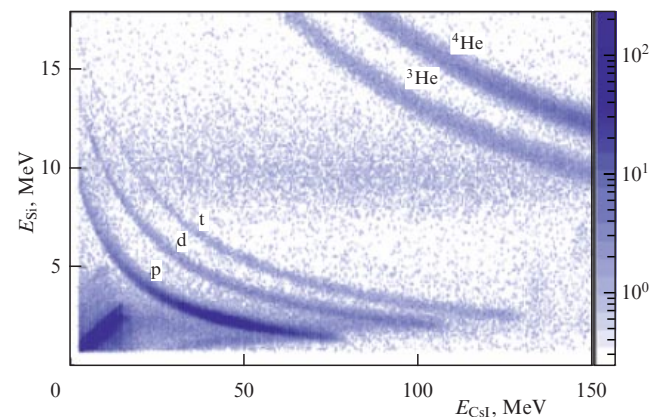


**Figure 29.** Particle identification by an annular telescope consisting of a segmented silicon detector 1 mm in thickness, and 16 modules of CsI(Tl)/PMT (crystal thickness of 25 mm).

<sup>6</sup> Hamamatsu R9880U-20 and R7600U-300 PMTs with enhanced quantum efficiency of the photocathode in the red region were applied, providing the best energy resolution of CsI(Tl) crystal-based detectors.

[139] was used to detect neutrons in experiments [26, 133, 134, 136, 138]. Each DEMON module consists of a sealed cylinder (diameter of 160 mm, length of 200 mm) filled with

liquid scintillator NE213 and coupled to a PMT.<sup>7</sup> Since 2012, more compact neutron detectors consisting of stilbene crystals (80 mm in diameter, and 50 mm in length) and fast-operating PMTs with photocathode diameters of 3 inches<sup>8</sup> [140] have been installed in experiments with radioactive beams at ACCULINNA. The stilbene-based detectors are superior to DEMON modules in their characteristics (amplitude and time resolutions,  $n-\gamma$  identification, operation time), and they are optimal for neutron detection in the energy range up to 20 MeV. The total number of such detectors, designed and mounted in JINR FLNR, amounts to 32 and will be increased to 48 by 2017.

Experiments with gamma-ray detection at the ACCULINNA facility have not been carried out yet. However, GADAST (Gamma Detectors Around a Secondary Target) scintillation modules [141] will be used soon in experiments at the ACCULINNA-2 facility. They were produced by staff of the ACCULINNA group in the framework of international collaboration within the project of modernization of equipment for the FRS (GSI) fragment separator. The assembly consists of 16 clusters with four detectors in each one. They are based on CsI(Tl) (trapezoid-shaped crystals with a volume of 371 cm<sup>3</sup>, coupled with PMT R7600U-300) (Fig. 30) and one cluster consisting of 16 LaBr<sub>3</sub>(Ce) detectors (cylindrical crystals 25 mm in diameter and 100-mm high, coupled with a PMT<sup>9</sup>). All the detectors are equipped with analogue electronics with an adjustable threshold of discrimination, delay-line, and built-in high-voltage PMT supply. The typical energy resolution of CsI(Tl) and LaBr<sub>3</sub>(Ce) for the 1174 keV gamma-line is  $\approx 7.5\%$  and  $\approx 3.2\%$ , respectively.

Replicate of the experimental study of the 2p-decay channel for the first excited state in <sup>17</sup>Ne (3/2<sup>-</sup>, 1288 keV), when direct measurement of the  $\Gamma_{2p}/\Gamma_{\gamma}$  ratio with an accuracy higher than that in Ref. [130] (see Section 5.9) will be possible, might offer an example of the effective application of the GADAST modules.

#### 4.4 Cryogenic <sup>1,2,3</sup>H, <sup>4</sup>He targets

Reactions of nucleon transfer (d, p), (t, p), (d, <sup>3</sup>He), (d, <sup>3</sup>H), (p, d), (p, t), (<sup>3</sup>He, d), (<sup>3</sup>He, n), (d, n), charge-exchange reactions (p, n), (<sup>3</sup>He, t), (t, <sup>3</sup>He), and reactions of quasifree scattering ( $\alpha, 2\alpha$ ), ( $\alpha, t\alpha$ ) provide various possibilities of



**Figure 30.** View of GADAST modules based on CsI(Tl) crystals with the sizes of 41 × 76 × 150 mm, assembled in the geometry optimal for installation at a distance of 50 cm from the target.

populating the states of exotic nuclear systems in the vicinities of the nucleon drip lines (see Fig. 4). Such experiments are inevitably related to studies of these reactions in the conditions of inverse kinematics. The involvement of targets containing hydrogen and helium isotopes is thus desired. Employment of cryogenic targets has important advantages and opens unique possibilities in many cases.

(1) Solid-state compounds are not available for preparing targets consisting of helium isotopes and, thus, a cryogenic cell is the only way to obtain a target with adjustable thickness.

(2) It is easy to produce targets of any thickness. Thin gaseous targets may be of small effective thicknesses, which are inaccessible for thin foils. It is simple to produce thick cryogenic targets and their thickness can easily be controlled (see the example in Section 5.8, where a liquid-deuterium target 56-mm thick was used).

(3) A gas/liquid target has a high level of homogeneity by definition. It is very hard to ensure the homogeneity of thin foil targets, which may complicate absolute calibration of the experimental data.

(4) The main background events relate to high carbon content in hydrogen-containing plastic targets. Reactions on carbon can effectively compete with the processes in hydrogen to be studied. In the case of cryogenic targets, the major sources of background are the iron windows of the cryogenic cell. Products of reactions on heavy materials of windows are usually kinematically well separated from relevant products of investigated process.

Cryogenic targets have been used in most experiments at the ACCULINNA facility [101, 122, 133–138]. Targets with hydrogen and helium isotopes were used, in many cases, with the ‘thickness’ varied from  $1 \times 10^{20}$  atoms per cm<sup>2</sup> to  $5 \times 10^{21}$  atoms per cm<sup>2</sup> in the gaseous or liquid phases. The convenient choice of gas temperatures covers the range of 23–30 K and 10–13 K, respectively, for hydrogen and helium targets.

Equipment deserving separate attention is the unique assembly of the cryogenic tritium target designed at the Russian Federal Nuclear Center–All-Russian Research Institute of Experimental Physics (RFNC–VNIIEF, Sarov) specially for the ACCULINNA facility [26, 142]. Despite the relatively low radioactivity (beta-decay with a half-life of 12.3 years and average energy release of 5.6 keV per decay), tritium represents a dangerous matter because of its biological activity. This makes tritium an object of strict regulation and imposes special requirements on the target cell design and equipment, providing safety of operation with gas. Therefore, the gas–vacuum system providing safety of operation with tritium at the ACCULINNA facility will be briefly described below. The design of other gas target cells is simpler than that for tritium (due to the lack of a safety system), but the gas–vacuum maintenance system itself is analogous.

A schematic of the tritium target cell construction, its image, and a picture of personnel in protective suits obligatory during the start-up/adjustment/disassembling work are presented in Fig. 31. The target cell is equipped with thin (12.5  $\mu$ m) windows (W1, W2) made of stainless steel 22 mm in diameter, germetically connected to the body by means of laser welding. The distance between the windows was chosen to be between 3 and 10 mm for different variants of the gas target. This distance varied between 0.4 and 1.0 mm for cells filled with liquid tritium. The tritium gas is delivered to the target cell through the tube T1. The cell connected with the tube T1 poses the first barrier for environmental protection.

<sup>7</sup> High-speed PMT XP4512B with a photocathode diameter of 5 inches.

<sup>8</sup> XP4312B and ET9822B.

<sup>9</sup> PMTs ET9106SB are used, specially designed for fast scintillators with high light output.



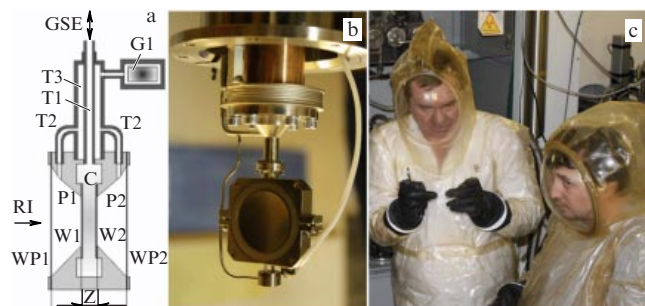


**Figure 31.** Schematic of the tritium target cell (a), its exterior view (b), and personnel in protective suits obligatory for starting/finishing work (c): C — target cell; W1, W2 — cell windows; GSE — gas supply/evacuation tube T1; P1, P2 — protective barriers with windows WP1, WP2 connected with getter G1 by tubes T2, T3.

The second protective barrier serves to assure protection reliability, preventing tritium leakage to the reaction chamber, where the target cell is placed and bombarded by a radioactive beam during the experiment. The second barrier includes volumes P1, P2 with windows WP1, WP2, connected to a getter G1 by means of tubes T2, T3. Tritium leaking through the target cell windows will be fully absorbed by the getter, which is titanium powder produced by special technology. The equilibrium pressure of the tritium gas above the activated titanium powder does not exceed  $10^{-8}$  Pa. The weight of the titanium getter is adjusted to provide full absorption of all tritium contained in both the target cell and the whole ballast volume utilized for its filling. The rated value of the gas pressure in the target cell and whole ballast volume used to deliver it (2 MPa) and leading to window damage was found empirically. The tritium gas pressure in the target cell should be less than 0.1 MPa for safety reasons in realistic conditions of experiments with separator beams.

The system of gas feeding and evacuation represents the most important part of the tritium target. Tritium is stored in porous uranium  $^{238}\text{U}$  in a chemically bound state for the designed system. The sorption capacity of uranium in the source for a pressure of 0.1 MPa is  $380\text{ cm}^3$  of the tritium gas. The source is designed in the form of an ampule with an external heater. The body of the ampule is constructed on the principle of a vessel with a hydrogen barrier, inside the volume of which the titanium getter is placed. The tubes connecting the tritium source with the target cell have two protective barriers, with the titanium getter joined to a protective vacuum volume where these tubes are placed.

Before filling the target with tritium, the source is attached to the pumped out ballast volume. The tritium pressure at room temperature in the source volume is about  $7 \times 10^{-4}$  Pa. The uranium ampule is heated to a temperature providing the necessary gas pressure for tritium delivery to the target cell. The tritium gas pressure of 0.1 MPa is established at the temperature of 680–705 K in the target cell. Coming back to room temperature on uranium leads to tritium evacuation from the whole volume to the source.

The gas target is cooled in order to get higher luminosity in measurements with the ACCULINNA facility. Depending on the gas pressure and hydrogen isotope, the temperature has been chosen in the range of 18–21 K for the liquid target, and 23–30 K for the gaseous one. A refrigerator installed on the reaction chamber is the main element of the target cooling system. Cooling of the target is implemented by means of a

copper rod. The heater is placed at the coupling of the rod with a cold target flange and serves to precisely adjust the target temperature. A thermodiode mounted on the body of the target cell is used for monitoring the cooling process dynamics and for temperature control. The time needed for the gas target to cool from room temperature to that of the tritium liquid-phase transition (21 K) is about 70 min. The cooling system is switched to the stabilization regime when the required temperature is reached. The operating temperature of the target is maintained at a stable level within  $\pm 0.1$  K.

The reaction chamber of the ACCULINNA separator containing the tritium target represents the third protective barrier preventing environmental radiation pollution. The chamber is pumped out until the pressure is  $3 \times 10^{-8}$  Pa. The exhaust gas is delivered from the pump to the cleaning system with sorbents absorbing the tritium residue. Before it reaches the atmosphere, the gas leaves the cleaning system and passes through the ionization chamber in the current mode, detecting the radioactive tritium content with respect to a level 100 times lower as the acceptable standards. The cleaning and radiation control system also includes other branches providing radiation safety in cleaning all systems of the tritium gas supply and evacuation.

#### 4.5 Optical time-projection chamber

The optical time projection chamber (OTPC) [143], designed at the University of Warsaw under the leadership of Professor M Pfützner, makes up another detection device deserving separate attention. A series of pioneering investigations have been done at the ACCULINNA facility at JINR [144, 145] and in other scientific centers, like NSCL [45, 146, 147], CERN [148], and GSI [149], using this apparatus.

The basic idea of OTPC, i.e., visualization of charged particle tracks in gas, is inherited from the Wilson chamber. This principle was applied at the dawn of development history of nuclear and elementary particle physics. The possibility of restoring three-dimensional images of tracks of the desired nuclei, rare channels of their decay with simultaneous emission of a few particles, and extraction of the time characteristics allowing the lifetime estimates in a wide time range,  $T_{1/2} \approx 1 - 500$  ms, characterize the advantages of this modern device.

OTPC technology opened new horizons in studies of extrarare events. Thus, correlations in two-proton radioactive decay [45] were measured using the OTPC for the first time, and  $\beta$ -delayed three-proton emission was discovered [146]. OTPC data processing can be rather labor-consuming, as it requires a visual identification of each event. On the other hand, this might be the only way to recognize really rare and unique events in the background. One example of  $\beta$ -delayed three-proton emission is very illustrative: this event is not extraordinarily rare and, if somebody is focused on searching for and studying such a complicated signal in a standard experiment with silicon telescopes, it could be discovered much earlier. The three-proton event is unambiguously identified by one look at the OTPC experiment (Fig. 32).

Visualization of light emission processes during charged particle motion using a highly sensitive digital camera and photomultiplier tube makes up a principle of OTPC operation. The active volume is filled with a gaseous mixture (typically 49% Ar + 49% He + 1% N<sub>2</sub> + 1% CH<sub>4</sub>) at atmospheric pressure with an  $\approx 90\text{ cm}^3\text{ min}^{-1}$  flow rate. The CCD (charge coupled device) camera Hamamatsu C9100-13 provides a two-dimensional image of tracks, while the third

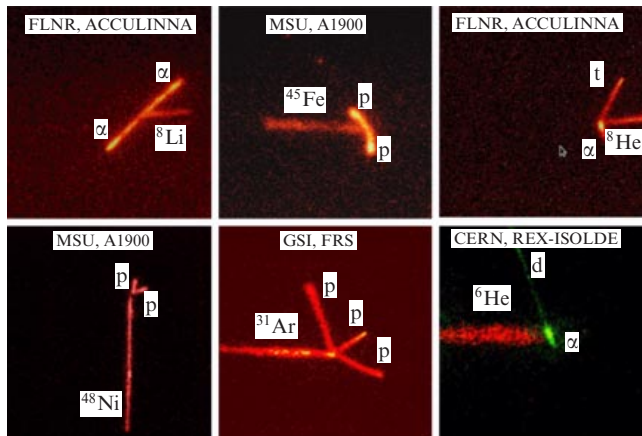


**Figure 32.** Examples of investigations into rare radioactive decay modes performed with OTPC (direct or  $\beta$ -delayed decay)  ${}^8\text{Li} \xrightarrow{\beta} \alpha - \alpha$ ,  ${}^{45}\text{Fe} \rightarrow {}^{43}\text{Cr} - 2p$ ,  ${}^8\text{He} \xrightarrow{\beta} \alpha - t - n$ ,  ${}^{48}\text{Ni} \rightarrow {}^{46}\text{Fe} - 2p$ ,  ${}^{31}\text{Ar} \xrightarrow{\beta} {}^{28}\text{Si} - 3p$ , and  ${}^6\text{He} \xrightarrow{\beta} \alpha - d$ .

coordinate is reconstructed through additional data analysis of the time signal from the PTM. Since the ionizing power of heavy ions from an investigated rare decay (for example, the  $\beta$ -delayed emission of  $2p$ ,  $3p$ ,  $\alpha - t - n$ , etc.) is 10–100 times larger than that for protons or alpha-particles, two operation regimes of the electron secondary emission amplification are available in the detector. Thus, by switching from one regime to the other during the operation only by changing the potential of the steering electrode, OTPC is able to detect (almost simultaneously) both heavy ions and light charged particles. Several examples of rare decay modes are demonstrated in Fig. 32.

Further advancement of the apparatus is planned: (1) manufacturing a leak-proof chamber operating with pressure varying within the range of 0.5–3.0 atm, which will provide the possibility of smooth variation of the typical track length depending on the task; (2) preview of tracks by means of two CCD chambers with different resolutions; (3) OTPC operation in the active target regime when filling the chamber with a more exotic gas mixture, e.g., 49% Ar + 49%  ${}^3\text{He}$  or 49% Ar + 49%  $\text{D}_2$ , which will allow investigating both rare modes of decay and reactions with exotic nuclei.

## 5. Research at the ACCULINNA facility

In this section, the most interesting experimental results obtained at the ACCULINNA facility in JINR FLNR are discussed.

### 5.1 Dineutron structure of the ${}^6\text{He}$ neutron halo

Representatives of a special form of nuclear structure, Borromean nuclei (see Section 3.2), have been found in the vicinity of the neutron drip line [150]. The  ${}^6\text{He}$ ,  ${}^{11}\text{Li}$ , and  ${}^{14}\text{Be}$  nuclei can be considered planetary systems with a compact inert ‘core’ and two ‘valence’ neutrons significantly distanced from the core. No single valence neutron can be bound with the core, while the neutron pair together with the core forms a long-living nuclear system with a neutron halo (see Section 3.2). The Borromean  ${}^6\text{He}$  nucleus is an especially interesting representative of the halo nuclei, as its  ${}^4\text{He}$  core is a compact, tightly-bound nucleus which with high reliability can be regarded as structureless. In this relation, experimental confirmation of the  ${}^6\text{He}$  halo structure, which according to

precise theoretical calculations [56] is a mixture of the dineutron and cigar-shaped configurations (see Fig. 11), is crucial.

Available calculations [56] apparently eliminate the significant probability of the  $t - t$  clusterization of  ${}^6\text{He}$ . Oppositely, calculations performed in the shell model [151,152] predict an even somewhat larger absolute value of the spectroscopic amplitude  $A_S \approx -1.3$  for the  $t - t$  clusterization of  ${}^6\text{He}$  compared with that for  $\alpha - 2n$  clusterization in this nucleus ( $A_S \approx 1.06$ ). Computations [151] also give comparable values of probabilities of the  $\alpha - d$  ( $A_S \approx -1.07$ ) and  ${}^3\text{He} - t$  ( $A_S \approx 1.0$ ) configurations in the neighboring  ${}^6\text{Li}$  nucleus, earlier disclosed from angular dependence in the cross section measurements [153, 154] for the  ${}^6\text{Li}(p, {}^3\text{He}){}^4\text{He}$  reaction.

To reveal the predicted features of the  ${}^6\text{He}$  wave function, we studied the transfer reactions in hydrogen and helium target nuclei bombarded with  ${}^6\text{He}$  beams at energies of 20–30 MeV per nucleon. This energy is comparable to the typical Fermi energy of the nucleon motion in the nucleus. Transition to higher energies dramatically reduces the transfer reaction cross section. At low incident energies, the strong coupling of the multistep mechanisms of transfer reactions complicates the data interpretation.

Two studies performed with  ${}^6\text{He}$  beams at the ACCULINNA fragment separator were devoted to neutron halo structure studies. In the first experiment from this run [155], two-neutron exchange was studied in the  ${}^6\text{He} - {}^4\text{He}$  reaction. A cryogenic helium target with the effective thick of  $5.6 \times 10^{20}$  particles per  $\text{cm}^2$  was irradiated by an  ${}^6\text{He}$  beam with the energy of 151 MeV. At this beam energy, the  ${}^6\text{He}$  elastic scattering cross section described by the optical model (OM) potential decreases sharply with angle growth. As a result, negligible contributions from the potential scattering to the elastic backscattering cross section for the angle  $\theta_{\text{cm}} > 120^\circ$  in the center-of-mass frame allow us to observe the two neutron exchange avoiding difficulties caused by interference with elastic scattering.

Therefore, the desired channels of elastic scattering and two-neutron transfer can be observed by coincidence detection of two nuclei,  ${}^6\text{He}$  and  ${}^4\text{He}$ , leaving the target in the whole available angular range. The measured angular dependence of the differential cross section of elastic scattering,  $d\sigma/d\Omega$ , is plotted in Fig. 33. The cross section data obtained at forward-scattering angles ( $\theta_{\text{cm}} = 17^\circ - 60^\circ$ ) were reproduced with a minor adjustment of the OM potential parameters already found in Ref. [156] for elastic scattering  ${}^6\text{Li} - {}^4\text{He}$  at the energy  $E_{\text{cm}} = 96.1$  MeV. For backscattering angles,  $\theta_{\text{cm}} = 125^\circ - 158^\circ$ , the measured cross sections exceed the cross sections obtained within the OM by three orders of magnitude. This apparently indicates the effect of the two-neutron exchange between the  ${}^6\text{He}$  and  ${}^4\text{He}$  nuclei. The corresponding curve in Fig. 33 shows the cross section obtained in Ref. [157] for the transfer reaction  ${}^4\text{He}({}^6\text{He}, {}^4\text{He}){}^6\text{He}(\text{g.s.})$  in the distorted wave Born approximation (DWBA), leading to  ${}^6\text{He}$  production in the ground state (g.s.). The main results of the rigorous approach [56] indicating the absence of  ${}^5\text{H}$  bound states and strong  $n - n$ -correlation in the structure of the  ${}^6\text{He}$  Borromean nucleus provide confidence that the dominant role in this reaction is played by one-step transfer of the neutron pair. The authors of Ref. [157] distinguished amplitudes of the  $2n$ -transition for the dineutron and cigar-shaped components of the wave function for the  ${}^6\text{He}$  Borromean nucleus. The contributions



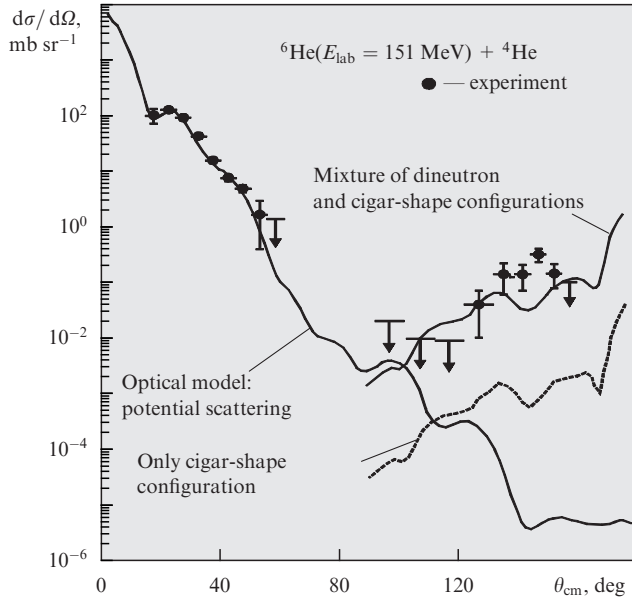


**Figure 33.** Experimental data (dots) and results of theoretical calculations (curves) of elastic scattering  ${}^6\text{He}(151\text{ MeV})-{}^4\text{He}$ .  $E_{\text{lab}}$  is the energy in the laboratory frame.

from these configurations to the  ${}^4\text{He}({}^6\text{He}, {}^4\text{He}){}^6\text{He}$  reaction cross section at backscattering angles significantly differ. This fact reflects the large weight of the dineutron configuration in the  ${}^6\text{He}$  ground state. When the dineutron pair is distanced from the  $\alpha$ -core, emission of the 2n-transfer products at forward-scattering angles dominates. With an increase in transferred momentum, i.e., when the reaction proceeds at smaller impact parameters, the contribution from the cigar-shaped configuration to the reaction cross section grows.

Study [158] was devoted to the transfer reaction induced by an  ${}^6\text{He}$  beam irradiation (at the energy of 150 MeV) of the cryogenic hydrogen gas target. The cross section of the  ${}^1\text{H}({}^6\text{He}, {}^4\text{He}){}^3\text{H}$  transfer reaction obtained in this work at the angles  $\theta_{\text{cm}} = 40^\circ - 130^\circ$  is shown in Fig. 34. For comparison, the angular dependence of the cross section of the reaction  ${}^6\text{Li}(p, {}^3\text{He}){}^4\text{He}$ , measured in Ref. [154] at the incident proton energy of 25 MeV, is also plotted in this figure.

The difference between the angular dependences of the cross section for the two reactions is evident. First of all, the measured data exhibit the opposite character of the cross section asymmetry pronounced at forward and backward

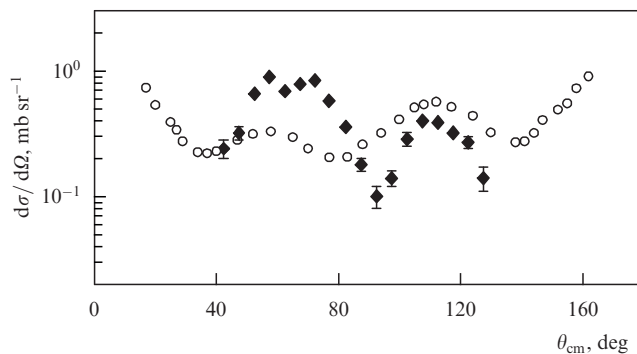


**Figure 34.** Comparison of the angular dependence of the cross section in the  ${}^1\text{H}({}^6\text{He}, {}^4\text{He}){}^3\text{H}$  and  ${}^6\text{Li}(p, {}^3\text{He}){}^4\text{He}$  transfer reactions, measured in Refs [158] (diamonds) and [154] (circles), respectively.

angles. The larger cross sections in the  ${}^6\text{Li}(p, {}^3\text{He}){}^4\text{He}$  reaction observed at backward angles correspond to the transfer of the  ${}^3\text{H}$  cluster from  ${}^6\text{Li}$  to the proton, while the deuteron transfer makes a major contribution to the cross section measured at the forward angles [153]. Therefore, the conclusion is obvious:  ${}^3\text{H}-{}^3\text{H}$  clusterization in  ${}^6\text{He}$  is less probable than  ${}^3\text{H}-{}^3\text{He}$  clusterization in  ${}^6\text{Li}$ . Second, oscillations in the angular dependence of the  ${}^1\text{H}({}^6\text{He}, {}^4\text{He}){}^3\text{H}$  reaction cross section are more pronounced than those for the reaction  ${}^6\text{Li}(p, {}^3\text{He}){}^4\text{He}$ . This probably signifies a purer mechanism of the reaction  ${}^1\text{H}({}^6\text{He}, {}^4\text{He}){}^3\text{H}$  corresponding to the zero angular momentum transfer. Third, the absolute values of the 2n-transfer cross sections obtained at forward scattering angles in the  ${}^1\text{H}({}^6\text{He}, {}^4\text{He}){}^3\text{H}$  reaction are greater than the deuteron transfer cross sections measured in the same angular range for the  ${}^6\text{Li}(p, {}^3\text{He}){}^4\text{He}$  reaction. Presumably, this result is explained by the larger size of the neutron halo in  ${}^6\text{He}$  than the dimension of the tightly bound  ${}^6\text{Li}$  system.

Qualitative conclusions about the angular dependence of the  ${}^1\text{H}({}^6\text{He}, {}^4\text{He}){}^3\text{H}$  reaction cross section presented above were analyzed within DWBA in Refs [157, 158]. This analysis leads us to the following conclusions:

- (1) the three-body  $\alpha$ -n-n configuration in the  ${}^6\text{He}$  nucleus has a weight close to 100%;
- (2) the  ${}^3\text{H}-{}^3\text{H}$  clusterization in  ${}^6\text{He}$  manifests itself much more weakly than the  ${}^3\text{H}-{}^3\text{He}$  configuration in the  ${}^6\text{Li}$  nucleus.

## 5.2 Study of the ${}^6\text{He}$ structure in quasifree scattering reactions

The quasifree scattering (QFS) reaction gives us a unique opportunity for experimental studies of internal correlations inherent to bound nuclear systems. The mechanism of the QFS reaction includes interactions with separate nucleons or clusters in the bound system under study, while the rest of the nucleus, called the 'spectator', is not involved in the reaction and keeps the properties of its motion, inherent to the bound state. The quasifree mechanism of interactions dominates at energies above 100 MeV per nucleon, where the probe particle wavelength is small compared to the size of the nucleus under study. However, it was shown in paper [159] that for light weakly bound nuclei with a strongly pronounced cluster structure, the QFS mechanism is the dominant type of interaction even at much lower energies. Reference [159] reported on the correlations observed for the two valence neutrons in the  ${}^6\text{He}$  nucleus becoming a spectator in the QFS reaction of the  ${}^4\text{He}$  target nuclei on the  $\alpha$ -cores of the  ${}^6\text{He}$  beam nuclei impinging on  ${}^4\text{He}$  with the energy of 25 MeV per nucleon.

The theoretical description of the reaction mechanism within the plane wave approximation assumes factorization of the  $T$ -matrix, which corresponds to the two independent vertices in the reaction diagram. One of the vertices is described by the amplitude of the free  $\alpha$ - $\alpha$  scattering, and the other one is described by the  ${}^6\text{He}$  wave function. Consistency between the angular distributions of the  $\alpha$ - $\alpha$  scattering in their center-of-mass system and results of calculations assuming the  $T$ -matrix factorization means that the spectator does not participate in the reaction and its momentum distribution in the  ${}^6\text{He}$  center-of-mass frame corresponds to its motion in the initial nucleus.

Measurement results [159] indicate that events referred to the QFS are localized in the corresponding domain of the

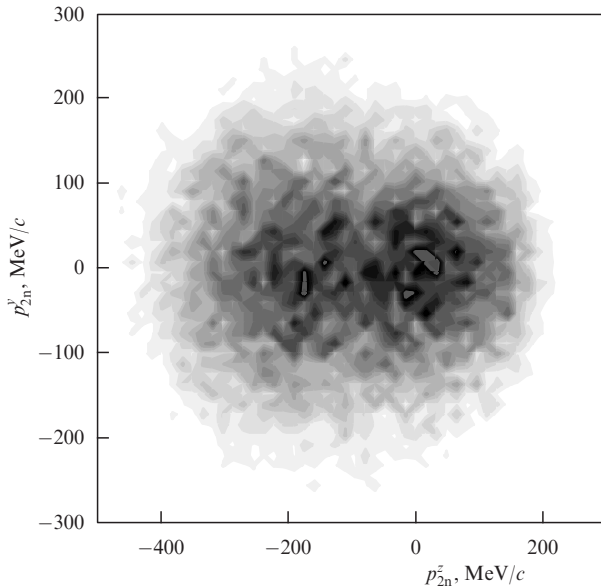


**Figure 35.** Spectator momentum distribution (two neutrons) in the center-of-mass system of an  ${}^6\text{He}$  projectile in the quasi-free scattering reaction  $(\alpha, 2\alpha)$ .

phase space and are confidently separated from the background events. The momentum distribution of the spectator in the center-of-mass frame of the  ${}^6\text{He}$  projectile is given in Fig. 35. Events conforming to the QFS mechanism are concentrated in the origin of the coordinate system ( $p_{2n}^y = 0$  and  $p_{2n}^x = 0$ ), which corresponds to a spectator velocity equal to the incident nucleus velocity.

Detailed experimental data for the QFS reaction with an unbound spectator comprising two neutrons were obtained in work [159]. Very special momentum correlations of the two neutrons, well-known for  ${}^6\text{He}$  theory, were experimentally observed for the first time. In Fig. 36, the distribution of the obtained events is given as a function of hyperangle

$$\tan \theta_{\alpha} = \sqrt{\frac{E_{nn}}{E_{\alpha-2n}}}.$$

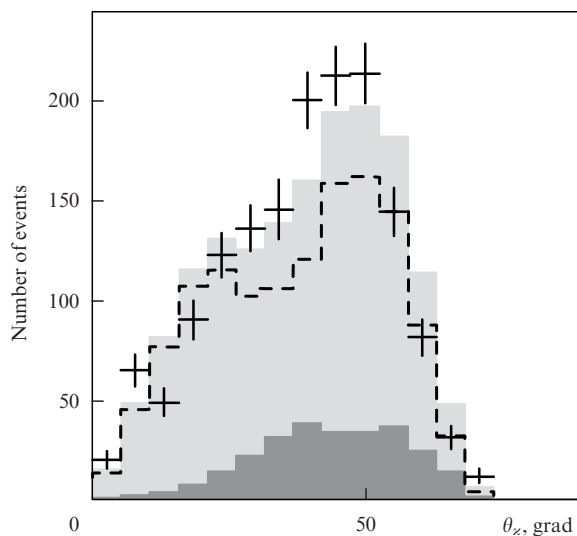


**Figure 36.** The hyperangular ( $\theta_{\alpha}$ ) distribution of events obtained in the quasifree scattering reaction of  ${}^6\text{He}$ . The number of events in the histogram is given for intervals of  $5.3^\circ$ .

The clearly observed asymmetry of this distribution is the result of the contribution from the dineutron (small values of the hyperangle) and cigar-like (large values of the hyperangle) components of the  ${}^6\text{He}$  three-body wave function.

### 5.3 ${}^9\text{He}$ : unambiguous spectrum identification

The results of  ${}^9\text{He}$  studies in the transfer reaction  $d({}^8\text{He}, p)$  [135] deal with one of the most interesting and problematic light nuclear systems, on the one hand, and are the most demonstrative from the viewpoint of the correlation method applied to the study of direct reactions, on the other hand. It was pointed out in Section 2.2 that unambiguous spin-parity identification for continuum states decaying via particle emission is made possible by the use of the angular correlation data, when (i) the reaction proceeds with special kinematics ('zero geometry'), and (ii) spinless particles participate in the reaction. In the case of  ${}^9\text{He}$ , unambiguous spectrum identification appeared to be accessible, though no 'zero geometry' was used and a particle with spin was transferred.

Before appearing Ref. [135] there had been two problematic topics related to the study of the  ${}^9\text{He}$  spectrum. Consistent results were obtained in Refs [160–162], assigning energy  $E_T = 1.1\text{--}1.3$  MeV for the  $p_{1/2}$  state, and  $E_T = 2.2\text{--}2.4$  MeV for the  $p_{3/2}$  state. Along with this, both states have quite small widths:  $\Gamma < 0.1$  MeV and  $\Gamma < 0.7$  MeV, respectively. This interpretation gives rise to questions, since the  $p_{3/2}$  subshell in  ${}^8\text{He}$  is closed, and it is expected that the  $p_{1/2}$  ground state of  ${}^9\text{He}$  is single-particle and, hence, the wide one, while the  $p_{3/2}$  state in the higher shell is separated from it by an energy of about a few MeV. Another problematic topic is related to the limitation for the scattering length  $a_s < -10$  fm in the  $s_{1/2}$ -state of  ${}^9\text{He}$ , discovered in Ref. [163]. This large negative value of the scattering length means that the state with  $l = 0$  is almost bound and in terms of the shell model the gap between the p- and s-d-shells is nearly absent. These abnormal features of  ${}^9\text{He}$  are not confirmed in theory (see, for example, paper [164]).

The layout of experiment [135] is shown in Fig. 37. The  ${}^8\text{He}$  nucleus with the energy of  $\approx 25$  MeV per nucleon is incident on a cryogenic deuterium target and picks up a neutron populating the  ${}^9\text{He}$  states. The recoil proton flies in the backward direction in the laboratory frame and is detected with an annular detector. Registration of the proton in coincidence with  ${}^8\text{He}$  emitted in forward direction allows the reconstruction of the full kinematics of the reaction. The measured  ${}^9\text{He}$  spectrum has two wide bumps (Fig. 38). The

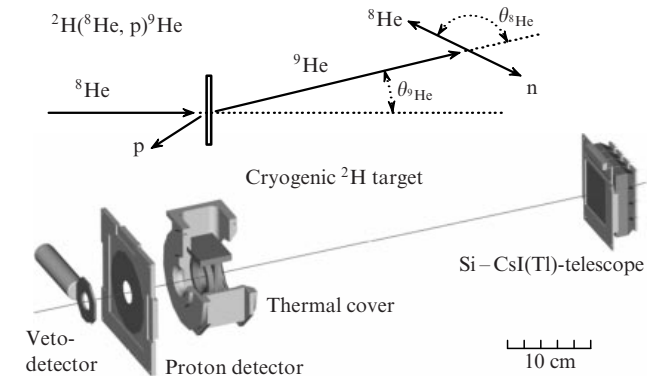


**Figure 37.** Layout of experiment [135] on studying  ${}^9\text{He}$  nucleus in the transfer reaction  $d({}^8\text{He}, p)$ .

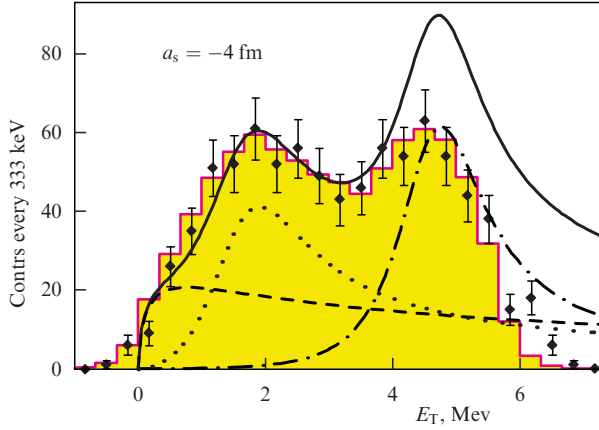


**Figure 38.** Fitting the  ${}^9\text{He}$  spectrum with theoretical curves. Contributions from the  $1/2^+$ ,  $1/2^-$ , and  $5/2^+$  states are shown by dashed, dotted, and dash-dotted lines, respectively. In fitting, the experimental bias effects are taken into account.

right slope of the high-energy bump related to the kinematic cut-off does not permit us to conclude its real shape. Narrow low-lying states are not observed. The energy resolution in the experiment is not high, of about 400 keV. Is this the reason why we do not see narrow resonance peaks?

An answer to this question follows from the correlation analysis. The  ${}^8\text{He}$  angular distributions in the frame attached to transferred momentum are given in Fig. 39. After algebraic transformation performed in the angular momentum theory, it appears that Figs 38 and 39 permit a unique interpretation in terms of interference between the s, p, and d states. All possible correlation functions for these three states with different  $l$  are given below:

$$x = \cos \theta_{s\text{He}}, \quad A_{ll'} = |A_l||A_{l'}|, \quad \phi_{ll'} = \arg(A_l A_{l'}),$$

$$W(s_{1/2}, p_{1/2}, d_{5/2}) \sim 4A_{00} + 4A_{11} + 3(1 - 2x^2 + 5x^4)A_{22} + 8xA_{10} \cos \phi_{10} + 4\sqrt{3}x(5x^2 - 3)A_{12} \cos \phi_{12}. \quad (32)$$

$$W(s_{1/2}, p_{1/2}, d_{3/2}) \sim 2A_{00} + 2A_{11} + (1 + 3x^2)A_{22} + 4xA_{10} \cos \phi_{10} + 2\sqrt{2}(3x^2 - 1)A_{20} \cos \phi_{20}, \quad (33)$$

$$W(s_{1/2}, p_{3/2}, d_{5/2}) \sim 4A_{00} + 2(1 + 3x^2)A_{11} + 3(1 - 2x^2 + 5x^4)A_{22}, \quad (34)$$

$$W(s_{1/2}, p_{3/2}, d_{3/2}) \sim 2A_{00} + (1 + 3x^2)(A_{11} + A_{22}) + 2x(9x^2 - 5)A_{12} \cos \phi_{12} + 2\sqrt{2}(3x^2 - 1)A_{20} \cos \phi_{20}. \quad (35)$$

Here,  $A_l$  is the amplitude for the population of state with a certain  $l$ . As the given  $l$  appears in each term only on time, the indication of  $l$  is equivalent to that for  $j$ . One can see from Fig. 39 that the angular distribution in the lower energy region is almost isotropic, which testifies to the dominating s-wave. To provide a description in the high-energy region, the dominating Legendre polynomials with  $l > 1$ , i.e., d-waves, are required. The distributions exhibit forward-backward asymmetry both for the s-wave region and for the d-wave region. Such asymmetry can only be related to interference between the states with opposite parities (p-wave). In interference functions (32)–(35), the asymmetric term ( $\propto x, \propto x^3$ ) is *simultaneously* met for p-s- and p-d-interference merely in equation (32). Thus, the character of the data and peculiarities of the angular momentum algebra for a given reaction led us to an unambiguous conclusion about the presence of the  $s_{1/2}$ ,  $p_{1/2}$ , and  $d_{5/2}$  states in  ${}^9\text{He}$ .

Our explanation of the  ${}^9\text{He}$  spectrum only demands wide single-particle states (see Fig. 38), which is the most simple and natural suggestion. The data exclude the presence of a strong  $s_{1/2}$ -state with large negative scattering length,  $a_s < -20$  fm, and the best fit is provided with  $a_s \sim -4$  fm. It should also be noted that the theoretical study of the  ${}^{10}\text{He}$  properties [62,108] shows that the observed position of the  ${}^{10}\text{He}$  ground state imposes strong restrictions on the properties of the  ${}^9\text{He}$  low-lying states. Thus, according to this analysis, the negative values of  $a_s$  are practically excluded [108].

Notice that experiments [165, 166], performed after carrying out those in Ref. [135], did not change qualitatively the understanding of the  ${}^9\text{He}$  structure. Experiment [165] appeared to be mostly sensitive to the  $s_{1/2}$ -state properties. The deduced scattering length  $a_s = -(3.2 - 3.6)$  fm certifies conclusions [135] rejecting a large negative scattering length in this system. The properties attributed in Ref. [165] to the  ${}^9\text{He}$  negative parity states are entirely arbitrary and are not justified by any spin-parity identification procedure. Study [166] was performed with the use of the same reaction  $d({}^8\text{He}, p)$  as in Ref. [135] at approximately the same beam energy. However, the results of the analysis in Ref. [166] significantly differ from the data [135]. We consider the conclusions made in Ref. [166] to be arbitrary, as the statistics gathered in this work was several times less than those in Ref. [135], and the spin-parity identification appears to be not convincing (angular distributions in the  ${}^9\text{He}$  center-of-mass frame were obtained with very low statistics).

#### 5.4 ${}^5\text{H}$ : the ground state and spectrum

The  ${}^5\text{H}$  isotope was discovered in JINR FLNR in 2001 in collaboration with National Research Centre ‘Kurchatov

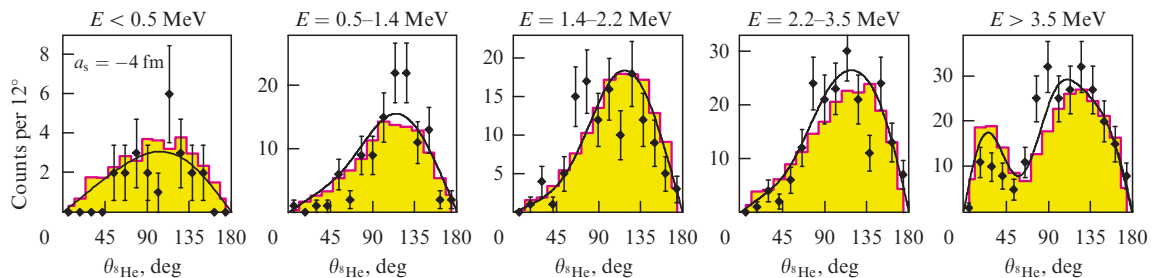


**Figure 39.** Angular distributions of  ${}^8\text{He}$  in the  ${}^9\text{He}$  center-of-mass frame attached to the transferred momentum for different regions of the  ${}^9\text{He}$  excitation energy. The number of events is normalized to the value in the angular range of  $12^\circ$ . Experimental data are marked by dots with error bars, the solid curve corresponds to theoretical results, and the histogram shows the results of MC simulations.

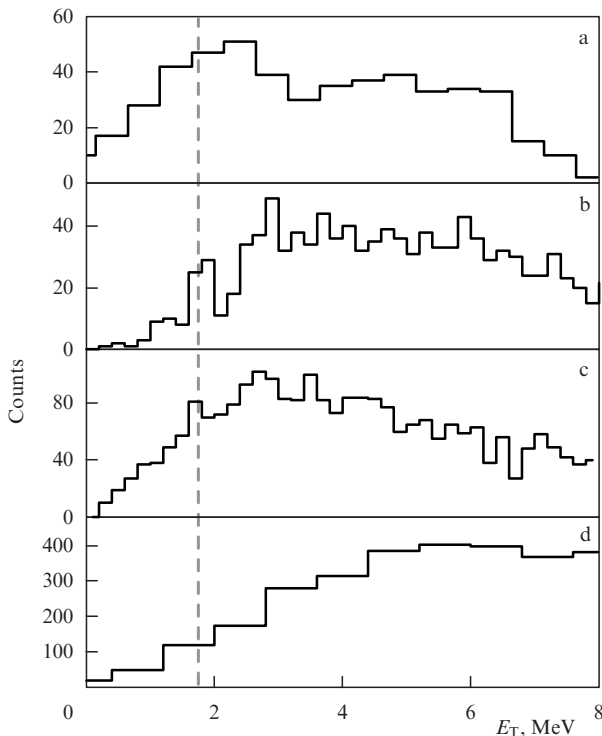


**Figure 40.**  ${}^5\text{H}$  spectra taken from Refs [167] (a), [168] (b), [169] (c), and [170] (d) preceding Ref. [133].

Institute' (NRC KI), RIKEN, and GANIL [167]. The  $p({}^6\text{He}, 2p){}^5\text{H}$  reaction of the proton knock-out from  ${}^6\text{He}$  was studied at the cryogenic hydrogen target (see Section 4.4). Quite wide resonance ( $\Gamma \approx 2$  MeV) was observed at energy  $E_T = 1.7$  MeV with respect to the three-particle ( ${}^3\text{H}-n-n$ ) threshold.

The subsequent experiments [168–170] gave very contradictory results (Fig. 40). In paper [169], the  ${}^5\text{H}$  invariant mass spectrum was obtained for the proton knock-out from  ${}^6\text{He}$  (240 MeV per nucleon) on a carbon target. The ground state energy and width were estimated to be  $\sim 3$  and  $\sim 6$  MeV, respectively. In Ref. [170], the  ${}^5\text{H}$  spectrum was obtained as the missing mass for the pion absorption reaction  ${}^9\text{Be}(\pi^-, \text{pt}){}^5\text{H}$ . This spectrum exhibits a weakly pronounced peak at  $E_T = 5.4$  MeV with  $\Gamma = 5.6$  MeV. In work [168] performed at the ACCULINNA facility, an alternative approach to the  ${}^5\text{H}$  study was applied, i.e., the  ${}^3\text{H}({}^3\text{H}, p){}^5\text{H}$  reaction of two-neutron transfer from tritium. The results of this work are consistent with those in Ref. [167] concerning the  ${}^5\text{He}$  ground state energy  $E_T = 1.8$  MeV, but an anomalously small value of  $\Gamma < 0.5$  MeV was obtained, the fact that is also inconsistent with theoretical predictions. Capability to identify the  ${}^5\text{H}$  spin-parity occurred in none of the above-mentioned studies.

From the theoretical viewpoint,  ${}^5\text{H}$  decay is referred to as democratic decay (see Section 3.5). For a relatively large decay energy ranging 2–3 MeV, the theory also predicts quite large values of widths,  $\Gamma > 1$  MeV [105]. For such short-lived systems, the resonance states in continuum spectrum tend to overlap, and the spectrum itself and the correlations become dependent on the reaction mechanism [106,107].

Correlation measurements performed in Refs [133, 134] offered an opportunity to resolve the experimental discrepancy and to reliably identify the low-energy  ${}^5\text{H}$  spectrum. In these studies, the reaction  ${}^3\text{H}({}^3\text{H}, p){}^5\text{H}$  was also examined,

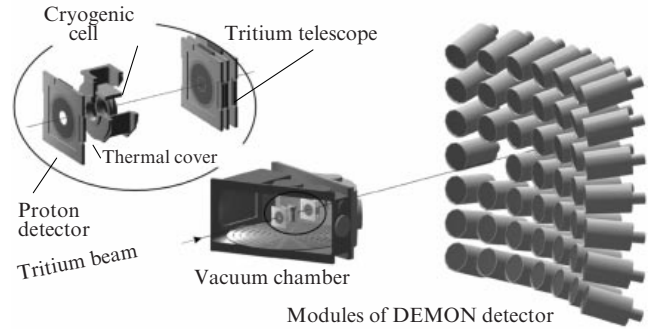


**Figure 41.** Layout of experiment [133,134] on the study of  ${}^5\text{H}$  in the  ${}^3\text{H}({}^3\text{H}, p){}^5\text{H}$  reaction.

but in different kinematic conditions (Fig. 41) compared to those in Ref. [168]. The recoil protons were detected in the backward direction, and tritons were detected in the forward direction in the laboratory frame. Detecting one of the neutrons in a forward cone with the use of the DEMON neutron-detector array provided reconstruction of the full kinematics of the reaction. Note that the relatively wide angular range of proton detection in the laboratory frame corresponds to a rather narrow cone ( $< 7^\circ$ ) in the center-of-mass frame. This suggests that the kinematics in this reaction is close to that of 'zero geometry' (see Section 2.2). Indeed, quite pronounced correlation spectra were obtained in this experiment.

The  ${}^5\text{H}$  missing mass spectrum obtained in the experiment [133, 134] (Fig. 42) is almost shapeless. It monotonously increases with energy up to  $\approx 4$  MeV (its subsequent decrease is due to the effect of instrumental cutoff, i.e., efficiency), which appears to be related to a weak population of the  ${}^5\text{H}$  ground state  $1/2^+$ , and the separation of its contribution against the background of the high-energy state contribution becomes possible solely by means of correlation analysis.

An example of how the  ${}^5\text{H}$  ground-state contribution influences the correlation picture is given in Fig. 43. Though

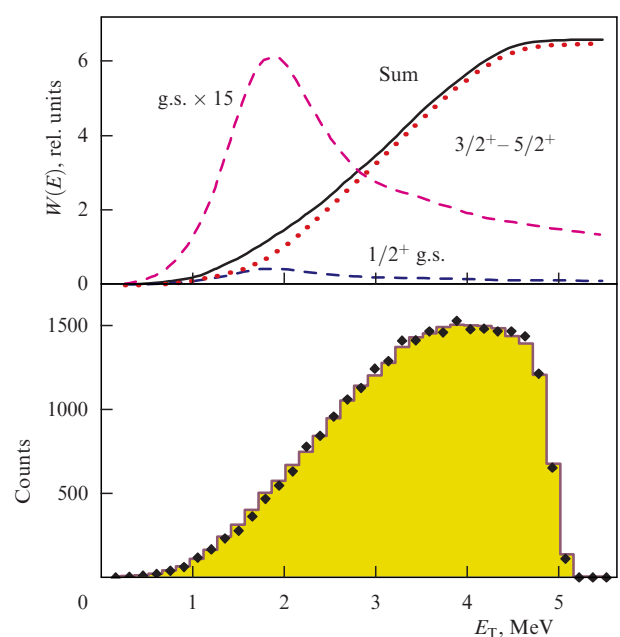


**Figure 42.** Spectrum of  ${}^5\text{H}$ ;  $W(E)$  is the population probability obtained for the  ${}^5\text{H}$  states (taken from Refs [133, 134]).



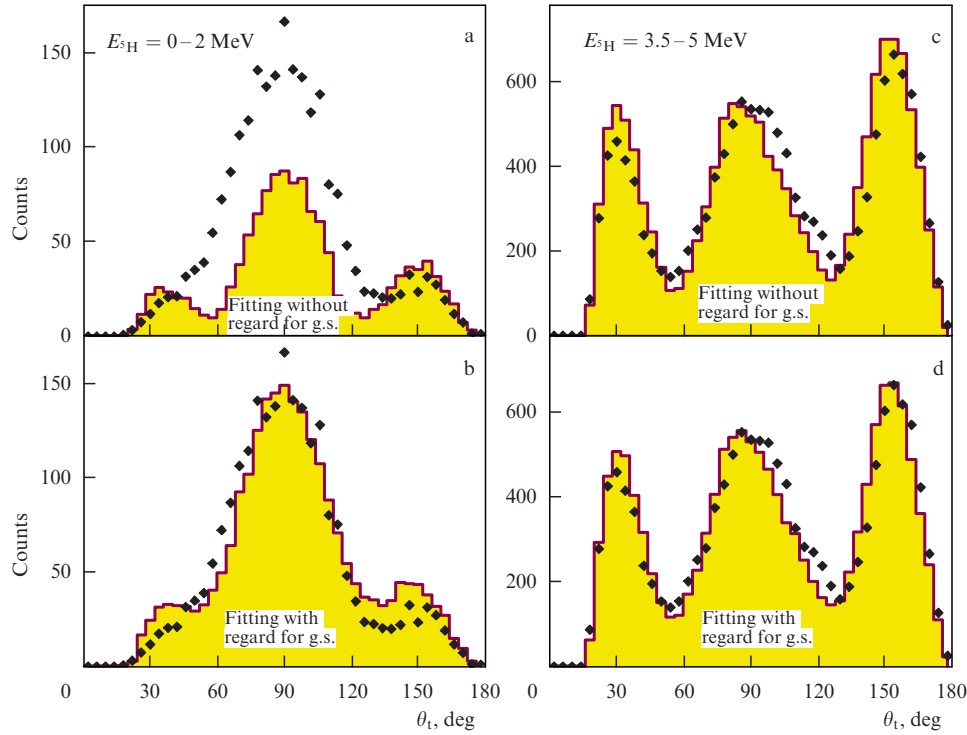


**Figure 43.** Angular distributions of tritium in the  ${}^5\text{H}$  center-of-mass frame related to the transferred momentum direction (taken from Ref. [134]).

the spectrum in Fig. 42 gives no chance for separation of the ground state, there can be no doubt that it manifests itself in correlations. Another result of correlation studies is the demonstration that the wide peak (tentatively at energy of about  $E_T \approx 4.5\text{--}5.0$  MeV), only the left wing of which we could observe, is a mixture of nearly degenerate states  $3/2^+$  and  $5/2^+$ —the doublet originating from coupling of the triton core spin with the  $2^+$  state of the valence nucleons.

The surprisingly small width of the  ${}^5\text{H}$  ground state obtained in Ref. [168] (see Fig. 40) has also found its explanation in paper [134]. Since the reaction products were detected in Ref. [168] in a narrow angular range, the observed peak was not a resonance peak of the ground state itself, but was a result of the interference of the ground state resonance with the higher-lying excited states. We managed to reproduce this effect for the data [134] obtained with a much larger acceptance, artificially applying desired geometrical cuts to the detector setup.

The situation with  ${}^5\text{H}$  indicates that the spin-parity identification capability may appear to be the key in the studies of continuum states in neutron-rich systems. These states usually turn out to be rather wide and overlapping. In different reactions, the populated states give rise to drastically different spectra, and under these conditions the excitation spectrum itself may contain insufficient information. Moreover, in registration within restricted angular ranges, the spectra can be distorted unrecognizably because of interference between the states with different  $J^\pi$ .

### 5.5 ${}^{10}\text{He}$ : the end of the shell magic

It was shown in Sections 5.3 and 5.4 how correlation measurements, specific for direct reactions at intermediate energies, make possible the reliable spin-parity identification for the states of two-particle and three-particle continuum spectra. In the considered experiments, analysis was based on data accumulated with quite high statistics. By the example of

the more complicated case with the  ${}^{10}\text{He}$  nucleus, we will show that such information can also be obtained for rather exotic systems populated with extremely low intensity.

For over half a century,  ${}^{10}\text{He}$  has been attracting the attention of both theorists and experimentalists, giving hope for getting unique, exceptional results. Expectations of such an outcome were born as a result of the direct expansion of the properties inherent to nuclei in the vicinity of the  $\beta$ -stability line to the  ${}^{10}\text{He}$  case. According to the shell model,  ${}^{10}\text{He}$  is the lightest (after  ${}^4\text{He}$ ) double magic nucleus. It was supposed that shell closure will lead to nuclear stability with respect to neutron emission or, in the case of instability, it will affect the energy position of the  ${}^{10}\text{He}$  ground state and its width. Interest in this issue was enhanced by the fact that  ${}^{10}\text{He}$  is characterized by extremely high neutron  $N/Z$  ratio.

${}^{10}\text{He}$  was discovered in 1994 by A. Korshennikov and colleagues [171]. It was observed as a quite wide resonance ( $\Gamma \sim 1.2$  MeV) at  $E_T = 1.2(3)$  MeV above the two-neutron emission threshold. Soon after the discovery of  ${}^{10}\text{He}$ , one doubtful feature in its spectrum was reported [172] as being the narrow (0.3 MeV) ground state with an energy of about 1 MeV. Though only wide states with the energy of 1–1.5 MeV were reported for  ${}^6\text{He}$  later in Refs [165, 173, 174], a quite popular opinion has been established that all the results are in good agreement. Notice that in Refs [165, 171, 173, 174]  ${}^{10}\text{He}$  was produced in the reactions of the proton knock-out from  ${}^{11}\text{Li}$ , and  $\alpha$  removal from  ${}^{14}\text{Be}$ . It turned out that another interpretation related to the reaction mechanism is possible for these types of  ${}^{10}\text{He}$  spectrum population [92, 108].

In our experiments [136, 137], the  ${}^{10}\text{He}$  nucleus was obtained in the reaction of two-neutron transfer from triton to the  ${}^8\text{He}$  bombarding nucleus. The registration system was analogous to that used in experiments studying  ${}^5\text{H}$  [134] and  ${}^9\text{He}$  [135]. Tritium gas cooled to a temperature of 26 K was bombarded by  ${}^8\text{He}$  ions with an energy of 21.5 MeV per nucleon. The recoil protons emitted in the direction opposite

to the beam direction were detected by an annular silicon detector installed in front of the target.  $^8\text{He}$ , which is the product of the  $^{10}\text{He}$  decay, was detected by a square telescope placed behind the target. More detailed information on the detector array can be found in paper [137].

Experiment [136] gave surprising results. The statistics in this experiment appeared to be insufficient for  $^{10}\text{He}$  ground-state energy identification, but quite enough to make the statement that the ground state did not appear at  $E_T \sim 1.2$  MeV but is situated somewhere higher. The next experiment [137] allowed this statement to be verified and the  $^{10}\text{He}$  ground state energy to be determined:  $E_T \approx 2.2(2)$  MeV. The discrepancy with preceding data obtained its explanation in papers [92, 108]. When  $^{10}\text{He}$  is produced in the removal reactions, the drip-line halo nuclei are used as the projectiles. The valence nucleons of the halo have narrow momentum distributions. The  $^{10}\text{He}$  nucleus were a long-lived resonance, this could not affect its observed spectrum. However, the width of the  $^{10}\text{He}$  ground state,  $\Gamma > 1$  MeV, is quite large. During the decay, there is not enough time to melt the memory of initial configurations of the valence nucleons, and this induces a shift of the whole spectrum towards the lower energy. In this context, the results of Refs [136, 137] reexamine the  $^{10}\text{He}$  ground state energy and add important caution concerning the study of nuclear systems beyond the stability border with the use of removal reactions at high energies.

In the measurements taken in Ref. [137], angular and energy correlations between the  $^{10}\text{He}$  decay products were obtained. In the analysis of the data, assumptions were made similar to those discussed in Section 2.2, namely, (i) the  $^{10}\text{He}$  orbital momentum is aligned with the transferred momentum  $\mathbf{q}$ ; (ii) the total dineutron spin  $S$  is equal to zero, and (iii) the emitted neutrons interact in the final state. The last condition corresponds to a small value of parameter  $\varepsilon = E_{nn}/E_T$ .

In Fig. 44, the  $^{10}\text{He}$  missing mass spectrum [137] obtained in the coincidence of the proton with  $^8\text{He}$  is shown. Experimental data are marked by dots with error bars, the grey histogram corresponds to events satisfying the condition of  $\varepsilon < 0.5$ . In both spectra, a wide peak with a maximum at the energy of about 2 MeV is clearly seen. At higher energies, the spectrum becomes smooth; there are no peculiarities that could prompt one to argue about the population of the  $^{10}\text{He}$  excited states.

At the same time, in the  $^{10}\text{He}$  missing mass spectrum one can find three ranges, each of them characterized by strongly pronounced angular and energy correlations. In Fig. 45, the  $^8\text{He}$  angular distributions are plotted in the center-of-mass

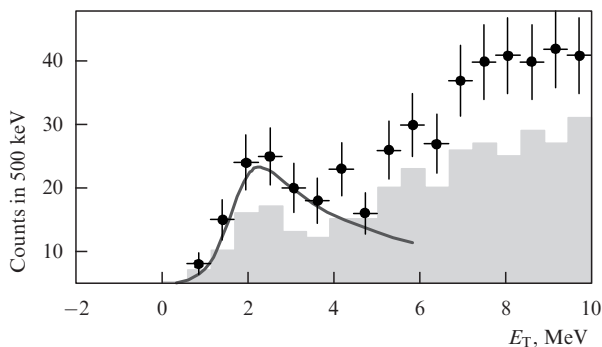


Figure 44.  $^{10}\text{He}$  missing mass spectrum (see text for details).

(CM) frame of  $^{10}\text{He}$  with respect to the  $\mathbf{q}$  direction, obtained under conditions that events with  $\varepsilon < 0.5$  are selected. These distributions agree well with the assumption that, at small values of  $\varepsilon$ , the  $^{10}\text{He}$  quasibinary decay into spinless particles occurs. The  $^8\text{He}$  angular distributions obey a simple formula represented by a coherent sum of three Legendre polynomials:

$$w = (AP_0(x) + B\sqrt{3}P_1(x) + C\sqrt{5}P_2(x))^2 + D^2, \quad (36)$$

where fitting parameters  $A$ ,  $B$ , and  $C$  are the amplitudes of the WF components containing the s-, p-, and d-waves, and amplitude  $D$  serves to take into account the total contribution from the  $^{10}\text{He}$  states which are incoherently summed.

The homogeneous angular distribution for  $E_T < 3.5$  MeV points to the fact that, at this energy range, the  $^{10}\text{He}$  ground state with the spin and parity  $J^\pi = 0^+$  dominates. The result of identification of two excited states turned out to be unexpected, i.e., the  $1^-$  state in the energy range  $4.5 < E_T < 6$  MeV, and the  $2^+$  state occurring at  $E_T > 6$  MeV, though for nuclei with closed shells/subshells typical is the opposite situation, when the first excited state has the spin-parity  $J^\pi = 2^+$ . This result reminds that  $^{10}\text{He}$  is one more example of breaking normal regularities in filling up the nuclear shells at the drip line, and confirms the evidence of this phenomenon obtained earlier for such nuclei as  $^{12}\text{Be}$  [175]. A popular review of this topic is also given in monograph [6].

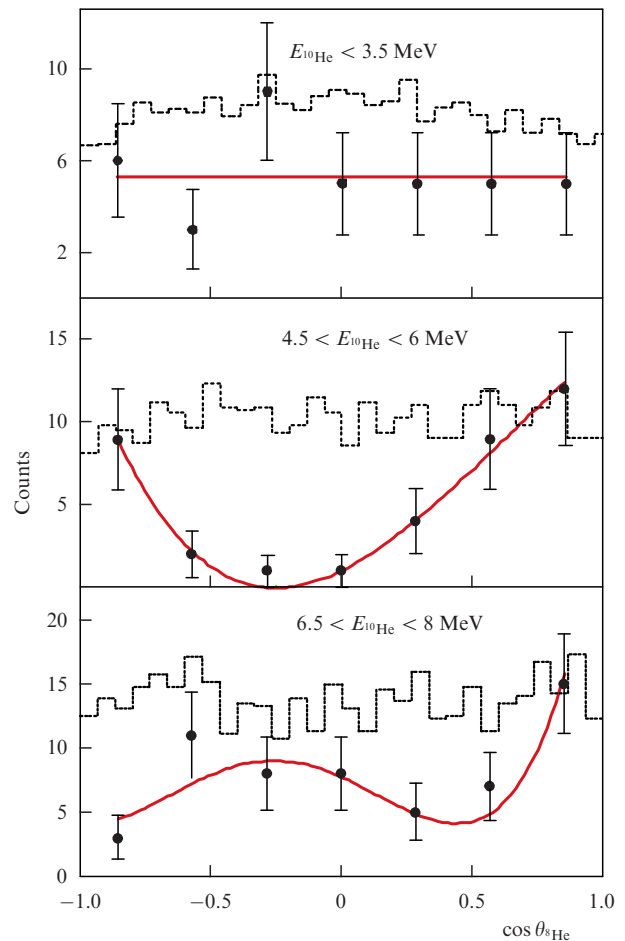


Figure 45.  $^8\text{He}$  angular distributions in the  $^{10}\text{He}$  center-of-mass frame with respect to the transferred momentum  $\mathbf{q}$  direction in different energy ranges of  $^{10}\text{He}$ . Histograms show the detection efficiency.

### 5.6 ${}^6\text{Be}$ : isovector soft dipole mode

The study of correlations in the  ${}^6\text{Be}$  nucleus decay, carried out in the 1970s–1980s, led to the formulation of the ‘*democratic decay*’ concept (see Section 3.5). However, there followed a period of ‘oblivion’ continuing almost 20 years. During these years, experimental techniques were significantly developed. The study of  ${}^6\text{Be}$  decays at a new technical level was continued in work [46, 63]. Notice that the results on  ${}^6\text{Be}$  obtained in these studies appeared to be a byproduct of the  ${}^{10}\text{Be}(p, n){}^{10}\text{C}$  reaction studies. Analyzing the decay channel of the  ${}^{10}\text{C}$  excited states into four fragments  $2\alpha-2p$ , it turned out that the decay proceeds with the dominating population of the  ${}^6\text{Be}$  ground state  $0^+$  due to the final state interactions. In papers [46, 63], interesting results on the  ${}^6\text{Be}$  structure and the dynamics of three-particle decay have been obtained. In general, the data in work [46] were obtained by chance in a narrow energy window (the ground state was populated alone); however, it became clear that we must return to a more detailed and dedicated investigation of this nucleus.

The first attempt was not successful. The environmental conditions around experiment [176] dramatically distorted the spectra. The low quality of MC simulations did not allow one to consider these distortions correctly (see the discussion of simulations in Section 2.3). The group at the ACCULINNA facility decided to take part in a ‘scientific competition’ by studying  ${}^6\text{Be}$  in the charge-exchange reaction  ${}^1\text{H}({}^6\text{Li}, {}^6\text{Be})n$ . It should be noted that almost simultaneously with our findings, the results of  ${}^6\text{Be}$  studies on the reaction of proton removal from  ${}^7\text{Be}$  at NSCL were also published. In this work, the decay dynamics of the  ${}^6\text{Be}$  states at quite high excitation energies up to  $E_T \sim 15$  MeV was investigated in detail. In particular, it was established that in  ${}^6\text{Be}$ , against all expectations, no transition from the three-particle decay mechanism to a purely sequential one occurs, even for large decay energies  $E_T \sim 10$  MeV [47].

The experimental setup used in study [101] is schematically shown in Fig. 46. In the experiment, a beam of  ${}^6\text{Li}$  stable nuclei was produced, thus making it possible to give up the event-by-event identification of all ingoing particles and exploit the ACCULINNA facility in the monochromatization regime to enhance the primary beam quality. The  ${}^6\text{Li}$  charge exchange proceeds on the cryogenic hydrogen target. The neutrons created in the charge exchange process are emitted in a wide angular range in the backward direction, which makes impossible their effective registration. The full kinematics of the reaction is retrieved from the triple

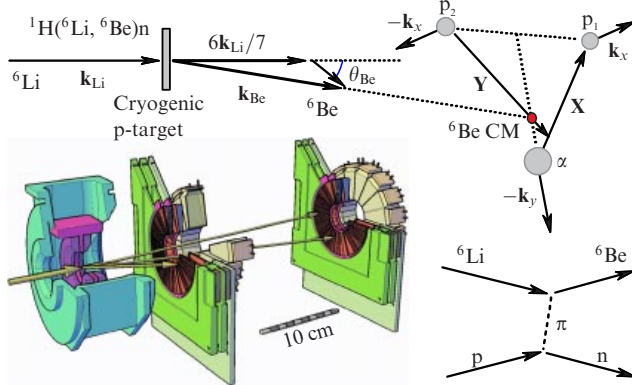


**Figure 46.** Layout of experiment [101] on  ${}^6\text{Be}$  in the charge-exchange reaction  ${}^1\text{H}({}^6\text{Li}, {}^6\text{Be})n$ .

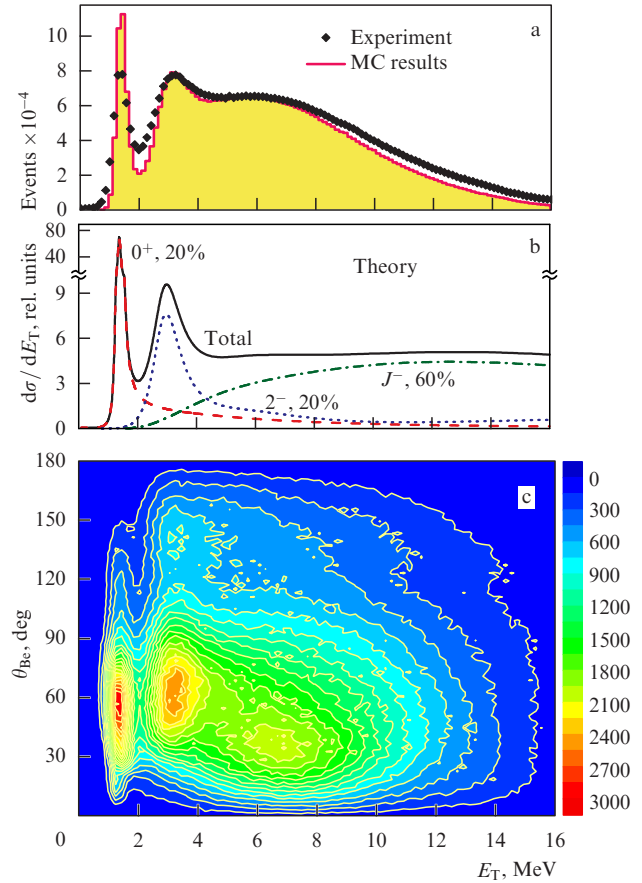


**Figure 47.** (Color online.) (a) The  ${}^6\text{Be}$  spectrum obtained in experiment [101] and the results of MC simulations. (b) Results of theoretical calculations used as input data for MC simulations. (c) The number of  ${}^6\text{Be}$  events obtained in the full range of angles in the center-of-mass frame of the reaction versus the energy  $E_T$  in the  ${}^6\text{Be}$  system.

coincidence ( $\alpha-p-p$ ). Two sequential annular telescopes covered the angular ranges of  $3^\circ-8^\circ$  and  $10^\circ-24^\circ$ , thus allowing the  ${}^6\text{Be}$  invariant mass to be reconstructed in a wide energy range (0.7–15 MeV).

The results of the  ${}^6\text{Be}$  investigation at the ACCULINNA facility are comparable in their quality with the results reported in paper [47], but they were used for physical conclusions in other field. The main qualitative result was the comprehension of the importance of the unique ensemble of the reaction mechanism and the dynamics in the continuum spectrum, characterized in Ref. [101] as the *isovector soft dipole mode* (IVSDM). It can be seen in Fig. 47 that, besides the well-known resonant  $0^+$  and  $2^+$  states of  ${}^6\text{Be}$ , the region of  $E_T > 4$  MeV is also intensively populated. It is found that the total intensity of its population is about three times more than that for low-lying resonant states, which seemingly should make the major contribution to the reaction cross section. In earlier studies [177, 178], this question was not posed, and the spectrum of  $E_T > 4$  MeV was approximated by the phase volume. Few versions related to both hypothetical states of  ${}^6\text{Be}$  and different reaction mechanisms are considered in works [179–181] (see discussion in paper [101]). The high quality of the data in Ref. [101] sheds light on this question, suggesting a consistent explanation of the spectrum in the region  $E_T > 4$  MeV (see Fig. 47) as a manifestation of IVSDM. In contrast to SDM, this mode is not based on the ground state of the nucleus (the  ${}^6\text{Be}$  ground

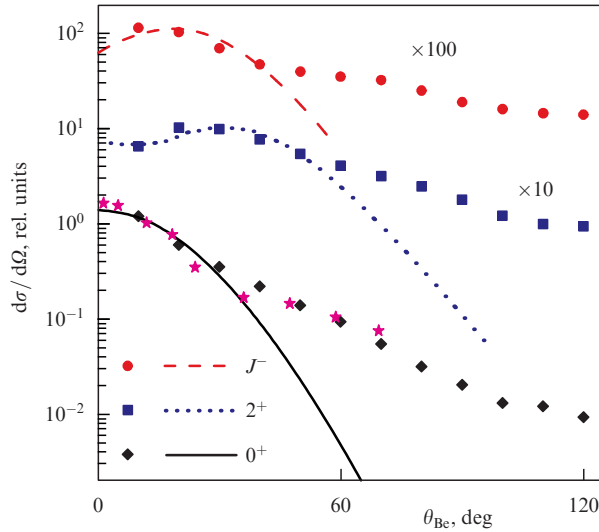


**Figure 48.** Angular distributions in the center-of-mass frame of the reaction for different states of  ${}^6\text{Be}$  in comparison with the calculations made in PWIA. The angular distribution for the  $0^+$  state from Ref. [177] is also given (stars), as obtained in similar experimental conditions.

state is a short-lived resonance); IVSDM is based on the spatially extended configuration of the  ${}^6\text{Li}$  parent nucleus in the isospin channel. It is clearly seen in Fig. 47b that the maximum in the  ${}^6\text{Be}$  angular distribution for  $E_T > 4$  MeV is placed at angles less than the maximum for the  $2^+$  state. In this figure, the maximum for the  $0^+$  state is not informative, since it is determined by the setup efficiency. Detailed MC simulations (see Section 2.3) allow finding that the IVSDM maximum is placed between peaks for the  $0^+$  and  $2^+$  states, as was predicted for  $\Delta L = 1$ , i.e., for negative parity structures (Fig. 48).

In this example, the feature of the *nuclear excitation modes* brilliantly manifests itself. For certain reaction mechanisms they provide more intensive population than *resonant processes*. From the viewpoint of methodology we see how the correlation measurements carried out with high statistics allow one to solve the problem which were not accessible before.

### 5.7 ${}^8\text{He}$ : $2^+$ state and soft dipole mode

Along with  ${}^6\text{He}$ , the  ${}^8\text{He}$  nucleus is assigned to classical halo nuclei.  ${}^8\text{He}$  itself has been known for more than 50 years, since 1965. This nucleus is a Borromean system in respect to  ${}^6\text{He}$ , with the two-neutron separation energy  $S_{2n} = 2.14$  MeV. However, the valence nucleons in  ${}^6\text{He}$  are more weakly bound,  $S_{2n} = 0.973$  MeV. As a result,  ${}^8\text{He}$  consists of five  ${}^4\text{He}-n-n-n$  clusters (four-nucleon halo), instead of three,  ${}^6\text{He}-n-n$ , and its root-mean-square radius is less than that in  ${}^6\text{He}$  (see Fig. 9). Seemingly, this nucleus should be well studied. However, if we turn to standard compilation [182], we find that the energy of the first excited  $2^+$  state is presented with a significant uncertainty ranging 2.7–3.6 MeV.

The source of this problem was identified in Ref. [136] discussed earlier in Section 5.5. The following interpretation of the low-lying  ${}^8\text{He}$  spectrum has been proposed in Ref. [136]. The  $2^+$  state resides in  ${}^8\text{He}$  at the excitation energy  $E^* = 3.6\text{--}3.9$  MeV (corresponding to  $E_T = 1.5\text{--}1.8$  MeV with respect to the  $2n$ -threshold). Such relatively high quadrupole excitation energy agrees satisfactorily with the fact that the  ${}^8\text{He}$  nucleus possesses closed  $p_{3/2}$  subshell. And

the lowest-lying excitation in the  ${}^8\text{He}$  spectrum represents the  $1^-$  SDM state. Theoretically predicted SDM spectrum in  ${}^8\text{He}$  is moderately wide with a peak at  $E^* \sim 3$  MeV ( $E_T \sim 0.9$  MeV). Because the SDM is very sensitive to the reaction mechanism, it is differently populated in various reactions. If such a combination of states is fitted by one peak, the result will demonstrate a strong variation in passing from one experiment to the other. Figure 49 demonstrates data from Refs [136, 161, 183, 184], which point to the presence of low-energy events on the left slope of an expected  $2^+$  peak.

Theoretical explanation of this situation may be found in Ref. [185]. The general expectation concerning the SDM origin is that it is a totally geometric effect (see Fig. 13). It stems from this interpretation that the larger the radius of the ground state, the lower the energy of the SDM peak. In  ${}^6\text{He}$ , the SDM peak is predicted and observed at the energy  $E_T \sim 1.1\text{--}1.4$  MeV. Since  ${}^8\text{He}$  is bound with respect to the  $2n$ -threshold much more strongly than  ${}^6\text{He}$  ( $E_b = 2.14$  MeV compared to  $E_b = 0.97$  MeV), and its wave function is much more compact, then following this logic the expected position of the SDM peak in  ${}^8\text{He}$  should be at  $E_T \sim 2$  MeV. This was the starting point for the authors of Refs [183, 184], when they assigned the alternation of states to be  $0^+$ ,  $2^+$ ,  $1^-$  in the low-energy spectrum of  ${}^8\text{He}$ . It was also demanded that the  $2^+$  state have abnormally low energy  $E^* = 2.9$  MeV.

It is shown in Ref. [185] that, besides the geometry of the ground state, there is one more effect qualitatively affecting the shape of the SDM spectrum in the three-particle systems.

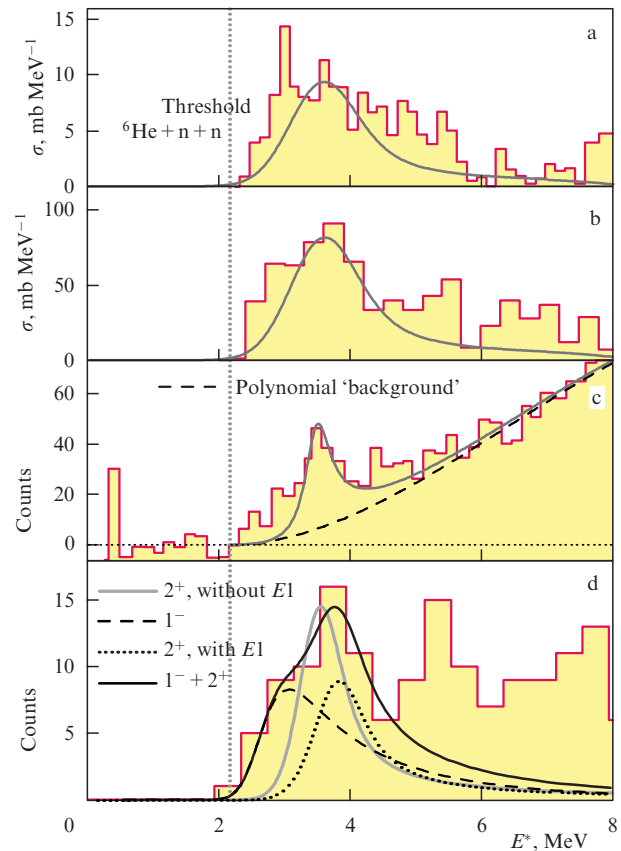


**Figure 49.** (Color online.) Experimental data on the first excited  $2^+$  state of  ${}^8\text{He}$ : (a) [183], (b) [184], (c) [161], and (d) [136]. In panel d, the results of fitting the low-energy part of the spectrum are given. The fit is obtained supposing either the  $2^+$  state is pure or this is a mixture of  $2^+$  and  $1^-$  SDM ( $E1$  excitation).



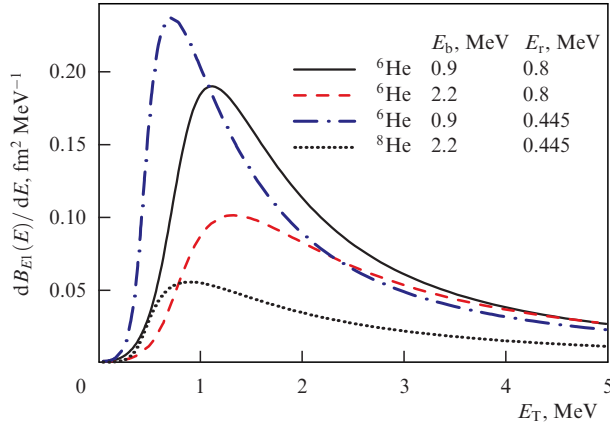


**Figure 50.** Dependence of the SDM spectrum for three-particles systems on the binding energy  $E_b$  of an initial system and the ground-state energy  $E_r$  of the core- $n$  subsystem.

This effect is connected with the SDM dependence on the final-state interaction. For the two-body case of the soft dipole mode, the final state is always nonresonant, as it always belongs to another shell, while the SDM features in the three-body case are always determined by a mixture of resonant and nonresonant dynamics (see Fig. 14). It was shown by the use of simplified semianalytical methods that, due to the dependence of the core- $n$  subsystem on the ground state energy  $E_r$ , the SDM spectrum can be shifted toward low energies (Fig. 50). The answer is that, for  ${}^8\text{He}$ , the ground state energy in the  ${}^7\text{He}$  subsystem,  $E_r = 0.445$  MeV, is much less than that in the  ${}^5\text{He}$  subsystem for  ${}^6\text{He}$  ( $E_r = 0.9$  MeV). Thus, two trends act upon the SDM in the transition from  ${}^6\text{He}$  to  ${}^8\text{He}$ : the energy of the SDM peak increases with the WF radius, and this energy lowers with a decrease in  $E_r$ . Calculations bring out that a critical role belongs to the final state interaction, and a very unusual situation arises for even-even light nuclei when the first excited state has negative parity.

### 5.8 ${}^7\text{H}$ and the 4n-decay problem

One may say that the  ${}^7\text{H}$  system constitutes the golden fleece for physicists studying light nuclei.  ${}^7\text{H}$  has the maximum neutron excess which can be imagined. Thus, the neutron-to-proton ratio amounts to 6/1. The prospects for the search for this nucleus as a narrow low-lying resonance and its importance for the nuclear structure theory were justified by Ya B Zel'dovich [77] at the end of 1950s. However, after more than half a century this problem remains unresolved.

Indications that the  ${}^7\text{H}$  ground state resides above the  ${}^3\text{H}$ -4n threshold were obtained in the  ${}^8\text{He}(p, 2p)$  and  ${}^{11}\text{Be}(\pi^-, p^3\text{He})$  reactions reported in Refs [186, 187]. In neither case did the low experimental resolution ( $> 1$  MeV) and bad background conditions allow a quantitative statement about the  ${}^7\text{H}$  properties. The discovery of  ${}^7\text{H}$  was declared by Caamaño et al. [188] for the  ${}^{12}\text{C}({}^8\text{He}, {}^{13}\text{N})$  reaction. However, a close examination of their detailed paper [189] shows that identification of a final state in these studies is actually absent, and observed events can refer to other hydrogen isotopes with other energies.

At present, paper [190] has put some multiple points after the history of the  ${}^7\text{H}$  search. The authors examined reaction  ${}^2\text{H}({}^8\text{He}, {}^3\text{He})$ , which is more advantageous than  ${}^{12}\text{C}({}^8\text{He}, {}^{13}\text{N})$ , utilized in Ref. [188], and it should have a significantly larger cross section. However, with a much

higher beam integral than that in Refs [188, 189], the authors of Ref. [190] could not disclose the ground state of  ${}^7\text{H}$ . Obviously, further search for  ${}^7\text{H}$  calls for serious steps: either new methods are needed or a significant expansion of statistics on reactions already studied with a simultaneous resolution enhancement is required.

In experiment [122] at the ACCULINNA facility, we managed to obtain a unique but informative result regarding  ${}^7\text{H}$ . In this research, a hypothesis for the possibility of existing the long-lived resonance in a system decaying with simultaneous emission of four neutrons (see Section 3.8) was tested. For  ${}^7\text{H}$  production, the reaction  ${}^2\text{H}({}^8\text{He}, {}^3\text{He})$  was utilized. The cryogenic target cell with liquid deuterium was very thick—56 mm—to absorb completely (with 100% assurance) the  ${}^8\text{He}$  beam with the energy of 20.5 MeV per nucleon. In this reaction, the  ${}^7\text{H}$  nucleus is predominantly emitted in the forward direction, and in the case of population of a long-lived state (hundreds of picoseconds or longer), it passes through the remaining thickness of the target relatively freely due to fewer ionization losses than those for the  ${}^8\text{He}$  beam. In this experiment, no  ${}^7\text{H}$  events were revealed. This fact put restrictions on two quantities, i.e., on the lifetime of the  ${}^7\text{H}$  ground state, and on its population cross section. In Ref. [122], theoretical estimates of the lifetimes of long-lived 4n-emitters have been performed for the first time (see also paper [24] and Fig. 24). In Ref. [122], the lower bound of the  ${}^7\text{H}$  decay energy in the  ${}^3\text{H}$ -4n channel was estimated with the use of systematics of the  $(d, {}^3\text{He})$  reaction cross sections as 50–100 keV.

### 5.9 ${}^{17}\text{Ne}$ for astrophysics

The  ${}^{17}\text{Ne}$  nucleus located at the proton drip line is interesting for several reasons. The unusual structure of this nucleus is related to low-lying single-particle proton orbitals  $2s_{1/2}$  and  $1d_{5/2}$  in a continuum spectrum. The presence of weakly bound valence protons and close continuum states with opposite parity creates prerequisites for appearing the soft dipole mode of excitation, which assumes a dipole strength concentration near the threshold. As shown in Ref. [191], this phenomenon can exhibit either resonant or nonresonant behavior, which requires experimental verification.

The first excited state,  $J^\pi = 3/2^-$ , with the energy of 1288 keV is of special interest here. This energy exceeds the two-proton decay  ${}^{17}\text{Ne} \rightarrow {}^{15}\text{O} + 2p$  threshold by only 344 keV and the channel of the one-proton decay is energetically prohibited. In other words, the first excited state is a candidate for a true two-proton emitter, when this decay branch can compete with  $\gamma$  decay to the  ${}^{17}\text{Ne}$  nucleus ground state. The decay mode of the first excited state of  ${}^{17}\text{Ne}$  is also interesting from astrophysical point of view.

First of all, determination of the 2p-decay width of the  ${}^{17}\text{Ne}$  first excited state  $3/2^-$  is of interest for the theory analyzing the dynamics of this process (see, for example, Refs [71, 90, 91, 95, 96, 192]). This problem is probably also important for the nucleosynthesis theory. The daughter  ${}^{15}\text{O}$  nucleus produced in the 2p-decay of the  $3/2^-$  state of  ${}^{17}\text{Ne}$  is the waiting point for the CNO cycle of nucleosynthesis in a hot and dense stellar substance. The reaction  ${}^{15}\text{O}(2p, \gamma){}^{17}\text{Ne}$  was considered by the authors of paper [96] as a possible bypass of this point. In Ref. [95], it was shown that the width of the  ${}^{17}\text{Ne}$   $3/2^-$  state is a critical value for the probability of 2p-pickup by the  ${}^{15}\text{O}$  nucleus in the CNO cycle. In Ref. [90], a conservative estimation of the 2p-decay partial width of the  $3/2^-$  state in  ${}^{17}\text{Ne}$  was given:  $\Gamma_{2p} \sim 5 \times 10^{-14}$  MeV. It was

supposed that the analogous estimate in paper [192] is inaccurate, giving for the partial width values 1000 times larger. A series of attempts to search for a weak branch of the 2p-decay of the  $3/2^-$  state in  $^{17}\text{Ne}$  was made, which put the upper bound for  $\Gamma_{2p} < 2.5 \times 10^{-11}$  MeV [193, 194].

The method [130] has been developed and realized at the ACCULINNA facility, allowing a substantial increase in the sensitivity of the experiment and, thus, either finding the rare branch of decay or lowering the bound for the 2p-decay partial width of  $^{17}\text{Ne}$  from the previously stated value to  $\Gamma_{2p} \leq 1 \times 10^{-13}$  MeV. In the long term, this bound is comparable to the estimation of  $\Gamma_{2p} \sim 5 \times 10^{-14}$  MeV performed in Ref. [95] and can be 250 times as low as the bound reached in Ref. [194].

The reaction  $^1\text{H}(^{18}\text{Ne}, d)^{17}\text{Ne}$  at the energy  $E(^{18}\text{Ne}) = 34.5$  MeV per nucleon [130] was chosen because the cross sections of the ground ( $1/2^-$ ) and the first excited ( $3/2^-$ ) state populations are maximum in the neutron pick-up reaction, as the neutrons are picked up from corresponding shells. The population of higher states ( $5/2^-$ , 1764 keV and  $1/2^+$ , 1908 keV) is realized with the aid of at least the two-step mechanism; thus, the cross sections are expected to be much less. The kinematics of this reaction is very convenient for application of the so-called combined mass method, i.e., for determining the energy and trajectory angle of the emitted deuteron and two protons. However, the two-proton decay of the first excited state may compete with dominating  $\gamma$  decay to the ground state. The doublet of higher-lying states decays with a 100% probability with the emission of two protons. This might be either sequential decay through an intermediate state of the  $^{16}\text{F}$  nucleus or direct decay to the  $^{15}\text{O}$  ground state. As the energies of these protons are close to those from the decay of the first excited state, this imposes constraints on the energy resolution and background conditions in the experiment.

The results of the experiment, which consists of two steps, are given in Fig. 51. At the first step, the cross sections of the  $^{17}\text{Ne}$  ground and first excited state populations are measured using the missing mass method with a thin hydrogen target. The energy resolution of the deuteron registration in the silicon annular telescope in the angular range of  $5^\circ - 10^\circ$  is

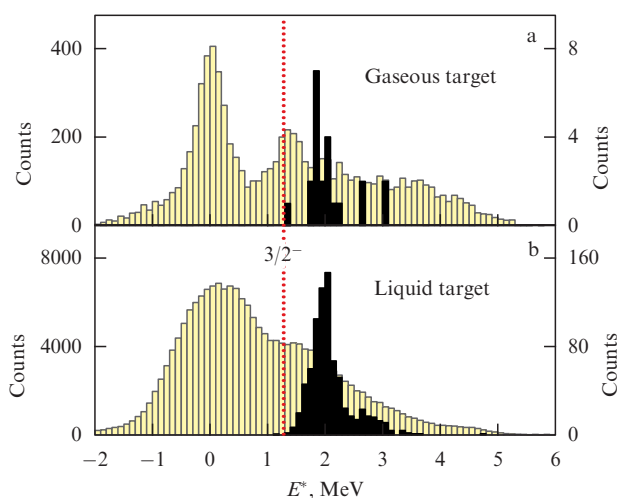


**Figure 51.** Spectra in the missing mass (light colored histogram, left scale) and combined mass (black histogram, right scale) methods for the  $^{17}\text{Ne}$  population in the reaction  $^1\text{H}(^{18}\text{Ne}, d)$  on thin (a) and thick (b) targets. The vertical dashed straight line shows the  $3/2^-$  state energy.

350 keV (FWHM), which makes possible unambiguous identification of all the states. In order to search for the two-proton decay of the  $^{17}\text{Ne}$  first excited state, the deuterons detected by the annular telescope are selected, which coincided with protons detected by the square telescope placed on the beam axis. For better statistics, the thickness of the hydrogen target was increased several times, while the resulting resolution remained relatively high (FWHM better than 300 keV), since providing coincidence of deuteron with two protons corresponds to the condition of the full kinematic experiment. A major part of the events in the combined mass spectrum is related to population and decay of the doublet of states  $5/2^-$  (1764 keV) and  $1/2^+$  (1908 keV). In the most interesting part of the spectrum,  $\approx 1300$  keV, three events were found which can be designated as both the first excited state decay and the background (the second proton could be produced as the result of the  $^{15}\text{O}$  nucleus interaction with the substance of the filter placed just in front of the square telescope). Under the assumption that one of the events belongs to the background, the new upper bound for the ratio  $\Gamma_{2p}/\Gamma_\gamma < 1.3 \times 10^{-4}$  was stated from the data analysis, being 30 less than that obtained in Ref. [194].

An important result of these measurements is affirmation of the promising outlook of the method. A further 50-fold or more reduction is assumed to be quite realizable with the ACCULINNA-2 facility, where the background will be suppressed by the use of a zero-angle spectrometer (see Section 6.1).

### 5.10 Search for $^{26}\text{S}$

The search for new isotopes in the region of light nuclei is usually conducted at facilities much more powerful than ACCULINNA. However, in the domain from magnesium up to argon there is a gap which has only recently started to fill up. This allowed performing a search experiment to detect the proton-rich  $^{26}\text{S}$  isotope. According to the National Brookhaven Laboratory database [1], it was accepted till 2011 that the  $^{26}\text{S}$  lifetime should be a few microseconds, and information on the mass excess and possible decay channels of the ground state of this nuclide was entirely absent. Based on the systematics, one could expect that the  $^{26}\text{S}$  isotope is a long-lived two-proton emitter. After experiments performed at the ACCULINNA facility and detailed analysis of data [94], the resulting table on  $^{26}\text{S}$  properties took on a new form (Table 3).

The experimental methodology includes registration of all fragments produced in the reaction  $^{32}\text{S}$  (50.3 MeV per nucleon) + Be (92.4 mg  $\text{cm}^{-2}$ ) and selection of  $^{26}\text{S}$  through the use of the regime of optimum transmission of nuclei with a certain ratio  $A^{5/2}/Z^{3/2}$  to the focal plane F4. The calculated time-of-flight of the  $^{26}\text{S}$  isotope on the flight path F1–F4 with regard for the energy losses in the target, wedge (Be, 92.4 mg  $\text{cm}^{-2}$ ), and ToF plastics was about 314 ns. This is four orders of magnitude less than the  $^{26}\text{S}$  lifetime from NNDC (National Nuclear Data Center) before 2011. Fragment identification was performed by means of  $(\Delta E - E)$  measurements using a silicon telescope and time-of-flight measurements on the straight-line flight path F3–F4.

**Table 3.** Current information on  $^{26}\text{S}$  states from the BNL database [1].

$E$	$J^\pi$	$A$ , MeV	$T_{1/2}$	Decay channel
0	$0^+$	27.0790 (syst.)	$< 79$ ns	2p

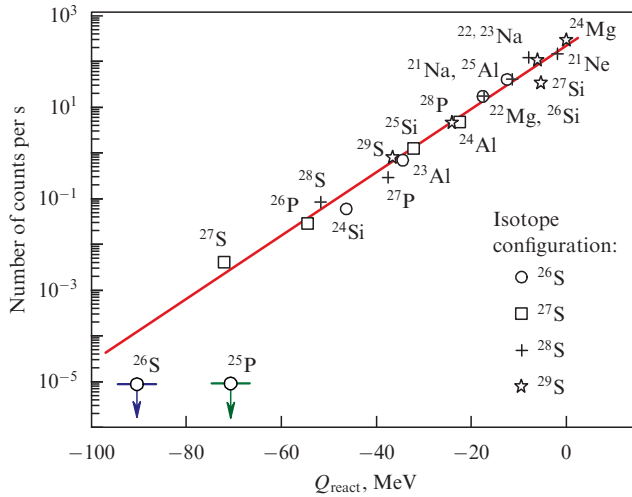


**Figure 52.** Systematics of yields of the fragmentation reaction for various nuclei as a function of the reaction energy release  $Q_{\text{react}}$ .

To get information on the  $^{26}\text{S}$  lifetime, the separator was sequentially tuned to give the optimum transmission of known  $^{29}\text{S}$ ,  $^{28}\text{S}$ , and  $^{27}\text{S}$  isotopes in order to measure yields of these nuclei and satellite isotopes with similar values of the parameter  $A^{5/2}/Z^{3/2}$  and to obtain the  $Q_{\text{react}}$  dependence of the nucleus yields. Extrapolation of this systematics (Fig. 52) to the region of  $^{26}\text{S}$  and  $^{25}\text{P}$  (according to data [195], the limit is  $T_{1/2} < 30$  ns) pointed to the expected number of events of  $\sim 16$  and  $\sim 360$ , respectively. In the experiment, no one event satisfying the certain isotope detection was found. Using the Poisson distributions with a 63% level of confidence for single-event registration, a new bound for the  $^{26}\text{S}$  half-life period was established,  $T_{1/2} < 79$  ns, while that for  $^{25}\text{P}$  was  $T_{1/2} < 38$  ns, which is in good agreement with available data.

A theoretical analysis of the properties of the  $^{26}\text{S}$  nucleus and its  $^{24}\text{Si}$ ,  $^{25}\text{P}$  subsystem was done in the RMF (relativistic mean field) approximation. The method suggested in Refs [58, 61, 120] has been further developed; in three-body decay calculations, the many-body structure has been taken into account. The results of these calculations allowed 2p-decay probability estimates for  $^{26}\text{S}$ . The combined analysis of theoretical and experimental data allowed the bound for a two-proton decay energy to be established at  $Q_{2p} > 640$  keV. Under the assumption that the main branch of the  $^{26}\text{S}$  decay is one-proton emission, the lower bound for this nuclear decay energy is  $Q_{2p} > 230$  keV. A similar analysis for the  $^{25}\text{P}$  system led to the bound  $Q_p > 110$  keV.

For continued experimental investigation of the properties of  $^{26}\text{S}$ , a technique is needed allowing us to extend the  $T_{1/2}$  range to a few picoseconds. One such technique can be based on decay in-flight measurements (see paper [9] and Section 6.3), which is most effective at high RIB energies ( $E/A > 200$  MeV per nucleon). Another approach can be based on transfer reaction studies, for example,  $p(^{28}\text{S}, t)^{26}\text{S}$  at energies  $E(^{28}\text{S}) > 40$  MeV per nucleon with the registration of all products in the exit channel. This experiment is on the list of primary ones at the ACCULINNA-2 facility (see Section 6.1).

## 6. Implemented and prospective projects

Some projects presented below are in the process of realization, their implementation going according to plan and the start of their operation is only a matter of time. Other projects are considered rather as realizable in the long term. Their implementation requires considerable funding and the involvement of qualified specialists. We hope that the content of this section, showing the real scientific potential in the field of RIB studies in our country, will serve to stimulate the discussion of long-term development in this area.

### 6.1 ACCULINNA-2

The rationale and aim of building the new fragment separator at FLNR, JINR was outlined in preprint [3] in 2008, where the results of ion-optics calculations and the facility layout in the U-400M cyclotron hall are presented. The technical tasks to carry out the work were prepared based on this document and the search for the manufacturer began. A contract with the French company SigmaPhi [196] on the overall manufacturing of equipment (all magnets with power supplies and a vacuum system), installation, and putting it into operation was finally signed in 2011. The facility was completely built at the beginning of 2015, and the technical startup took place in summer 2015. Based on test results, it was certified that the technical characteristics of the magnet elements correspond to the values laid out in the project [197].

A layout of the ACCULINNA-2 facility in the building of the U-400M cyclotron is shown in Fig. 53a, and photos of the facility elements inside the cyclotron chamber during installation are displayed in Fig. 53b. A comparison of the main characteristics of working and planned fragment-separator centers created for the RIB studies around the world is presented in Table 4. Additional information about foreign centers was given in Section 1.4.

A zero-angle spectrometer plays an important role in this project. The D3 dipole magnet installed behind the F5 focal plane (Fig. 54) at a distance of 40–60 cm from the target

**Table 4.** Characteristics of in-flight RIB separators:  $\delta_p = \Delta p/p$ —momentum acceptance, and  $p/\Delta p$ —first-order momentum resolution obtained in the achromatic focal plane (F3 and F4 for ACCULINNA and ACCULINNA-2, respectively) at a 1-mm slit size in the F1 focal plane.

Characteristics	ACC FLNR–JINR	ACC-2	LISE3 GANIL	A1900* MSU–NSCL	ARIS* MSU–NSCL	RIPS RIKEN	BigRIPS* RIKEN	FRS GSI–FAIR	SuperFRS* GSI–FAIR
$\Delta\Omega$ , msr	0.9	5.8	1.0	8.0	8.0	5.0	8.0	0.32	5.0
$\delta_p$ , %	2.5	6.0	5.0	5.5	5.5	6.0	6.0	2.0	5.0
$p/\Delta p$	1000	2000	2200	2915	4000	1500	3300	8600	3050
$B\rho_{\text{max}}$ , T m	3.2	3.9	3.2–4.3	6.0	8.0	5.76	9.0	18	18
Length, m	21	38	19(42)	55	70	21	77	74	140
$E_{\text{min}}$ , MeV per nucleon	10	5	40	90	100	50	100	220	300
$E_{\text{max}}$ , MeV per nucleon	40	50	80	160	300	90	350	1000	1500

\* Superconducting magnets are used in the ion-optical system.



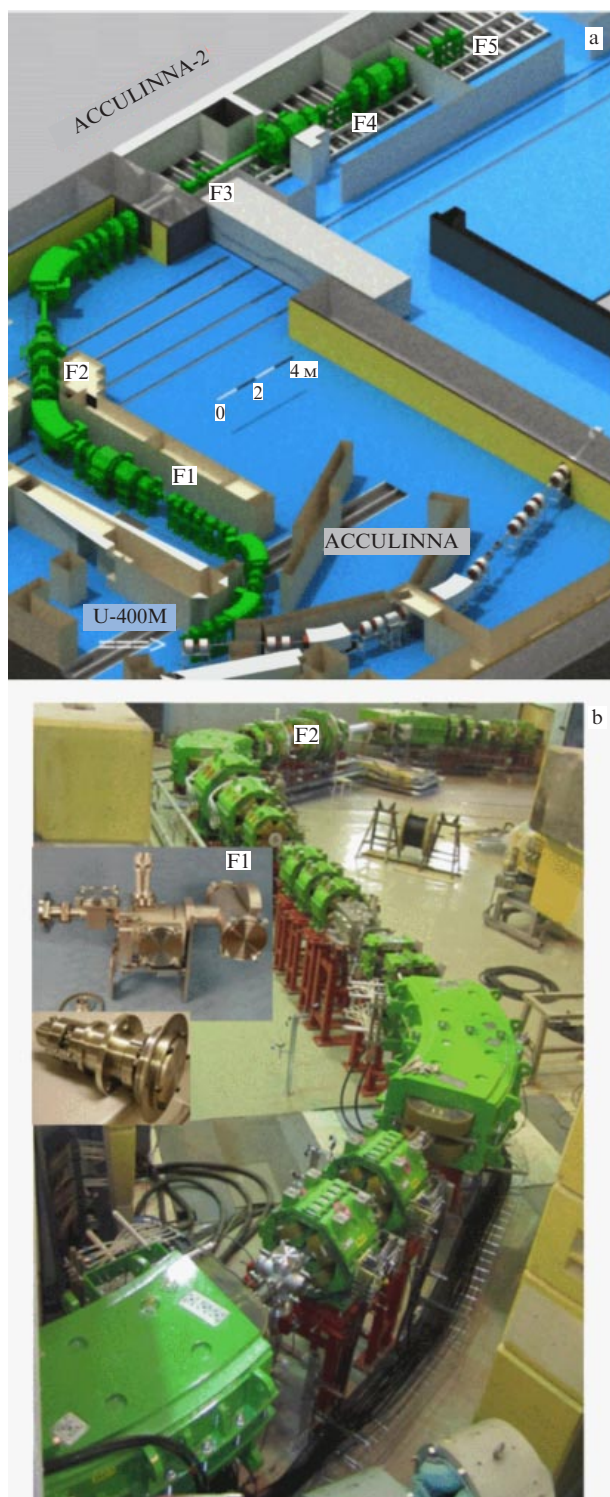


**Figure 53.** (a) Layout of the ACCULINNA and ACCULINNA-2 separators in the building of the U-400M cyclotron. (b) View of the ACCULINNA-2 separator in the U-400M cyclotron hall. The inset on the left of the photo shows the chamber housing the production target ready for installation in the F1 plane. In front is the water-cooled unit of the rotating target.

provides high accuracy in determining the momentum for reaction products with  $Z = 1 - 30$ , emitted in the forward direction. Nuclei with excess protons, produced in direct reactions on targets containing isotopes of hydrogen or helium, move forward in a narrow cone around the axis of

the incident RIB. These nuclei tend to emit in-flight one or two protons within a short period of time ( $\ll 10^{-10}$  s). Both the residual nucleus and the protons emitted from it pass through a gap in the D3 magnet with a probability of 20–60%. Taking into account that the point of emission from the target is known with an accuracy of better than 1 mm, it is enough to provide the same accuracy for measurements of particle coordinates before entry into the magnetic gap and in two planes behind the gap. These two planes are separated from each other by 1–2 m. Thus, the momenta of the three particles will be measured with an accuracy of  $\sim 0.1\%$  and the invariant mass will be determined with a good accuracy, i.e., the invariant mass resolution does not exceed 100 keV, and the error in its determination is on the order of 10 keV in the case of reasonably high statistics. Use of the D3 dipole magnet significantly extends the capacity to study nuclei in the vicinity of the neutron drip line as well. The charged reaction products are detected outside of the beam axis, while neutrons emitted from the decay of these nuclei pass through a wide magnetic gap and are detected by scintillation detectors installed at a distance of 3–4 m from the target in the vicinity of the zero angle with a sufficiently high probability. The error in the invariant mass measurement does not exceed 300 keV for such reactions.

The first experiments on the new separator will be performed in 2016. The RIB research program, including further development of the facility, provides: (1) startup of the D3 zero-angle spectrometer at F5 (according to the contract with the Sigmaphi company, it is expected in mid-2016); (2) manufacturing and launch of the RF filter on the F3–F4 path in 2017, and (3) creation of a new gas–vacuum system for operation with cryogenic targets, including a tritium one (after 2017).

## 6.2 User center built around ACCULINNA-2

Nowadays, the world's major RIB research centers operate in the user center mode. The desirable RIB and massive scientific equipment for a specific experiment are provided by research centers in the 'scientific service' mode, usually carried out in terms of a decision by PAC (Program Advisory Committee)—a representative international council. This allows the creation of a setup from large modules for a specific experiment, like a Lego set. The idea and the design of an experimental setup, the fabrication of unique experimental equipment, and the analysis of data are the business of 'guests'.

User facilities provide all the advantages of an industrial approach to the organization of the experiment, i.e., a series of experiments give the opportunity to efficiently utilize the beam time, to carry out the rational allocation of work, and to concentrate funds on the key tasks during the construction and operation of the massive tools. The scientific groups conducting the experiment are no longer required to maintain all the experimental infrastructure (high-priced, but mostly trivial); they can devote much more time to the improvement of unique equipment and data analysis.

The most important aspect of the work of the user centers is the broad collaboration and availability of research infrastructure. Differences between ideas about the 'center' and 'periphery' are fading thanks to the availability of the scientific infrastructure: exceptionally expensive world-class equipment becomes affordable for researchers from 'peripheral' scientific organizations. Such an opportunity is especially important for young scientists, because the user facility



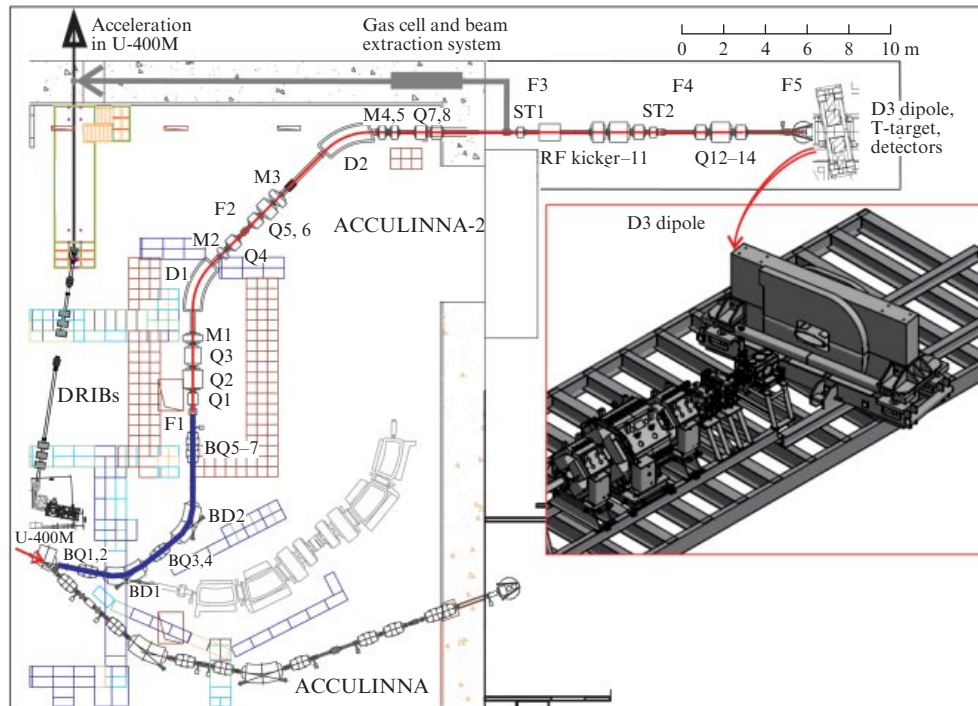


**Figure 54.** (Color online.) Development plan for DRIBs complex for 2017–2023: BD1-2 and BQ1-7—dipole and quadrupole magnets of the primary beam line; D1-2, Q1-14, M1-5—dipole, quadrupole, and multipole magnets of the secondary beam line, and ST1-2—steering magnets in the vertical plane for operation with the RF kicker. Dipole magnet D3, to be launched in 2016, is shown in the inset on the right panel.

becomes for them an interaction point with the leading experts.

The multiuser ideology of RIB nuclear centers is very different from the collaboration work in the field of high energy physics. The members of the collaboration are usually responsible for a narrow range of technical tasks there, and the ‘center’ formulates the scientific program. Nuclear physics experiments have not reached the scale and complexity of experiments in high energy physics. And ‘guest’ experiments on RIBs usually have an autonomous and independent scientific program.

We consider it possible that ACCULINNA-2 will be brought to the standard of user centers. There are several unsolved problems here: improvement of the stability of RIB production, increase in RIB diversity, the formation of a massive pool of modular equipment that can be routinely used upon request, and, finally, simplification of access to a beam time. Preparatory work in this area is already going on, and it seems that the full formalization of such an initiative within the framework of JINR will help to speed it up.

The ACCULINNA-2 facility includes several successfully developing infrastructure subprojects which might provide the basis for the user facility. These subprojects are an RF-kicker, a gas-filled cell with a system of extraction of single-charge ions and a line of their subsequent acceleration, a tritium target facility, and detector systems (see Fig. 54). The D3 dipole magnet (zero-angle spectrometer) is shown in the inset to Fig. 54. Different purpose detectors are also under construction. Arrays of neutron detectors (based on stilbene) and gamma-detectors (GADAST) experiencing quantitative enlargement have been discussed in Section 4.3. A project concerning the construction of a charged particle detector with the best characteristics (time and position resolutions) available today is another important course of development.

The presence of an effective source, i.e., an accelerator of heavy ions, is a basic element for operation with RIB. The long-range development plan of the DRIBs complex (2017–2023) assumes the reconstruction of U-400 and U-400M cyclotrons. After reconstruction, it will be possible to smoothly adjust the beam energy and expand the range of primary beam energies at U-400M to 60–80 MeV per nucleon. One of the main goals of the upgrade is to produce beams of heavy ions with proton numbers in the range of  $Z = 3–28$  (from Li to Ni) with energies up to 80 MeV per nucleon. It is planned to create beams of  $^{78–86}\text{Kr}$  nuclei with the energy of 30–35 MeV per nucleon, and beams of heavier nuclei up to uranium with an energy of about 10 MeV per nucleon. The intensity of such beams will usually reach values of 0.5–1.0  $\mu\text{A}$ . The beam extraction from the cyclotron is supposed to be done using an electrostatic deflector. The transition from the current typical energy of 33–50 MeV per nucleon for  $Z = 3–28$  at U-400M to energies of 60–80 MeV per nucleon will lead to an increase in RIB intensities at the ACCULINNA-2 separator by 5–20 times over the proposed intensities. At the same time, the thickness of the targets made up from  $^1\text{--}^3\text{H}$  and  $^3,^4\text{He}$  isotopes and irradiated during the experiments, can be increased 3–5 times. The luminosity will hence increase 15–200 times compared to the planned values for ACCULINNA-2, as a result of the accelerator’s upgrade. This will bring the facility to a new quality of operation.

The ISOL method of RIB production can be applied in exploiting the ACCULINNA-2 facility in the future. A gas catcher should be manufactured and mounted in the F3 focal plane to extract RIBs passing through a gas. Both the upgrade of the U-400 cyclotron and the development of ISOL technology on the base of the ACCULINNA-2 facility will expand the available range of tasks at low energies. The

**Table 5.** Expected intensities  $I$  of several RIBs after the upgrade of the DRIBs complex.\*

RI beam	${}^6\text{He}$	${}^8\text{He}$	${}^9\text{Li}$	${}^{12}\text{Be}$	${}^8\text{B}$	${}^{16}\text{C}$	${}^{17}\text{F}$	${}^{34}\text{Si}$	${}^{46}\text{Ar}$
$I$ , number of particles per s	$1 \times 10^8$	$3 \times 10^5$	$5 \times 10^5$	$7 \times 10^5$	$3 \times 10^5$	$6 \times 10^5$	$7 \times 10^6$	$2 \times 10^5$	$3 \times 10^5$

\* Possibility of continuous tuning of the RIB energy is provided in the range of 5–20 MeV per nucleon. Purity of all RI beams is 100%.

expected RIB parameters at the U-400M–ACCULINNA–U-400 complex are presented in Table 5.

### 6.3 Project EXPERT

FAIR is the project of global renovation of the GSI center in Germany [11]. Four main collaborations with various physical agendas are involved in FAIR: CBM (Compressed Baryonic Matter), APPA (Atomic, Plasma Physics, and Applied sciences), and PANDA (antiProton ANnihilation at DArmstadt). The nuclear physics component of FAIR — NUSTAR (NUclear STructure, Astrophysics, Reactions) — should become the most advanced RIB factory in the world due to the high energy of primary beams from the SIS-100 synchrotron (up to 2.7 GeV per nucleon) and a powerful superconducting fragment separator Super-FRS.

The FAIR center should become an international research organization (10 main participating countries in 2015). At the same time, the Russian Federation is the main partner of FAIR from abroad, with approximately 14% of the shares (that is about 180 million euros in 2005 prices). A large part of the Russian contribution should be delivered in the form of components, devices, and facilities manufactured domestically. At the moment, the main funds are planned to be directed to the creation of magnets, ion-optical systems, and massive detector components.

The NUSTAR collaboration implements a number of research projects, including the project EXPERT, which refers to experiments on relativistic kinematics. It is a relatively cheap experiment which is planned to be held directly inside the Super-FRS fragment separator [198]. EXPERT is distinguished by the fact that this is one of the few projects in which the scientific initiative comes from the Russian side and the facility itself has a dominant Russian financial and intellectual contribution.

The main component of the EXPERT project is based on a new experimental method developed in the last decade in the work of I G Mukha and his collaborators (GSI/RNC KI) [9, 36, 85, 199, 200]. This method was initially designed to investigate radioactive decays with particle emission using the product tracking method (Fig. 55). If the lifetime of a nuclear system is large enough to pass a macroscopic distance with a relativistic speed, this time can be determined by the distribution of decay vertices in space. The vertices can be reconstructed using position-sensitive microstrip silicon detectors. In fact, this advance is not new: it is widely used in elementary particle physics. However, such an approach has never been applied in nuclear physics before because of a fundamental difficulty: the energy deposit of a charged particle in the detector increases with increasing charge as  $Z^2$ , and a heavy ion begins to ‘shadow’ protons. Thus, for the decay  ${}^{30}\text{Ar} \rightarrow {}^{28}\text{S} + p + p$  [36] the energy deposit of the heavy fragment is about 250 times larger than the proton one. This difficulty has been eliminated in the new generation of microstrip (pitch  $\approx 100\ \mu\text{m}$ ) silicon detectors equipped with digital electronics. The high spatial resolution of such detectors ( $\approx 30\ \mu\text{m}$  for protons, and  $\approx 12\ \mu\text{m}$  for heavy

ions) provides high angular resolution,  $\approx 0.1\ \text{mrad}$ , and, thus, high accuracy in reconstructing the decay vertex. For example, to determine the half-life of  ${}^{19}\text{Mg}$  with  $T_{1/2} \approx 4\ \text{ps}$  in the experiment [9], the error in vertex reconstruction had to be less than 0.5 mm. The employment of the last achromatic section of the fragment separator (Fig. 56) to trace the heavy fragment additionally increases the angular resolution between protons and the heavy fragment and ensures unambiguous identification of the latter.

The ability to obtain spectroscopic information with high accuracy has been another advantage of the method with product tracking. This is quite unexpected, since this method does not provide reconstruction of the full kinematics (emission directions of fragments are measured, but their energies are not); therefore, the invariant mass cannot be determined. The possibility of determining the energy of states is associated with so-called kinematic focusing (see papers [9, 85]). This effect can be easily explained in the case of two-particle decays with a fixed energy (Fig. 55b). Particles isotropically emitted in the center-of-mass frame are concentrated near the surface of the cone corresponding to the maximum possible angle in the laboratory frame. The kinematic effect begins to depend on correlations between the fragments in the case of three-particle decays and, therefore, the accuracy of the energy reconstruction using the experimental data begins to depend on the quality of theoretical predictions for correlations. Thus, the develop-

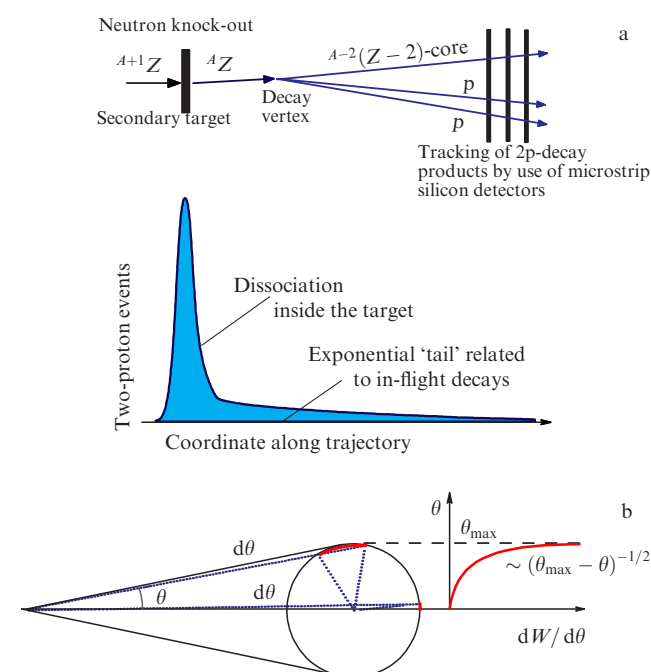


**Figure 55.** (a) Schematic of experiment studying radioactivity with particle emission (two-proton one in this case) using track detectors within relativistic kinematics, (b) Kinematic focusing in the experiment with tracking by the example of a two-particle decay.

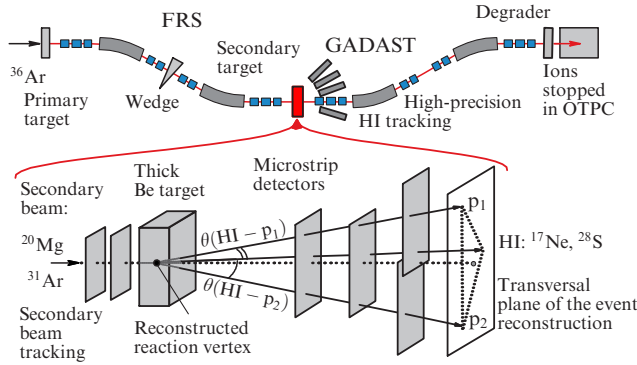


**Figure 56.** Components of the EXPERT project by the example of an experiment already performed [36].

ment of theoretical methods and MC simulations are the necessary components of the EXPERT project.

An important advantage of the considered technique is the ability to work with very thick targets without irreversible degradation of the resolution. The (beryllium) target thickness in experiments [9] and [36] was 20 and 27 mm, respectively, which is several hundred times larger than in the case of a typical low-energy experiment. This makes this technique attractive for pioneering studies with RIBs of low intensity.

The assemblage of equipment in experiment [36] was extended to that of the original facility [9] and was a functioning prototype of the EXPERT project (see Fig. 56). The GADAST gamma-detector was positioned in the area of the secondary target (see Section 4.3). Registration of gamma-rays should allow discrimination of events corresponding to emission of excited heavy fragments (deexciting by gamma-quanta) in the future. An absorber, decreasing the energy of heavy fragment to several MeV per nucleon, was installed in the final focus of FRS for the sake of subsequent implantation to OTPC (another element of EXPERT; see Section 4.5). This gave the opportunity to study the beta-delayed decays of heavy fragments [149], which itself represents a rather exotic system, and thus enhanced the scientific value of the experiment.

This is how we see that EXPERT is a really functioning system. The project is distinguished by wide international collaboration, the use of modern technologies, and its modularity. The EXPERT project includes development of fast-operating and radiation-hard silicon strip detectors for beam monitoring and the creation of the NeuRad high-resolution neutron detector in its full version. The opportunity to use the EXPERT components in experiments at the ACCULINNA-2 facility is also of importance to us.

#### 6.4 Storage ring complex and electron-ion collider based on ACCULINNA-2

A fundamentally important issue is the problem of extraction of information free from features associated with the mechanism of the reaction, if we consider nuclear reactions as a tool for studying nuclear structure. The use of the ‘electromagnetic test’ instead of the ‘strong sample’ and, accordingly, consideration of all the uncertainties associated with the strong interaction is a possible solution to this problem. Electron-nucleus scattering is the most powerful method: electrons with sufficient energy start to feel the contribution from pure Coulomb interaction related to the charge distribution  $\rho_{ch}$  in the nucleus. The simplest plane-

wave Born approximation (PWBA) already allows associating such an important characteristic as the charge radius  $\langle r_{ch}^2 \rangle$  of the ion with the electron scattering cross section via the charge form factor  $F(q)$ :

$$\left( \frac{d\sigma}{d\Omega} \right)_{PWBA} = \frac{Ze^2}{4E} \frac{1}{\sin^4(\theta/2)} |F(q)|^2, \quad q = 2k \sin \frac{\theta}{2},$$

$$F(q) = 4\pi \int dr r^2 j_0(qr) \rho_{ch}(r), \quad \frac{F(q)}{Z} = 1 - \frac{q^2}{6} \langle r_{ch}^2 \rangle + \dots$$

Studies of the electromagnetic form factors of stable nuclei achieved exceptional excellence [201], and the pioneering work of R Hofstadter in this field [202] was awarded a Nobel Prize in Physics 1961.

Since it is impossible to create a target of radioactive ions, we can consider only a collider type experiment, in which the RIB will interact with the electron beam. This feature was incorporated in the design of the K4-K10 radioactive ion complex planned in the late 1980s as a project of a massive upgrade of the JINR FLNR [28]. When it became apparent that K4-K10 will not be implemented, the initiative was taken up by RIKEN (Japan). However, the practical development of the FRIB project (Facility for Rare Isotope Beams) led to a gradual reduction of the storage-ring topic: only one small storage ring spectrometer with limited functionality was built. RIKEN continues the development of the subject of the electron-RIB collisions in the framework of the project SCRIT (Self-Confining Radioactive Ion Target). They are trying to implement an original approach: a target of radioactive ions is formed by their accumulation in an electromagnetic trap. It is a test project which is implemented aside the main RIB production facilities.

A storage ring facility is a serious part of the FAIR project (Germany): CR (Collector Ring) for accumulation and cooling of beam, and NESR (Next to the Experimental Storage Ring) designed for research with the accumulated radioactive ions. The ELISE experiment on electron-radioactive ion scattering at NESR [30], developed with the active participation of Russian scientists, has reached a very high degree of sophistication. However, the delay in realization of the FAIR project as a whole has postponed the implementation of the idea of such experiments to the distant future.

The uncertain situation in the world with the implementation of projects of electron-radioactive ion scattering has returned discussions about such an opportunity in our country. A project on the construction of a K5 complex on the base of the ACCULINNA-2 fragment separator (Fig. 57) was presented at the RAS Council on the Physics of Heavy Ions in 2013. Ironically, the logic of the existing experimental base dictates a solution, to a large degree, similar to the K4-K10 proposal brought forward almost 30 years ago. Storage ring technology represents a high-tech facility even in the world of technologically advanced nuclear experiments: ultrahigh vacuum, high-power subnanosecond electronics, exceptionally accurate ion optics. The implementation of this project will require raising the national experimental culture at a whole new level.

#### 6.5 Storage ring complex for direct reactions with beams of radioactive isotopes

Finally, the most expensive but also the most interesting project for the future is the construction of a storage-ring



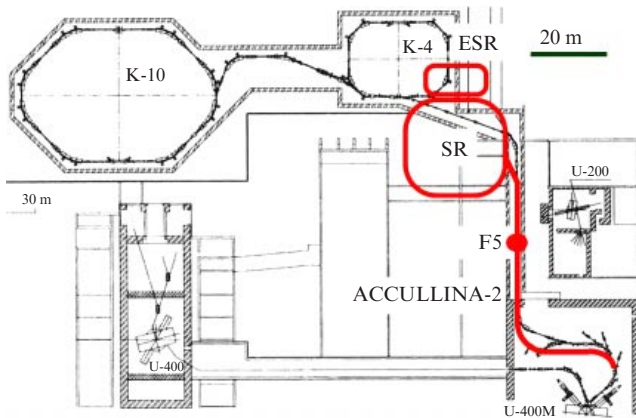


**Figure 57.** Possible placement of a K5 storage ring (SR) and electron storage ring (ESR) for the electron–RIB collider. The schematics shown in the background represents the project K4–K10 from 1989 and the layout for the existing buildings with the U-400M, U-400, and U-200 cyclotrons at JINR FLNR.

complex for precision studies of reactions with RIBs. A similar complex can be created on a K5 storage ring (maximum magnetic rigidity of the ion beam  $B\rho_{\max} = 5.0$  T m) operating in the mode of *merging beams* with a second K3.6 ring ( $B\rho_{\max} = 3.6$  T m). Qualitatively, it is the ‘anticollider’ mode, where the velocity of the center-of-mass of the reaction increases due to the movement of the target in the same direction as the beam. Work with merging beams allows flexibly choosing between the direct and inverse reaction kinematics, eliminating any restrictions which are often called kinematically unfavorable operating conditions with a stationary target. The structure of the K3.6 ring must ensure the accumulation of cooled beams in the orbit up to  $10^{13}$  light stable/long-lived nuclei (p, d, t,  $^3\text{He}$ ,  $^4\text{He}$ ,  $^{10}\text{Be}$ ,  $^{14}\text{C}$ , etc.).

The aim of the K5 ring is to accumulate and to cool the RIBs produced by the ACCULINNA-2 fragment separator. It is proposed to install a gas catcher (see paper [203]) to perform this task behind the F5 focal plane. Devices ensuring the accumulation of a flow of single-charged radioactive ions, extracted from the gas catcher, have been created and tested elsewhere in the world. A bunch of radioactive ions accumulated and cooled in a penning trap [204] is transferred to an electromagnetic trap — an ion source increasing the ion charge within a short time interval (about 100 ms). Perfect ion sources, ECR (see, e.g., Ref. [205]) or electron-string [‘KRION’, EBIS (Electron Beam Ion Source)] (see Refs [206, 207]), allow fully stripped nuclei with proton number  $Z < 20$  to be obtained.

The results of several research groups (see reviews [208, 209]) show that the breeding effectiveness of more than 20% will be achieved in the near future for radioactive nuclei with lifetimes of more than 100 ms. The time of acceleration of an RIB bunch to an energy of 5–10 MeV per nucleon, its injection into the orbit of K5, and cooling down will be 5–10 ms. Such time economy will provide the electron cooling discovered by G I Budker and brought to perfection at Budker INP SB RAS (Novosibirsk) [210, 211]. Within 1 minute, about  $10^9$  long-lived radioactive ions can be collected in the orbit of K5, using the accumulation–cooling mode proposed in the draft K4–K10 [28]. It is estimated that one 100-ms bunch with an emittance of  $\tau_{\perp} = 0.1\pi$  mm mrad,  $\Delta p/p_0 = 10^{-6}$ , will be accumulated and cooled in about 10 ms.

An estimation of the luminosity achievable in this project in a merging mode of the beams depends on the lifetime and intensity of RIBs at the output of the ACCULINNA-2 fragment separator. Thus, the maximum luminosity of  $10^{25} - 10^{26} \text{ cm}^{-2} \text{ s}^{-1}$  can be obtained for experiments with RIBs of  $^{16}\text{C}$  ( $T_{1/2} = 0.75$  s) and  $^{46}\text{Ar}$  ( $T_{1/2} = 7.8$  s) nuclei.

Experiments with merging beams are particularly interesting due to the unprecedented high-precision determination of the energy of the products of direct reactions with radioactive ions, as we have discussed in Section 2. Measurements of the excitation energy spectra of exotic nuclei will be performed in such experiments with a resolution of at least 1 keV.

## 7. Conclusion

Original methods for the study of light nuclear systems near the borders of nucleon stability and beyond have been developed in experiments at the ACCULINNA fragment separator, JINR FLNR, in the last two decades. These techniques are based on correlation methods especially efficient for direct reactions studies at intermediate energies. On the one hand, this area is not in the mainstream of modern studies with RIBs, which constantly tend to increase incident energies. On the other hand, there are numerous fundamental advantages of this approach, which can be implemented in the performance of complex correlation experiments. A quite low statistics and the qualitative rather than quantitative nature of the received information are characteristic for pioneering experiments with RIBs. It is expected that they will be followed by experiments with a high accuracy and probative value. This is the direction we are moving in.

The present paper overviews theoretical results in the field of few-body dynamics. This form of nuclear dynamics arises in clustered systems near the borders of nuclear stability and leads to such phenomena as the nuclear halo, soft modes of excitation, and radioactive decay with emission of several (two or more) particles. The understanding of such phenomena is fragmented, and the significant progress achieved in this field in recent years makes this review relevant.

We have presented our workplace in the context of modern research conducted with RIBs throughout the world. Several promising projects, both implemented in our country and with our participation abroad, and potential ones have been considered here.

Looking back at the material presented in this review, we see that the theoretical concepts and experimental results are tightly intertwined, sometimes in a very fanciful way. This might create some difficulties in perception; however, it seems to us that it correctly reflects the spirit of research in this rapidly developing field.

## Acknowledgments

Director of FLNR, S N Dmitriev, comprehensively supporting the presented area of research, suggested writing this paper and actively followed up on its progress. FLNR scientific leader Yu Ts Oganessian is the initiator of the study of light exotic nuclei in our laboratory and a coauthor of many presented papers. I G Mukha promotes the project EXPERT and plays an important role in supporting the scientific collaboration of FLNR and GSI on the topic of RIB studies. We are grateful to M V Zhukov for his long-term collaboration and theoretical support of our research programs, as well as for important suggestions on the



content of the present review. The authors are grateful to A A Korshennikov for the kind words about this paper, long-term support, and development of the FLNR collaboration with RNC KI and RIKEN. The authors express their sincere gratitude to all the staff of the ACCULINNA facility, especially to A G Knyazev and P G Sharov. We are grateful to A L Barabanov, T A Golubkova, and V V Pokhmelnikh for the assistance provided in carrying out this work and for numerous useful comments. Yu M Chuvisky made many important comments and suggestions regarding the content of this review. The work was performed under the partial support of grant 14-02-00090-a of RFBR and a grant from the Ministry of Education and Science of the Russian Federation, NSH-932.2014.2.

## References

- National Nuclear Data Center. Brookhaven National Laboratory, <http://www.nndc.bnl.gov/>
- ACCULINNA. JINR, <http://aculina.jinr.ru/>
- Fomichev A S et al., Preprint E13-2008 (Dubna: JINR, 2008)
- Grigorenko L V *Phys. Part. Nucl.* **40** 674 (2009); *Fiz. Elem. Chast. At. Yad.* **40** 1271 (2009)
- Fomichev A S et al., Preprint JINR E7-2012-73 (Dubna: JINR, 2012)
- Ter-Akopian G M, Sidorchuk, S I, Grigorenko L V "Breakdown of shell closure in helium-10", in *McGraw-Hill Yearbook of Science and Technology* (New York: McGraw-Hill, 2012)
- Grigorenko L, Fomichev A, Ter-Akopian G *Nucl. Phys. News* **24** (4) 22 (2014)
- Baz' A I *Sov. Phys. JETP* **6** 709 (1958); *Zh. Eksp. Teor. Fiz.* **33** 923 (1958)
- Mukha I et al. *Phys. Rev. Lett.* **99** 182501 (2007)
- GSI Helmholtzzentrum für Schwerionenforschung GmbH, <http://www.gsi.de/>
- FAIR: Facility for Antiproton and Ion Research in Europe GmbH, <http://www.fair-center.eu>
- RIKEN Nishina Center for Accelerator-Based Science (RNC), <http://www.riken.jp/en/research/labs/rnc/>
- National Superconducting Cyclotron Laboratory, Michigan State Univ., <http://www.nsl.msu.edu/>
- GANIL SPIRAL2 Grand Accélérateur National d'Ions Lourds, <http://www.ganil-spiral2.eu/>
- Toschek P E "Atomic particles in traps", in *New Trends in Atomic Physics, Course 3: Les Houches, Session XXXVIII, June 28–July 29, 1982* Vol. 1 (Eds G Grynberg, R Stora) (Amsterdam: Elsevier, 1984) p. 383; Translated into Russian: *Usp. Fiz. Nauk* **158** 451 (1989)
- Brown L S, Gabrielse G *Rev. Mod. Phys.* **58** 233 (1986)
- Franzke B, Geissel H, Münzenberg G *Mass Spectrom. Rev.* **21** 428 (2008)
- Litvinov Y A et al. *Acta Phys. Pol.* **B 41** 511 (2010)
- Dickel T et al. *Nucl. Instrum. Meth. Phys. Res. A* **777** 172 (2015)
- Akkoyun S et al. *Nucl. Instrum. Meth. Phys. Res. A* **668** 26 (2012)
- Hofmann S et al. *Z. Phys. A* **305** 111 (1982)
- Pfützner M et al. *Eur. Phys. J. A* **14** 279 (2002)
- Giovinazzo J et al. *Phys. Rev. Lett.* **89** 102501 (2002)
- Grigorenko L V et al. *Phys. Rev. C* **84** 021303(R) (2011)
- Pfützner M, Karny M, Grigorenko L V, Riisager K *Rev. Mod. Phys.* **84** 567 (2012)
- Rodin A M et al. *Nucl. Instrum. Meth. Phys. Res. B* **204** 114 (2003)
- Flerov Laboratory of Nuclear Reactions. The Dubna Radioactive Ion Beam, <http://159.93.28.88/flnr/dribs.html>
- Oganessian Yu Ts et al. *Z. Phys. A* **341** 217 (1992)
- The Institute of Modern Physics (IMP) of the Chinese Academy of Sciences, <http://english.imp.cas.cn/>
- Antonov A N et al. *Nucl. Instrum. Meth. Phys. Res. A* **637** 60 (2011)
- Treiman S B, Yang C N *Phys. Rev. Lett.* **8** 140 (1962)
- Shapiro I S, Kolybasov V M, Augst G R *Nucl. Phys.* **61** 353 (1965)
- Sitenko A G *Theory of Nuclear Reactions* (Singapore: World Scientific, 1990); Translated from Russian: *Teoriya Yadernykh Reaktsii* (Moscow: Energoatomizdat, 1983)
- Satchler G R *Direct Nuclear Reactions* (Oxford: Clarendon Press, 1983)
- Bromley D A (Ed.) *Treatise on Heavy-Ion Science* (New York: Plenum, 1984–1989)
- Mukha I et al. *Phys. Rev. Lett.* **115** 202501 (2015)
- Artemov K P et al. *Sov. J. Nucl. Phys.* **52** 408 (1990); *Yad. Fiz.* **52** 634 (1990)
- Goldberg V Z et al. *JETP Lett.* **67** 1013 (1998); *Pis'ma Zh. Eksp. Teor. Fiz.* **67** 959 (1998)
- Markenroth K et al. *Phys. Rev. C* **62** 034308 (2000)
- Assié M et al. *Phys. Lett. B* **712** 198 (2012)
- Fifield L K, Balamuth D P, Zurmühle R W *Phys. Rev. C* **15** 1595(R) (1977)
- Biedenbarn L C, Rose M E *Rev. Mod. Phys.* **25** 729 (1953)
- Barabanov A L *Simmetrii i Spin-Uglovyie Korrelyatsii v Reaktsiyakh i Raspadakh* (Symmetry and Spin-Angle Correlations in Reactions and Decays) (Moscow: Fizmatlit, 2010)
- Artemov K P et al. *Sov. J. Nucl. Phys.* **14** 615 (1972); *Yad. Fiz.* **14** 1105 (1972)
- Miernik K et al. *Phys. Rev. Lett.* **99** 192501 (2007)
- Grigorenko L V et al. *Phys. Lett. B* **677** 30 (2009)
- Egorova I A et al. *Phys. Rev. Lett.* **109** 202502 (2012)
- Simonov Yu A *Sov. J. Nucl. Phys.* **3** 461 (1966); *Yad. Fiz.* **3** 630 (1966)
- Badalian A N, Simonov Yu A *Sov. J. Nucl. Phys.* **3** 755 (1966); *Yad. Fiz.* **3** 1032 (1966)
- Smirnov Yu F, Shitikov K V *Fiz. Elem. Chast. At. Yad.* **8** 847 (1977)
- Baz' A I, Zhukov M V *Sov. J. Nucl. Phys.* **11** 435 (1970); *Yad. Fiz.* **11** 779 (1970)
- Vostrikov A N, Zhukov M V *Sov. J. Nucl. Phys.* **26** 377 (1977); *Yad. Fiz.* **26** 716 (1977)
- Demin V F, Pokrovsky Yu E, Efros V D *Phys. Lett. B* **44** 227 (1973)
- Efros V D *Sov. J. Nucl. Phys.* **15** 128 (1972); *Yad. Fiz.* **15** 226 (1972)
- Dzhibuti R I, Shitikova K V *Metod Gipersfericheskikh Funktsii v Atomnoi i Yadernoi Fizike* (The Method of Hyperspherical Functions in Atomic and Nuclear Physics) (Moscow: Energoatomizdat, 1993)
- Zhukov M V et al. *Phys. Rep.* **231** 151 (1993)
- Ershov S N, Grigorenko L V, Vaagen J S, Zhukov M V *J. Phys. G* **37** 064026 (2010)
- Grigorenko L V et al. *Phys. Rev. Lett.* **85** 22 (2000)
- Danilin B V et al. *Phys. Rev. C* **43** 2835 (1991)
- Grigorenko L V et al. *Phys. Rev. C* **57** R2099 (1998)
- Grigorenko L V et al. *Phys. Rev. C* **64** 054002 (2001)
- Grigorenko L V, Zhukov M V *Phys. Rev. C* **77** 034611 (2008)
- Grigorenko L V et al. *Phys. Rev. C* **80** 034602 (2009)
- Tanihata I et al. *Phys. Rev. Lett.* **55** 2676 (1985)
- Kukulin V I et al. *Nucl. Phys. A* **453** 365 (1986)
- Danilin B V et al. *Sov. J. Nucl. Phys.* **48** 766 (1988); *Yad. Fiz.* **48** 1208 (1988)
- Ikeda K, INS Report JHP-7 (1988) (in Japanese)
- Aumann T *Eur. Phys. J. A* **26** 441 (2005)
- Schümann F et al. *Phys. Rev. Lett.* **90** 232501 (2003)
- Cortina-Gil D et al. *Nucl. Phys. A* **720** 3 (2003)
- Grigorenko L V et al. *Phys. Lett. B* **641** 254 (2006)
- Hammache F et al. *Phys. Rev. C* **82** 065803 (2010)
- Marganec J et al. *J. Phys. Conf. Ser.* **337** 012011 (2012)
- Kanungo R et al. *Phys. Rev. Lett.* **114** 192502 (2015)
- Nakamura T et al. *Phys. Rev. Lett.* **96** 252502 (2006)
- Goldansky V I *Nucl. Phys.* **19** 482 (1960)
- Zel'dovich Ya B *Sov. Phys. JETP* **11** 812 (1960); *Zh. Eksp. Teor. Fiz.* **38** 1123 (1960)
- Goldansky V I *Nucl. Phys.* **27** 648 (1961)
- Galitsky V M, Cheltsov V F *Nucl. Phys.* **56** 86 (1964)
- Brown B A *Phys. Rev. C* **43** R1513 (1991)
- Barker F C *Phys. Rev. C* **63** 047303 (2001)
- Brown B A, Barker F C *Phys. Rev. C* **67** 041304(R) (2003)
- Dossat C et al. *Phys. Rev. C* **72** 054315 (2005)
- Blank B et al. *Phys. Rev. Lett.* **94** 232501 (2005)
- Mukha I et al. *Phys. Rev. C* **77** 061303(R) (2008)
- Ascher P et al. *Phys. Rev. Lett.* **107** 102502 (2011)
- Grigorenko L V, Mukha I G, Zhukov M V *Nucl. Phys. A* **713** 372 (2003); *Nucl. Phys. A* **740** 401 (2004) erratum
- Grigorenko L V, Mukha I G, Zhukov M V *Nucl. Phys. A* **714** 425 (2003)
- Grigorenko L V, Zhukov M V *Phys. Rev. C* **68** 054005 (2003)
- Grigorenko L V, Zhukov M V *Phys. Rev. C* **76** 014008 (2007)
- Grigorenko L V, Zhukov M V *Phys. Rev. C* **76** 014009 (2007)
- Grigorenko L V et al. *Phys. Rev. C* **82** 014615 (2010)

93. Brown K W et al. *Phys. Rev. Lett.* **113** 232501 (2014)
94. Fomichev A S et al. *Int. J. Mod. Phys. E* **20** 1491 (2011)
95. Grigorenko L V, Zhukov M V *Phys. Rev. C* **72** 015803 (2005)
96. Görres J, Wiescher M, Thielemann F-K *Phys. Rev. C* **51** 392 (1995)
97. Fowler W, Caughlan G, Zimmerman B *Annu. Rev. Astron. Astrophys.* **5** 525 (1967)
98. Angulo C et al. *Nucl. Phys. A* **656** 3 (1999)
99. Geesaman D F et al. *Phys. Rev. C* **15** 1835 (1977)
100. Bochkarev O V et al. *Nucl. Phys. A* **505** 215 (1989)
101. Fomichev A S et al. *Phys. Lett. B* **708** 6 (2012)
102. Jager M F et al. *Phys. Rev. C* **86** 011304(R) (2012)
103. Wamers F et al. *Phys. Rev. Lett.* **112** 132502 (2014)
104. Brown K W et al. *Phys. Rev. C* **92** 034329 (2015)
105. Shul'gina N B et al. *Phys. Rev. C* **62** 014312 (2000)
106. Grigorenko L V, Timofeyuk N K, Zhukov M V *Eur. Phys. J. A* **19** 187 (2004)
107. Grigorenko L V *Eur. Phys. J. A* **20** 419 (2004)
108. Sharov P G, Egorova I A, Grigorenko L V *Phys. Rev. C* **90** 024610 (2014)
109. Grigorenko L V et al. *Phys. Rev. C* **86** 061602(R) (2012)
110. Grigorenko L V, Zhukov M V *Phys. Rev. C* **91** 064617 (2015)
111. Zaytsev S, Gasaneo G J. *At. Mol. Sci.* **4** 302 (2013)
112. McCurdy C W, Baertschy M, Rescigno T N *J. Phys. B* **37** R137 (2004)
113. Hilico L et al. *Phys. Rev. A* **66** 022101 (2002)
114. Kilic S, Karr J-P, Hilico L *Phys. Rev. A* **70** 042506 (2004)
115. Madronero J et al. *Math. Struct. Comput. Sci.* **17** 225 (2007)
116. Ambrosio M J et al. *Few-Body Syst.* **55** 825 (2014)
117. Thomas R G *Phys. Rev.* **88** 1109 (1952)
118. Ehrman J B *Phys. Rev.* **81** 412 (1951)
119. Comay E, Kelson I, Zidon A *Phys. Lett. B* **210** 31 (1988)
120. Grigorenko L V et al. *Phys. Rev. Lett.* **88** 042502 (2002)
121. Grigorenko L V, Golubkova T A, Zhukov M V *Phys. Rev. C* **91** 024325 (2015)
122. Golovkov M S et al. *Phys. Lett. B* **588** 163 (2004)
123. Kohley Z et al. *Phys. Rev. Lett.* **110** 152501 (2013)
124. Lunderberg E et al. *Phys. Rev. Lett.* **108** 142503 (2012)
125. Caesar C et al. (R3B Collab.) *Phys. Rev. C* **88** 034313 (2013)
126. Kondo Y et al. *JPS Conf. Proc.* **6** 010006 (2015)
127. Grigorenko L V, Mukha I G, Zhukov M V *Phys. Rev. Lett.* **111** 042501 (2013)
128. Gulbekyan G et al. *Phys. Part. Nucl. Lett.* **7** 511 (2010); *Pis'ma Fiz. Elem. Chastits. At. Yad.* **7** 827 (2010)
129. Efremov A et al. *Rev. Sci. Instrum.* **83** 02A334 (2012)
130. Golovkov M S et al., in *Exotic Nuclei, EXON-2014, Proc. of Intern. Symp. on Exotic Nuclei, Kaliningrad, Russia, 8–13 September 2014* (Eds Yu E Penionzhkevich, Yu G Sobolev) (Singapore: World Scientific, 2015) p. 171
131. Slepnev R S et al. *Instrum. Exp. Tech.* **55** 645 (2012); *Prib. Tekh. Eksp.* (6) 41 (2012)
132. Yamada K, Motobayashi T, Tanihata I *Nucl. Phys. A* **746** 156 (2004)
133. Golovkov M S et al. *Phys. Rev. Lett.* **93** 262501 (2004)
134. Golovkov M S et al. *Phys. Rev. C* **72** 064612 (2005)
135. Golovkov M S et al. *Phys. Rev. C* **76** 021605(R) (2007)
136. Golovkov M S et al. *Phys. Lett. B* **672** 22 (2009)
137. Sidorchuk S I et al. *Phys. Rev. Lett.* **108** 202502 (2012)
138. Sidorchuk S I et al. *Phys. Lett. B* **594** 54 (2004)
139. Tilquin I et al. *Nucl. Instrum. Meth. Phys. Res. A* **365** 446 (1995)
140. Slepnev R S et al., in *Exotic Nuclei, EXON-2014, Proc. of Intern. Symp. on Exotic Nuclei, Kaliningrad, Russia, 8–13 September 2014* (Eds Yu E Penionzhkevich, Yu G Sobolev) (Singapore: World Scientific, 2015) p. 619
141. Mukha I et al., GSI Scientific Report pHW-ENNA-EXP-45 (2013)
142. Yukhimchuk A A et al. *Nucl. Instrum. Meth. Phys. Res. A* **513** 439 (2003)
143. Cwiok M et al. *IEEE Trans. Nucl. Sci.* **52** 2895 (2005)
144. Miernik K et al. *Nucl. Instrum. Meth. Phys. Res. A* **581** 194 (2007); *VCI 2007, Proc. of the 11th Intern. Vienna Conf. on Instrumentation*
145. Mianowski S et al. *Acta Phys. Pol. B* **41** 449 (2010)
146. Miernik K et al. *Phys. Rev. C* **76** 041304(R) (2007)
147. Pomorski M et al. *Phys. Rev. C* **90** 014311 (2014)
148. Pfützner M et al. *Phys. Rev. C* **92** 014316 (2015)
149. Lis A A et al. *Phys. Rev. C* **91** 064309 (2015)
150. Tanihata I *J. Phys. G* **22** 157 (1996)
151. Smirnov Yu F, Tchuvil'sky Yu M *Phys. Rev. C* **15** 84 (1977)
152. Nemets O F et al. *Nuklonnye Assotsiatsii v Atomnykh Yadrakh i Yadernye Reaktsii Mnogonuklonnykh Peredach* (Nucleon Associations in Atomic Nuclei and Nuclear Reactions of Multi-Nucleon Transfer) (Kiev: Naukova Dumka, 1988)
153. Werby M F et al. *Phys. Rev. C* **8** 106 (1973)
154. Schenk K et al. *Phys. Lett. B* **52** 36 (1974)
155. Ter-Akopian G M et al. *Phys. Lett. B* **426** 251 (1998)
156. Bachelier D et al. *Nucl. Phys. A* **195** 361 (1972)
157. Oganessian Yu Ts, Zagrebaev V I, Vaagen J S *Phys. Rev. Lett.* **82** 4996 (1999)
158. Wolski R et al. *Phys. Lett. B* **467** 8 (1999)
159. Sidorchuk S I et al. *Nucl. Phys. A* **840** 1 (2010)
160. Seth K K et al. *Phys. Rev. Lett.* **58** 1930 (1987)
161. Bohlen H et al. *Prog. Part. Nucl. Phys.* **42** 17 (1999)
162. Rogachev G V et al. *Phys. Rev. C* **67** 041603(R) (2003)
163. Chen L et al. *Phys. Lett. B* **505** 21 (2001)
164. Volya A, Zelevinsky V *Phys. Rev. C* **74** 064314 (2006)
165. Johansson H T et al. *Nucl. Phys. A* **842** 15 (2010)
166. Kalanee T A et al. *Phys. Rev. C* **88** 034301 (2013)
167. Korshennikov A A et al. *Phys. Rev. Lett.* **87** 092501 (2001)
168. Golovkov M S et al. *Phys. Lett. B* **566** 70 (2003)
169. Meister M et al. *Phys. Rev. Lett.* **91** 162504 (2003)
170. Gornov M G et al. *JETP Lett.* **77** 344 (2003); *Pis'ma Zh. Eksp. Teor. Fiz.* **77** 412 (2003)
171. Korshennikov A A et al. *Phys. Lett. B* **326** 31 (1994)
172. Ostrowski A N et al. *Phys. Lett. B* **338** 13 (1994)
173. Johansson H T et al. *Nucl. Phys. A* **847** 66 (2010)
174. Kohley Z et al. *Phys. Rev. Lett.* **109** 232501 (2012)
175. Iwasaki H et al. *Phys. Lett. B* **491** 8 (2000)
176. Papka P et al. *Phys. Rev. C* **81** 054308 (2010)
177. Batty C et al. *Nucl. Phys. A* **120** 297 (1968)
178. Bochkarev O V et al. *Sov. J. Nucl. Phys.* **55** 955 (1992); *Yad. Fiz.* **55** 1729 (1992)
179. Yang X et al. *Phys. Rev. C* **52** 2535 (1995)
180. Nakayama S et al. *Phys. Rev. Lett.* **85** 262 (2000)
181. Nakamura T *Eur. Phys. J. A* **13** 33 (2002)
182. Tilley D et al. *Nucl. Phys. A* **745** 155 (2004)
183. Markenroth K et al. *Nucl. Phys. A* **679** 462 (2001)
184. Meister M et al. *Nucl. Phys. A* **700** 3 (2002)
185. Grigorenko L V et al. *Part. Nucl. Lett.* **6** 118 (2009); *Pis'ma Fiz. Elem. Chast. At. Yad.* **6** 197 (2009)
186. Korshennikov A A et al. *Phys. Rev. Lett.* **90** 082501 (2003)
187. Gurov Yu B et al. *Phys. Part. Nucl.* **40** 558 (2009); *Fiz. Elem. Chast. At. Yad.* **40** 1062 (2009)
188. Caamaño M et al. *Phys. Rev. Lett.* **99** 062502 (2007)
189. Caamaño M et al. *Phys. Rev. C* **78** 044001 (2008)
190. Nikolskii E Yu et al. *Phys. Rev. C* **81** 064606 (2010)
191. Danilin B V et al. *Phys. Rev. C* **55** R577 (1997)
192. Garrido E, Fedorov D V, Jensen A S *Phys. Rev. C* **69** 024002 (2004)
193. Chromik M J et al. *Phys. Rev. C* **55** 1676 (1997)
194. Chromik M J et al. *Phys. Rev. C* **66** 024313 (2002)
195. Firestone R *Nucl. Data Sheets* **110** 1691 (2009)
196. Sigmaphi, <http://www.sigmaphi.fr/>
197. Beeckman W et al., in *Proc. of the 13th Intern. Conf. on Heavy Ion Accelerator Technology, HIAT2015, Yokohama, Japan, September 7–11, 2015*
198. Geissel H et al., in *Exotic Nuclei, EXON-2014, Proc. of Intern. Symp. on Exotic Nuclei, Kaliningrad, Russia, 8–13 September 2014* (Eds Yu E Penionzhkevich, Yu G Sobolev) (Singapore: World Scientific, 2015) p. 579
199. Mukha I et al. *Phys. Rev. C* **79** 061301(R) (2009)
200. Mukha I et al. *Phys. Rev. C* **82** 054315 (2010)
201. Vries H D, Jager C D, Vries C D *At. Data Nucl. Data Tabl.* **36** 495 (1987)
202. Hofstadter R *Rev. Mod. Phys.* **28** 214 (1956)
203. Savard G et al. *Nucl. Instrum. Meth. Phys. Res. B* **204** 582 (2003)
204. Plass W et al. *Nucl. Instrum. Meth. Phys. Res. B* **317** 457 (2013)
205. Bekhterev V et al. *High Energy Phys. Nucl. Phys.* **31** 23 (2007)
206. Donets E D *Rev. Sci. Instrum.* **69** 614 (1998)
207. Donets D E et al. *Priklad. Fiz.* (3) 34 (2010)
208. Leitner D *Nucl. Instrum. Meth. Phys. Res. B* **317** 235 (2013)
209. Delahaye P *Nucl. Instrum. Meth. Phys. Res. B* **317** 389 (2013)
210. Budker G I, Skriskii A N *Sov. Phys. Usp.* **21** 277 (1978); *Usp. Fiz. Nauk* **124** 561 (1978)
211. Skriskii A N, Parkhomchuk V V *Sov. J. Part. Nucl.* **12** 223 (1981); *Fiz. Elem. Chast. At. Yad.* **12** 557 (1981)